Spring 1-1-2017

Effects of Submesoscale Turbulence on Reactive Tracers in the Upper Ocean

Katherine Margaret Smith
University of Colorado at Boulder, kat.smith133@gmail.com

Effects of Submesoscale Turbulence on Reactive Tracers in the Upper Ocean

by

Katherine Margaret Smith

B.S., San Francisco State University, 2012

M.S., University of Colorado Boulder, 2015

A thesis submitted to the

Faculty of the Graduate School of the

University of Colorado in partial fulfillment

of the requirements for the degree of

Doctor of Philosophy

Department of Mechanical Engineering

2017

This thesis entitled:
Effects of Submesoscale Turbulence on Reactive Tracers in the Upper Ocean
written by Katherine Margaret Smith
has been approved for the Department of Mechanical Engineering

_____
Prof. Peter Hamlington

_____
Prof. John Daily

Date _____

The final copy of this thesis has been examined by the signatories, and we find that both the content and the form meet acceptable presentation standards of scholarly work in the above mentioned discipline.

Smith, Katherine Margaret (Ph.D., Mechanical Engineering)

Effects of Submesoscale Turbulence on Reactive Tracers in the Upper Ocean

Thesis directed by Prof. Peter Hamlington

In this dissertation, Large Eddy Simulations (LES) are used to model the coupled turbulence-reactive tracer dynamics within the upper mixed layer of the ocean. Prior work has shown that LES works well over the spatial and time scales relevant to both turbulence and reactive biogeochemistry. Additionally, the code intended for use is able to carry an arbitrary number of tracer equations, allowing for easy expansion of the species reactions. Research in this dissertation includes a study of 15 idealized non-reactive tracers within an evolving large-scale temperature front in order determine and understand the fundamental dynamics underlying turbulence-tracer interaction in the absence of reactions. The focus of this study, in particular, was on understanding the evolution of biogeochemically-relevant, non-reactive tracers in the presence of both large ($\sim$ 5 km) submesoscale eddies and small-scale ($\sim$ 100 m) wave-driven Langmuir turbulence. The 15 tracers studied have different initial, boundary, and source conditions and significant differences are seen in their distributions depending on these conditions. Differences are also seen between regions where submesoscale eddies and small-scale Langmuir turbulence are both present, and in regions with only Langmuir turbulence. A second study focuses on the examination of Langmuir turbulence effects on upper ocean carbonate chemistry. Langmuir mixing time scales are similar to those of chemical reactions, resulting in potentially strong tracer-flow coupling effects. The strength of the Langmuir turbulence is varied, from no wave-driven turbulence (i.e., only shear-driven turbulence), to Langmuir turbulence that is much stronger than that found in typical upper ocean conditions. Three different carbonate chemistry models are also used in this study: time-dependent chemistry, equilibrium chemistry, and no-chemistry (i.e., non-reactive tracers). The third and final study described in this dissertation details

the development of a reduced-order biogeochemical model with 17 state equations that can accurately reproduce the Bermuda Atlantic Time-series Study (BATS) ecosystem behavior, but that can also be integrated within high-resolution LES.

Dedication

"Somewhere on the mountain,
It's said that there's a potion,
That makes you truly happy,
And infinite in wisdom."
$\sim$ *Mihali Savoulidis*

Acknowledgements

I would like to start with thanking my advisor, Professor Peter Hamlington, for his guidance and support throughout the course of my graduate work. His enthusiasm for all things turbulence related has been infectious and inspiring. He has been patient in my learning process and gone to great lengths to ensure I've recieved the best preparation for a career in research.

Additionally, I would like to thank the many collaborators I've had the pleasure of working with, and hope to contiue doing so. Professor Nadia Pinardi, whos enthusiasm for science and life cannot be overstated. She, along with Professor Marco Zavaterelli, has been generous enough to host me several times at the University of Bologna, Ravenna Campus in Italy. While there, they helped mentor me, both in matters of science and Italian culture, and contributed greatly to the work in this thesis. Professor Baylor Fox-Kemper from Brown University, who has provided many insights regarding submeoscale processes and helped facilitate the assimilation of this engineer into a oceanography world. Professor Nicole Lovenduski, who has helped to ground the oceanic biogeochemistry within this thesis and help facilitate my participation in an amazing field research campaign over the Southern Ocean. I would also like to thank the remaining members of my dissertation committee, Professors Daven Henze and John Daily, for their time and energy in ensuring this dissertation was of the highest quality.

During the last four years, I have had opportunity to share both time and work space with many students at the University of Colorado, including Ryan King, Colin Towery, Spencer Alexander, Nicolas Wimer, Ryan Darragh, and Jason Christopher. I have greatly appreciated the science and life conversations and the support each one of you has provided.

Last, but certainly not least, I would like to thank my friends and family for their love and support through out this process. My parents have never wavered in their enthusiasm for my pursuit of high-education and have patiently listened to me jabber on about all things science, despite them often not understanding a word I have said. And to my friends, I could not have done this without you. Camping trips, powder days, dancing like goofballs, and trail running in the mountains with all of you has been my anchor through all of this.

Contents

Chapter

Tables

Table

Figures

Figure

Chapter 1

Introduction

The properties and evolution of tracers in the upper ocean are critical for understanding the global carbon cycle and climate. Such tracers include phytoplankton, nutrients, and CO_2. Phytoplankton, confined to the upper layers of the ocean due to light penetration and the pycnocline, consume inorganic carbon and nutrients diffused across the air-sea interface or entrained from depth. At the end of their life, they then sink to the interior of the ocean or are consumed by zooplankton. Similarly, CO_2 diffuses across the air-sea interface and is transformed into carbonate and bicarbonate by chemical reactions, after which it remains sequestered in the ocean.

Both phytoplankton and CO_2 are examples of reactive tracers that can be spontaneously created and destroyed, although the specific reaction models themselves differ. These tracers are additionally mixed and transported by turbulent processes. Due to turbulent mixing both vertically and horizontally, reactive tracers are not spatially uniform throughout the mixed layer and exhibit patchy distributions over a wide range of scales. Since concentrations of these reactive tracer species at mixed layer boundaries can greatly affect exchange rates, it is crucial to include the coupling of this turbulent mixing in reactive tracer transport models. Recent research has shown the importance of fluid motions by submesoscale (1$\sim$10 km) eddies on reactive tracers, but very small scales (1km$\sim$1m) have yet to be examined. Small scale turbulence includes both wave- (i.e., Langmuir) and shear-driven turbulence, and can affect reactive tracer evolutions since turbulent mixing time scales at such small scales can

be similar to reaction (e.g., chemical) time scales. Additionally, these small scale motions can affect the depth of the mixed layer. A comprehensive look at these scales, both in the presence and absence of larger submesoscale eddies, is therefore required in order to gain a more complete understanding of their effects on reactive tracer properties and evolution in the upper ocean.

The need for this more complete understanding provides motivation for the present dissertation. In this work, a series of studies are performed to examine the effects of submesoscale eddies and small-scale turbulence on the evolution of biogeochemically-relevant reactive tracers. These studies are based on numerical ocean data from large eddy simulations of turbulent and reactive tracer dynamics in a variety of contexts. The complexity of these simulations is progressively increased from tracers that do not interact, to chemically reacting tracers relevant to the inorganic carbon cycle, to the formulation of a reduced biogeochemical model that can be used to study the evolution of biological tracers (e.g., phytoplankton) in high resolution simulations.

1.1 Ocean Turbulence

Ocean turbulence spans a wide range of scales, from the global thermohaline circulation and basin scale processes down to the millimeter energy dissipation scale. The dominant physics and characteristics of the flow at each of these scales differs greatly and many of these scales interact with each other as well as the larger global carbon cycle in order to transport heat, momentum, and tracers. Dominant scales of motion within the ocean can be roughly divided up into the following categories: *(i)* large scale, *(ii)* mesoscale, *(iii)* submesoscale, and *(iv)* small scale. Below a brief over view of each scale is given.

1.1.1 Large Scale Processes

Large-scale ocean turbulence differs from standard incompressible isotropic turbulence in that it is characterized by large-scale rotation and stratification as well as a small aspect

ratio between its horizontal and vertical scales, or otherwise known as thin fluid motions. Their relative horizontal length scales are $\mathcal{O}(100+$ km) [5], while their vertical length scales are only a few kilometers. This small small aspect ratio between its horizontal and vertical scales gives rise to essentially two-dimensional type motions. Large-scales processes exhibit small Rossy numbers (i.e. Coriolis force is much greater than convective forces), small Froude numbers (i.e. vertical stratification is large), and large Richardson numbers (i.e. stably stratified).

Large-scale flow in the ocean can be broken up into three layers: *(i)* the near-surface layer, *(ii)* the interior, and *(iii)* the near bottom layer. The first and last layers are dominated by boundary layer processes, while the interior is dominated by pressure gradients. In order to derive the equations of motion that describe large-scale motions within the interior of the ocean, known as the planetary geostrophic equations, we first must begin with the full governing equations of motion for incompressible flow [5] **Momentum Equation**

$$\frac{D\mathbf{u}}{Dt} + 2\mathbf{\Omega} \times \mathbf{u} = -\frac{1}{\rho}\nabla p + \nu\nabla^2\mathbf{u} - g\mathbf{k} \tag{1.1}$$

Mass Conservation Equation

$$\frac{D\rho}{Dt} + \rho\nabla \cdot \mathbf{u} = 0 \tag{1.2}$$

Thermodynamic Equation

$$\frac{D\rho}{Dt} - \frac{1}{c_s^2}\frac{Dp}{Dt} = \frac{\dot{Q}}{\left(\partial\eta/\partial\rho\right)_{p,S} T} - \left(\partial\rho/\partial S\right)_{\rho,p}\dot{S} \tag{1.3}$$

where $\mathbf{u}$ is the full velocity vector, $\mathbf{\Omega}$ is the angular velocity of the Earth, ρ is density, p is pressure, ν is viscosity, g is gravity, c_s is the sound speed, $\dot{Q}$ is the heat flux, $\left(\partial\eta/\partial\rho\right)_{p,S}$ is the change in entropy with respect to density, T is temperature, $\left(\partial\rho/\partial S\right)_{\rho,p}$ is the change in density with respect to salinity, and $\dot{S}$ is the salinity flux. In order to arrive at the planetary geostrophic equations, we first need to derive what are known as the stratified primitive equations, which make the following assumptions [5]

(1) Thin-fluid approximation: Given that the radius of the Earth is $\mathcal{O}(6000\text{km})$ and the thickness of the ocean is $\mathcal{O}(4\text{km})$, it is assumed that the depth of the ocean or atmosphere is negligible in comparison to the radius of the earth except when differentiating.

(2) Hydrostatic approximation: It is assumed that gravity is balanced by the pressure gradient within the vertical momentum equations, leaving only

$$\frac{\partial p}{\partial z} = -\rho g\,, \tag{1.4}$$

For large-scale flows, $Fr^2\alpha^2 \sim \mathcal{O}(10^{-10})$, where Fr is the Froude number and is a measure of the vertical stratification, and α^2 is a measure of the small aspect ratio. When $Fr^2\alpha^2 \ll 1$, the flow is both stratified and of a small aspect ratio, therefore hydrostasy holds.

(3) Boussinesq approximation: The density variations in the ocean are small compared to the mean density and so it is assumed that density variations are negligible unless when multiplied by gravitational terms.

(4) Large Reynolds number approximation: Viscous terms are small and thus can be ignored.

Applying these assumptions gives us the following stratified primitive equations in vector form [5]

$$\frac{D\mathbf{v}}{Dt} + \mathbf{f} \times \mathbf{vv} = \nabla_z \phi \tag{1.5}$$

$$\frac{\partial \phi}{\partial z} = b \tag{1.6}$$

$$\frac{Db}{Dt} = 0 \tag{1.7}$$

$$\nabla \cdot \mathbf{u} = 0 \tag{1.8}$$

where $\mathbf{v}$ is just the horizontal velocity vector, $f = 2\Omega \sin\theta$ is the vertical component of the Coriolis parameter, $\phi = \delta p/\rho_0$, and $b = -g\delta\rho/\rho_0$. In order to arrive at the planetary geostrophic equations, the following additional assumption must be made [5]

(1) Geostrophic balance approximation: It is assumed that in the horizontal momentum equation, the rotation and pressure terms balance. If the Rossby number is small, which is true for large-scale motions ($Ro \ll 1$), convective forces will be small in comparison to the Coriolis force. Additionally, if the time period of the motion scales advectively, the time derivative will also be small in comparison to the Coriolis force.

Applying this final assumption, we get the final planetary geostrophic equations in vector form

$$f \times \mathbf{u_g} = -\frac{\partial \phi}{\partial y}\,, \quad fv_g = \frac{\partial \phi}{\partial x} \tag{1.9}$$

$$\frac{\partial \phi}{\partial z} = b\,, \tag{1.10}$$

$$\frac{Db}{Dt} = 0\,, \tag{1.11}$$

$$\nabla \cdot \mathbf{v}_g = 0\,, \tag{1.12}$$

where now $\mathbf{v}_g$ is only the horizontal geostrophic velocity vector, and u_g is the zonal component and v_g is the meridional component.

The planetary geostrophic equations are only valid when horizontal scales of motion much greater than that of the Rossby radius of deformation ($L_d = NH/f_0$, where N is the buoyancy frequency, H is the mean depth of the fluid, and f_0 is the magnitude of the Coriolis force) or when the Rossby number is sufficiently small, meaning that rotational terms are much greater than any convective or buoyancy terms. If horizontal scales of motion become on the order of the deformation radius, these equations no longer apply.

From these equations it can be seen that, within the interior ocean, a balance exists between two opposing forces in both the horizontal and vertical directions. In the vertical direction, an assumed balance exists between the pressure gradient and gravity (i.e. the hydrostatic balance). In the horizontal direction, an assumed balance between the pressure gradient and the Coriolis force exists. These balances, along with large-scale boundary layer processes, are what drive large-scale circulations in the ocean such as the Gulf Stream, the Antarctic circumpolar current, the Kuroshio current, and many other currents and gyres.

Away from the interior of the ocean, very near to the surface, lateral pressure gradients are small and surface boundary layer effects, such as wind stress, become large and balance with the Coriolis force [5]. This balance leads to what is known as Ekman transport. Near the equator, 60°N, and 60°S, Ekman transport causes large-scale divergence of the flow, leading to upwelling (Ekman suction), elevated sea surface heights, and greater pressures at depth. At 30°N and 30°S, Ekman transport causes large-scale convergence of the flow, leading to downwelling (Ekman pumping), depressed sea surface heights, and less pressure at depth. It can be seen from the previous planetary geostrophic equations, that large-scale geostrophic flow is confined to being parallel to lines of constant pressure, meaning that in the Northern hemisphere (where $f > 0$), geostrophic flow is clockwise around regions of Ekman convergence and high pressure and anti-clockwise around regions of Ekman divergence and low pressure. Typical horizontal velocities due to interior geostrophic currents are on the order of 0.1 m s^{-1} [5]. Conversely, typical vertical velocities due to Ekman transport are on the order of 10^{-6} m s^{-1} [6, 7].

1.1.2 Mesoscale Processes

Large-scale motions are typically unstable to strong horizontally sheared motions as well as baroclinic instabilities, or when the pressure and density gradients are misaligned. When such instabilities are present the next dominant scale of motion develops, mesoscale eddies and filaments. Mesoscale processes have horizontal length scales of $\mathcal{O}$(10 - 100 km) and

times scales of $\mathcal{O}$(1 month) [6, 8]. Like large-scale processes, they have small Rossy numbers and large Richardson numbers [9]. However, unlike large-scale processes, mesoscales have horizontal scales on a similar order of magnitude to that of the Rossby radius of deformation [5], meaning convective or buoyancy terms are no longer sufficiently smaller than Coriolis terms that they can be ignored entirely. The equations of motion that describe mesoscale processes are known as the quasi-geostrophic equations, in that they are close to geostrophic, but still take into account the nonlinear advective and time derivative terms

$$\frac{D\mathbf{v}_g}{Dt} - \mathbf{f} \times [\mathbf{v}_g + \mathbf{v}_a] = \nabla_z \phi \,, \tag{1.13}$$

$$\frac{\partial \phi}{\partial z} = b \,, \tag{1.14}$$

$$\frac{Db}{Dt} = 0 \,, \tag{1.15}$$

$$\nabla_z \cdot \mathbf{v}_g = 0 \,, \quad \nabla_z \cdot \mathbf{v}_a + \frac{\partial w}{\partial z} = 0 \,, \tag{1.16}$$

where $\mathbf{v} = \mathbf{v}_g + \mathbf{v}_a$, $\mathbf{v}_g$ is the horizontal geostrophic velocity vector, $\mathbf{v}_a$ is the horizontal ageostrophic velocity vector, and w is the total vertical velocity vector. Mesoscale eddies develop from large-scale currents, primarily in the form of large circular front-like structures or domed isopycnals [6]. Similarly to large-scale motions, mesoscale eddies are essentially still two-dimensional processes, in that their horizontal spatial are much greater than than their vertical scales ($\sim$ 1 km). While they exhibit similar horizontal velocities ($U = 0.1$ m s^{-1}), theory, observations, and models [10–15] all show that they can exhibit greater vertical velocities than large-scale processes (i.e. Ekman pumping and suction) at fronts ($W = 10^{-4}$m s^{-1}) [16].

1.1.3 Submesoscale Processes

The formation of mesoscale eddies and fronts described in the previous section, along with the filaments that can be formed from them due to stretching, give rise to the next smallest scale of motion, submesoscale processes. In the absence of buoyancy forcing, such

as radiative heating or cooling at the surface, buoyancy must be conserved within the flow. However, existing horizontal buoyancy gradients, formed by large-scale and mesoscale fronts, eddies, and filaments, can evolve and lead to an intensification of a front. This leads to Richardson numbers close to $\mathcal{O}(1)$, an increase in the horizontal vorticity, and a local Rossby number of $\mathcal{O}(1)$ [9, 16]. The geostrophic balance from the two previous processes is now lost. Due to this, a secondary ageostrophic circulation develops which attempts to restore this balance through up- and down-welling at the front which advectively tilts isopycnals towards the horizontal, promotes restratification, and accelerates the geostrophic flow [16, 17]. This secondary ageostrophic vertical velocity is on the order of 10^{-3} m s^{-1} and the upwelling portions that develop at the base of the mixed layer can help to inject buoyancy and tracers stored at depth into the mixed layer in the form of concentrated jets and plumes. Horizontal length scales of submesoscale processes are $\mathcal{O}$(1-10 km) and have time scales of $\mathcal{O}$(1 day) [16, 18]. Although submesoscale processes still exhibit substantially greater horizontal scales than vertical scales, unlike large-scale and mesoscale processes, submesoscale processes are only considered quasi two-dimensional due to the considerable vertical velocities they can produce.

A fundamental physical process that leads to the development of submesoscales is the loss of geostrophic balance and a defining characteristic is its $\mathcal{O}(1)$ Rossby numbers. Thus, the only valid assumptions to be made for submesoscale processes is that of the Boussinesq and hydrostatic approximations, which leads to the following equations

$$\frac{D\mathbf{v}}{Dt} - \mathbf{f} \times \mathbf{v} = -\nabla_z \phi \,, \tag{1.17}$$

$$\frac{\partial \phi}{\partial z} = b \,, \tag{1.18}$$

$$\nabla \cdot \mathbf{u} = 0 \,, \tag{1.19}$$

$$\frac{Db}{Dt} = \dot{b} \,, \tag{1.20}$$

where $\dot{b} = g\beta_T \dot{Q}/c_p$, β_T is the thermal expansion coefficient, and c_p is the constant pressure heat capacity.

Symmetric instabilities, shear instability that arises due to misalignments of the buoyancy and momentum fields, have also been associated with submesoscale processes. Symmetric instabilities extract kinetic energy from geostrophic flows [19], meaning they can serve as an important link between submesoscales and non-hydrostatic small scales [20–23], where dissipation can occur.

1.1.4 Small Scale Processes

Small scale turbulence in the ocean differs substantially from any of the previous scales of motion discussed so far, as they are truly three-dimensional, non-hydrostatic, and exhibit a forward cascade of energy down to the dissipation scale [24]. Small scale processes within the ocean can develop due to several different mechanisms. The most common of which are boundary layer processes, which involve the flux of either buoyancy or momentum to or from the upper layer of the ocean through the surface boundary layer. The first of these is a buoyancy instabilities due to heat loss or precipitation and the second is a shear instabilities driven by wind and waves. Characteristic behavior of the small-scale processes produced by each of these instabilities can be fundamentally different. With respect to small scale processes, only the Boussinesq approximation applies

$$\frac{D\mathbf{u}}{Dt} - \mathbf{f} \times \mathbf{u} = -\nabla\phi - b\mathbf{k}\,, \tag{1.21}$$

$$\nabla \cdot \mathbf{u} = 0\,, \tag{1.22}$$

$$\frac{\partial b}{\partial t} + \mathbf{u} \cdot \nabla b = 0\,. \tag{1.23}$$

Small scale processes typically have horizontal and vertical length scales of $\mathcal{O}$(1-100 m) and time scales much less than 1 day. Additionally, due to their three-dimensional nature, small scale turbulent processes have an overall homogenizing, or mixing, effect on the upper layer of the ocean, in contrast to the largely stratifying effects of each of the previously discussed processes.

A particular type of small scale turbulence of interest to the work done in this thesis, is

Langmuir turbulence. Langmuir turbulence is a surface-confined, three-dimensional, small-scale ocean process that results from surface waves, and their induced Stokes drift, tilting vertical vorticity anomalies into the horizontal, creating disordered rows of counter rotating roll structures called Langmuir cells[25]. The convergent and divergent regions of the counter rotating Langmuir cells produce strong upwelling and downwelling velocities that can extend well below the surface and lead to increased mixing of the upper ocean, as seen in Figure 1.1. Often this also results in a deeper mixed layer depth due to increased entrainment of stratified waters below. "Windrows" are a defining visual characteristic of Langmuir turbulence where debris, bubbles, oil, and many other tracers collect and concentrate along the surface convergent zones of the Langmuir cells. The effects of Langmuir turbulence can be described by the Craik-Leibovich equations[27–31], which are obtained by wave-averaging the Boussinesq equations above

$$\frac{D\mathbf{u}}{Dt} = -\nabla p - \mathbf{f} \times \mathbf{u}_L - u_{L,j}\nabla u_{s,j} - b\mathbf{k}\,, \tag{1.24}$$

$$\nabla \cdot \mathbf{u} = 0\,, \tag{1.25}$$

$$\frac{\partial b}{\partial t} + \mathbf{u}_L \cdot \nabla b = 0\,. \tag{1.26}$$

where now $\mathbf{u}_L \equiv \mathbf{u} + \mathbf{u}_s$ is the Lagrangian velocity, and $\mathbf{u}_s$ is the surface gravity wave induced Stokes drift velocity. The strength of the Langmuir turbulence can be identified by its turbulent Langmuir number, which is defined as the ratio of mixing due to Langmuir turbulence over the mixing due to shear turbulence, $La_t^2 = u_*/u_s(0)$, where u_* is the surface friction velocity and $u_s(0)$ is the Stokes drift velocity at the surface.

1.2 Coupling to Ocean Tracers

The ocean is estimated to store over 20% of all anthropogenic CO_2 and over 90% of anthropogenic heat [32, 33], and is the largest reservoir of carbon in the Earth system that is active on short timescales. This is partially due in part to the evolution and properties of ocean biogeochemical tracers such as CO_2, phytoplankton, and nutrients. Each of these

Figure 1.1: A sketch of Langmuir circulations and their resulting upwelling and downwelling regions [26].

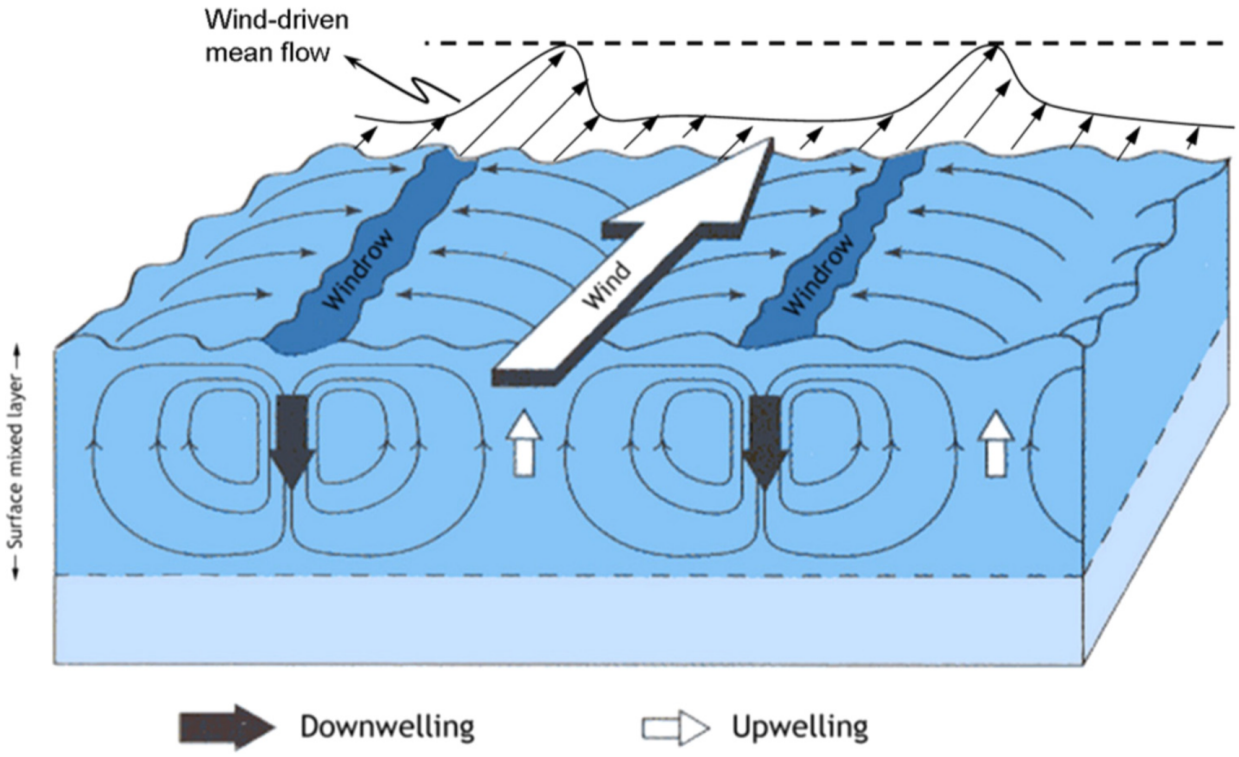

tracers can be conceptualized as an Eulerian concentration field (as opposed to discrete Lagrangian particles) that is advected by the fluid flow. The evolution of such tracers occurs primarily in the oceanic mixed layer where light is plentiful, air-sea exchanges of energy, momentum, gases, and freshwater occur [e.g., 34], and various scales of turbulent motion are active in transporting tracers. The evolution and properties of mixed layer tracers are thus closely coupled to the dynamics of upper ocean turbulence. Figure 1.2 shows a sketch of just a few of these upper ocean processes, both tracers and turbulence, that interact with each other and can have important roles in the global carbon cycle.

Even when ocean tracers are passive (i.e., their concentration does not affect density or otherwise change the flow), their coupling to multiscale mixed layer turbulence is not trivial. As an example of this complex coupling, the supply of CO_2 across the air-sea interface depends on the rate at which vertical mixing transports CO_2 downward, thereby maintaining (or, conversely, failing to maintain) a favorable air-sea gradient for diffusion of CO_2 across the surface [35]. Phytoplankton are most productive near the surface where light is plentiful for photosynthesis, but in order to grow they require that nutrients be brought upward from stores at depth. The dispersion of buoyant oil, which often collects at the surface after accidental spills, is yet another example of turbulent tracer transport across many scales of upper ocean motion.

It is well known from prior observational [36–42] and numerical [6, 43–50] studies that the coupling between biogeochemical tracers and fluid processes results in heterogeneous distributions of tracers at the ocean surface. The origins and characteristics of this heterogeneity are understood to have potential biological and physical origins, particularly at small (i.e., sub-kilometer) scales. However, these prior studies have also revealed a major unresolved difficulty in fully describing the origins of tracer heterogeneity: namely, understanding and explaining the impacts of multiscale turbulent fluid processes on tracer evolution, and the "solubility" and "biological" carbon pumps in particular.

The range of fluid scales relevant to ocean tracer evolution is truly enormous. Ocean

Figure 1.2: A sketch of processes within the upper ocean mixed layer (Illustration from Jayne Doucette, Woods Hole Oceanographic Institution).

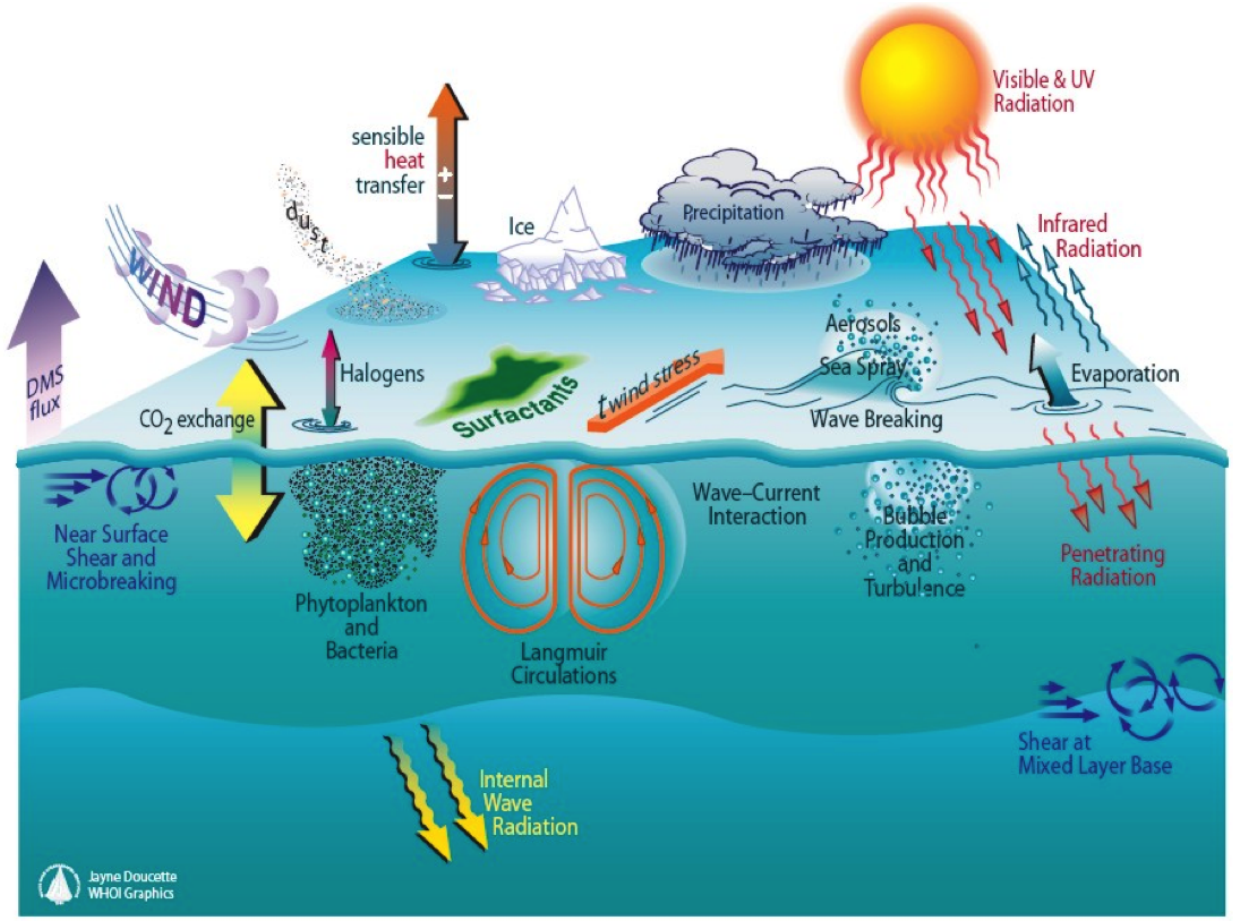

biogeochemistry is affected by fluid processes that span large scale (∼10,000 km) budgets to millimeter-scale flows where kinetic energy and tracer variance are dissipated [51, 52]. As we discussed previously, many important fluid processes take place between these scales, and processes at widely disparate scales may also interact [4, 53, 54]. Recent studies have shown that physical transport by mesoscale and submesoscale circulations can give rise to substantial tracer heterogeneity [6, 36, 45, 55–57]. In particular, prior studies [56, 58–60] have revealed that upwelling associated with mesoscale and submesoscale fronts plays a key role in nutrient transport, phytoplankton production, and bloom timing and budgets. These upwelling motions produce $\mathcal{O}$(1km) variations in tracer distributions at the surface, which are also affected by biological and chemical processes.

Knowledge gained from combustion research shows that the most significant tracer-flow couplings occur when coherent structures in the flow have timescales that rival reaction time scales. The Damkohler number, a non-dimensional number that relates the chemical (or biological) reaction rate to the transport rate, has been calculated between the physical process scales discussed previously and two important categories of ocean reactive tracer that affect the carbon cycle, biological and chemical tracers, and is shown in Table 1.1. Many upper ocean biological reaction rates, such as the nutrient uptake and growth rate of phytoplankton or grazing of zooplankton, are also on the order of $\mathcal{O}$(1day) [52]. Additionally, once CO_2 transfers across the air-sea interface it reacts with seawater to hydrate and produce bicarbonate (HCO_3^-) and carbonate (CO_3^{2-}) in a series of reactions whose rate limiting steps have time scales of approximately 10-25s [2]. Dissimilarities in time scales (i.e., time scale ratios are not close to $\mathcal{O}(1)$) indicates either the tracer reactions or the physical process is much faster than the other, so strong tracer-flow couplings are not likely and it is appropriate to assume the fast process is in steady-state with respect to the slower process. Since there are not significant time scale similarities between mesoscale and large-scale processes and biological and chemical tracers, it is assumed that the biological and chemical processes take place instantaneously in comparison to these larger scale processes. Therefore, they

Table 1.1: Damkohler numbers for various physical and biological/chemical proceses in the ocean.

	Small scale $\tau_t \sim 10^2$s	Submesoscale $\tau_t \sim 10^5$s	Mesoscale $\tau_t \sim 10^7$s	Large scale $\tau_t \sim 10^8$s
Chemical Processes [2]				
Surface transfer of CO_2: $\tau \sim$1s	10^2	10^5	10^7	10^8
Hydration/hydroxylation: $\tau \sim$10s	10^1	10^4	10^6	10^7
Protolysis/hydrolysis: $\tau \sim 10^{-7}$s	10^9	10^{12}	10^{14}	10^{15}
Equilibration of CO_2: $\tau \sim 10^2$s	1	10^3	10^5	10^6
Biological Processes [52]				
Nutrient uptake: $\tau \sim 10^5$s	10^{-3}	1	10^2	10^3
Phytoplankton growth: $\tau \sim 10^5$s	10^{-3}	1	10^2	10^3
Phytoplankton loss: $\tau \sim 10^5$s	10^{-3}	1	10^2	10^3
Zooplankton growth: $\tau \sim 10^5$s	10^{-3}	1	10^2	10^3
Zooplankton loss: $\tau \sim 10^6$s	10^{-4}	0.1	10	10^2
Zooplankton reaction: $\tau \sim$10s	10^1	10^4	10^6	10^7

only act to transport tracer as a bulk property of the flow, simply as a background state. In contrast, similarities in time scales (i.e. time scale ratios that are approximately $\mathcal{O}(1)$), such as submesoscale and biological processes as well as small-scale (specifically wave-driven Langmuir turbulence [25]) and chemical processes indicates a potential for strong tracer-flow coupling effects. These $\mathcal{O}(1)$ Damkohler numbers are what specifically motivate this thesis's further investigation into tracer-turbulence interactions at the submesoscale and small-scales.

1.3 Overview of Present Dissertation

In contrast to prior studies focused on the effects of larger-scale ocean processes on tracer dynamics, the present thesis work is specifically focused on the effects of submesoscale turbulent processes from meter to kilometer scales. The scale range examined here includes mixed layer restratification involving coherent vertical motions of water masses by submesoscale eddies and wind- and wave-influenced fronts and vertical mixing by Langmuir turbulence. These processes occur at subgrid scales in essentially all ESMs. Current state of the art is to run ESMs at $\leq 1/64^\circ$ resolution ($\sim$1 km at the equator). At best, these simulations can resolve mesoscale and larger submesoscale processes, but smaller submesoscale and

small-scale boundary layer processes, such as Langmuir turbulence, are still left unresolved. Additionally, the large computational expense of these simulations precludes them from being run to climate prediction timescales. Current state of the practice is to run ESMs at a $\leq$ 1° resolution ($\sim$100 km at the equator), which can be reasonably run to $\geq$ 100 year climate predictions times scale, however, leave even more energetic scales unresolved, both temporally and spatially. Given that recent research has shown the importance of tracer transport on scales left unresolved within ESMs, it is imperative we improved our understanding of these processes effects on tracer dynamics on a fundamental level. The knowledge gained from such studies can help to assist in the development of improved physically-accurate subgrid-scale tracer parameterizations.

Although submesoscale eddies and Langmuir turbulence commonly involve similar horizontal velocities of $\mathcal{O}(0.1$ m/s), their typical vertical velocity scales, and hence their ability to transport tracers, differ substantially. The ratio of horizontal to vertical length scales is $\mathcal{O}(1)$ for Langmuir cells, so the largest horizontal separation distance between these cells tends to vary with mixed layer depth [61]. The corresponding ratio of horizontal to vertical velocity scales is also $\mathcal{O}(1)$ for Langmuir cells. Submesoscale eddies, by contrast, tend to occur on horizontal scales near the mixed layer deformation radius [9, 18], so they are much wider than the mixed layer depth, with a horizontal to vertical length scale ratio of $\mathcal{O}(N/f)$, where N and f are the buoyancy frequency and Coriolis parameter magnitude, respectively. Such eddies are roughly ten to a hundred times wider than the mixed layer is deep under typical upper ocean stratification, mixing, and frontal strength conditions [62–64]. Furthermore, geostrophic flows avoid horizontal convergence and are therefore associated with small vertical velocities, so weaker submesoscale fronts and eddies (i.e., those with small Rossby number) have horizontal to vertical velocity scale ratios that are even greater than N/f [65]. During frontogenesis, the vertical velocity can be significantly larger at the nose of the front due to the frontal overturning circulation, and this velocity is further enhanced during the creation of fronts aligned with the Stokes drift [31].

Due to the multiscale nature of biogeochemical tracer dynamics in the oceanic mixed layer, previous studies have often focused on increasing the complexity of biogeochemical modeling while employing relatively simple background flows [e.g. 43, 50, 66–68]. In contrast, this dissertation work employs a foundational approach whereby first non-reactive passive tracers are modeled in the presence of realistic upper ocean turbulence and only then is tracer complexity (i.e. reactive chemistry or phytoplankton, nutrient, zooplankton dynamics) progressively increased towards realistic biogeochemistry. This approach, of modeling idealized tracers in complex flows, has complementary aims to those studying more complex tracer dynamics in simple flows.

The next chapter of this dissertation explores multiscale tracer-flow interactions between submesoscale and small-scale processes and upper ocean, non-reactive, passive tracers in order to gain baseline knowledge of tracer-flow coupling. This chapter is closely based on a journal publication by Smith *et al.* [69]. From there, both chemical and biological tracer reactions are explored. The second chapter explores single scale tracer-flow interactions between small-scale, Langmuir turbulence and upper ocean carbonate chemistry and the final chapter details the development of a new, reduced-order, biogeochemical model for use in a high-resolution LES simulation to further explore tracer-flow interactions.

Chapter 2

Multi-Scale Turbulence with Non-Reactive Tracers: Effects of Submesoscale Turbulence on Ocean Tracers

2.1 Introduction

Although real-world upper ocean tracers have substantial dynamical complexity, work in the present chapter employs a foundational approach whereby non-reactive passive tracers are modeled in the presence of realistic upper ocean turbulence for a wide range of tracer conditions. This approach is intended to reveal fundamental effects of upper ocean fluid transport processes on tracer evolution and distributions prior to increasing the complexity of the modeled tracers (e.g., by employing reactive chemistry or coupled nutrient, phytoplankton, and zooplankton dynamics). Tracers examined herein include non-conserved tracers that flux across the air-sea interface and conserved tracers released at different initial locations in the mixed layer. These tracers have been specifically chosen to represent biogeochemical tracers such as CO_2, phytoplankton, and oil, whose dynamics can be idealized as vertical transport problems. Such transport has a substantial impact on tracer heterogeneity, but there are a number of outstanding questions that must be still be answered, including:

(1) How is near-surface CO_2 flushed downward after diffusing across the air-sea interface?

(2) How do phytoplankton arrive in the euphotic zone?

(3) How are nutrients delivered to the euphotic zone from greater depths?

This first chapter will address key aspects of each of these questions by modeling the transport of idealized tracers in the presence of realistic submesoscale ocean flows that are spatially heterogeneous in horizontal directions and that also vary with scale. A range of different tracer flux rates and initial source locations will be examined in order to develop a parametric understanding of tracer evolution and properties, which will be of substantial benefit when using the present results to inform the development of new subgrid models for tracer transport.

Hamlington *et al.* [4] examined the same range of scales with a focus on the interactions between submesoscale processes and small-scale Langmuir turbulence, finding that the effects of Langmuir turbulence are weakened in the presence of submesoscale eddies. Contrasts will be made here between tracer behavior in regions where both submesoscale eddies and Langmuir turbulence are active, and in regions where only Langmuir turbulence is active. Submesoscale motions are coherent on larger scales than Langmuir turbulence, so spectral analysis of fluxes and tracer variance will also be used to understand tracer evolution and properties.

In this chapter, large eddy simulations are used to examine the effects of submesoscale ocean processes on the evolution of tracers in the oceanic mixed layer at horizontal scales from 20km down to 5m, with a specific focus on the respective roles played by submesoscale eddies, as well as their associated fronts, and Langmuir turbulence. Details of the physical set-up is outlined first, followed by a presentation of results from the simulations. These results are then discussed in the context of modeling tracer properties using eddy diffusivity approaches and understanding the patchiness of biological tracers such as phytoplankton. Finally, conclusions are provided at the end of the chapter.

2.2 Numerical Simulations

The simulations performed in this first chapter are extensions of the submesoscale frontal spin-down simulations described in [4]. The governing equations solved are the wave-

averaged Boussinesq equations [27–31] given by

$$\frac{D\mathbf{u}}{Dt} = -\nabla p - \mathbf{f} \times \mathbf{u}_L - u_{L,j}\nabla u_{s,j} + b\hat{\mathbf{z}} + \mathbf{SGS}_u \,, \tag{2.1}$$

$$\frac{Db}{Dt} = \mathbf{SGS}_b \,, \tag{2.2}$$

$$\frac{Dc_i}{Dt} = \mathbf{SGS}_{c_i} \,, \tag{2.3}$$

$$\nabla \cdot \mathbf{u} = 0 \,, \tag{2.4}$$

where $D/Dt \equiv \partial/\partial t + (\mathbf{u}_L \cdot \nabla)$ is the Lagrangian material derivative, $\mathbf{u}$ is the Eulerian velocity averaged over surface gravity waves, $\mathbf{f}$ is the Coriolis parameter, p is the pressure normalized by a reference density ρ_0, b is the buoyancy, $\mathbf{u}_L \equiv \mathbf{u} + \mathbf{u}_s$ is the Lagrangian velocity, and $\mathbf{u}_s$ is the Stokes drift velocity created by surface gravity waves. Buoyancy is given as $b = -g\rho/\rho_0$, where g is gravitational acceleration, ρ is density, and b has dimensions of acceleration. Buoyancy frequency is related to buoyancy by $N^2 = \partial b/\partial z$. The third term on the right-hand side of Eq. (2.1) is the Stokes shear force, which has been written using index notation for clarity [31]. In Eq. (2.3), c_i denotes the Eulerian concentration field for the ith tracer. The tracers are passive and thus do not impact the dynamics of the velocity $\mathbf{u}$ or the buoyancy b. In this chapter, the tracers considered are all non-reactive and thus there are no source terms on the right-hand side of Eq. (2.3), however, in the proceeding chapter the tracers are reactive and the source term on the right-hand-side of Eq. (2.3) accounts for sources and sinks due to chemical or biological reactions of the ith species. Each of the $\mathbf{SGS}_i$ terms in Eqs. (2.1)-(2.3) are vector fluxes representing the subgrid-scale (SGS) model used in the LES.

The Stokes drift velocity $\mathbf{u}_s$ in Eqs. (2.1)-(2.3) is represented in the simulations as

$$\mathbf{u}_s(z) = u_s(z)\left[\cos(\vartheta_s)\hat{\mathbf{x}} + \sin(\vartheta_s)\hat{\mathbf{y}}\right] \,, \tag{2.5}$$

where $u_s(z)$ is the Stokes drift magnitude vertical profile, which decays faster than exponentially from the surface, and ϑ_s is the angle of the Stokes drift velocity in the horizontal (i.e., $x-y$) plane. The mathematical formulation for $u_s(z)$ is given by numerical integration of the

Figure 2.1: Stokes drift velocity $u_s(z)$ used in Eq. (2.5) as a function of depth z. The main plot shows $u_s(z)$ on linear axes and the inset shows $u_s(z)$ on semi-log axes.

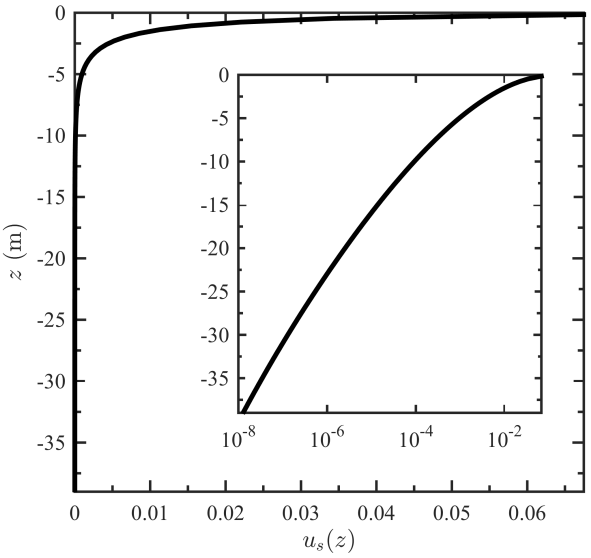

wave spectrum in Eq. (5.1) of [70] and Eq. (33) in [71], and is shown in Fig. 2.1 as a function of depth. Note that the Stokes drift velocity $\mathbf{u}_s$ is the same at all horizontal locations and depends only on z. Wave spreading effects on Stokes drift are neglected [72], as are breaking wave effects. Prior studies [4, 73, 74] have shown that this parameterization for the Stokes drift velocity leads to the creation of small-scale, counter-rotating Langmuir cells throughout the domain, with the strongest cells occurring close to the surface (i.e., within the upper 25m of the ocean) and substantial impacts on submesoscale fronts and instabilities [31, 53, 75].

The numerical model used to solve the governing equations is the National Center for Atmospheric Research (NCAR) LES model [76] which is described in [73] and [77]. Horizontal spatial derivatives are calculated spectrally, while second-order finite differences are used for vertical velocity derivatives and third-order finite differences are used for vertical tracer derivatives. A third-order Runge-Kutta time stepping scheme is used with a constant Courant number. Essentially the same model has been used in several prior studies [e.g., 4, 69, 73, 74, 77].

The LES is performed using a subgrid-scale model for the **SGS** terms in Eqs. (2.1)-(2.3) that provides a spatially-variable viscosity, buoyancy diffusivity, and tracer diffusivity according to the scheme proposed by [78]. As a result, there is no one tracer diffusivity or viscosity applied throughout the domain. A ratio between the tracer transport by the subgrid scheme and by the resolved flow can be formed and interpreted as a Péclet number (the Schmidt number, relating subgrid viscosity to diffusivity, is fixed at 1/3 by the subgrid scale model [78] and applies to both buoyancy and passive tracers). The horizontal Péclet number is 3.2 on 100m scales and 1262 on 10km scales. The vertical Péclet number is 1.3 using basin-averaged root-mean-square velocity and 50m mixed layer depth. In the real ocean, the equivalent quantities are $10^5, 10^7$ and 10^4, respectively. It is therefore likely that the subgrid scheme does affect the tracer transport significantly on small scales, particularly in the vertical direction, so the transport by Langmuir turbulence is likely to be quantitatively different when compared to a simulation with higher resolution. It is important to recognize, however, that variability in the subgrid diffusivity is intended to resemble a spectral variance cascade, so it may behave like a higher Péclet number flow, or in any case quite differently from a flow with constant diffusivity. The Péclet number of submesoscale features is very large, and so the interaction between submesoscale eddies and Langmuir turbulence crosses a range of scales where diffusivity is weak, as in the real ocean. The computational expense of the present simulation precludes a comparison to higher-resolution simulations, but in a smaller domain the effects of the subgrid scheme and finite Péclet number may be explored in the future.

The physical setup for the current chapter is the spin-down of two submesoscale buoyancy fronts; the same configuration has been examined previously in [4]. In the [4] study, a warm 10km-wide filament of water was initialized within a domain of cooler water. Oblique wind and wave forcing was applied at a horizontal angle of 30°, leading to destabilization of the more buoyant filament along an unstable front where the Ekman buoyancy flux from a downfront wind component carries more dense water over less dense water, resulting in the

formation of $\mathcal{O}(5\text{km})$ submesoscale eddies. A stable front on the other side of the buoyant filament is restratified by an upfront wind and Ekman buoyancy flux of less dense water carried over more dense water [20]. A mixed layer region was initialized near the surface of the domain with an initial uniform depth of $H_{ML,0} = -50\text{m}$. The mixed layer becomes both significantly deeper and shallower at different spatial locations as the system evolves. Substantial additional detail on the spin-down configuration and the subsequent evolution of the system is provided in [4].

The present study builds upon the simulations described in [4] by introducing tracers to the simulations and restarting the computations at roughly day 12, corresponding to the final fully-developed state in the [4] study. Figure 2.2 shows the buoyancy field at day 12 when the tracers are first introduced. At this time, a number of large submesoscale eddies have formed, but the eddies along the unstable front have not yet begun to interact with the stable front. The same wave and wind forcing is maintained after restarting the simulations, corresponding to a surface wind stress with wind speed of 5m/s and an angle of 30° with

Figure 2.2: Initial $x-y$ surface buoyancy field when tracers are introduced to the simulations, corresponding to approximately day 12 of the [4] study. Vertical white dashed lines denote the Langmuir only (LO) and submesoscale eddy (SE) regions over which statistics are calculated.

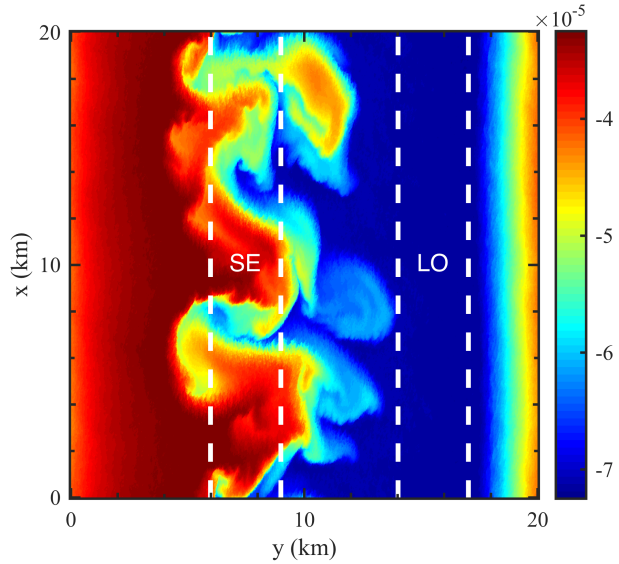

respect to the x-axis (which is aligned with the initial along-front orientation of the buoyancy filament). Additionally, the original uniform mixed layer depth of -50m has been modified throughout the domain by the deepening effects of Langmuir turbulence and the shallowing effects of restratifying submesoscale eddies. At the time of tracer introduction, the mixed layer depth based on the buoyancy threshold $\Delta b > (\Delta b)_c$, where $\Delta b \equiv [b(x,y,0) - b(x,y,z)]$ and $(\Delta b)_c = -0.53\text{ms}^{-2}$, ranges from roughly -30m to -55m. The mixed layer depth based on the critical Richardson number $\text{Ri}_c = 0.25$ ranges from -20m to -40m, and the depth based on the Ertel potential vorticity threshold $q(x,y,z) > q_c$, where $q_c = 8 \times 10^{-11}\text{s}^{-3}$, ranges from -30 to -60m. These different depths indicate a variety of mixing processes, including convective, Langmuir, and symmetric instabilities [4, 21, 53].

The physical domain size of the simulations is 20km×20km×-160m, with a computational grid of size 4096×4096×128, giving a horizontal resolution of ∼5m and a vertical resolution of ∼1m (a summary of these and other simulation parameters is provided in Table 2.1). For the Eulerian velocity field $\mathbf{u}$, periodic boundary conditions are used in horizontal $(x-y)$ directions, with no vertical velocity and a wind stress condition at the top boundary, and a stress-free condition at the bottom boundary. In the present study, the simulation was run for approximately 60 additional hours past the initial day 12 starting point; beyond 60 hours, submesoscale eddies along the unstable front have grown large enough to strongly affect the stable front. As shown in [4], substantial subsmesoscale structure has developed by day 12 of the spin-down problem, thereby allowing the simultaneous effects of submesoscale eddies and Langmuir turbulence to be studied prior to interaction of the stable and unstable fronts, which begins to occur near day 14. Analysis of tracer fields in this chapter has been primarily performed 8 hours after the tracers are introduced to the simulations. This particular time is chosen for the analysis in order to allow sufficient time for the tracer fields to develop so that robust insights into tracer evolution can be obtained, while also avoiding later times when the unstable and stable fronts begin to interact. Although the spin-down configuration examined here is an inherently non-stationary problem, all qualita-

Table 2.1: Summary of physical and computational parameters used in the numerical simulations. The turbulent Langmuir number is defined as $La_t = \sqrt{u_\tau / u_s(0)}$.

Physical size, $L_x \times L_y \times L_z$	20km×20km×-160m
Grid size, $N_x \times N_y \times N_z$	4096×4096×128
Grid Resolution, $\triangle_x \times \triangle_y \times \triangle_z$	4.9m×4.9m×1.25m
Reference density, ρ_0	1000 kg/m^3
Coriolis parameter, $\mathbf{f}$	$0.729\times10^{-4}\mathrm{s}^{-1}\hat{\mathbf{z}}$
Initial mixed layer depth, $H_{ML,0}$	-50m
Wind speed at 10m, U_{10}	5 m/s
Stokes drift velocity, $u_s(z = 0m)$	0.063 m/s
Turbulent Langmuir number, La_t	0.29
Stokes drift direction, ϑ_s	30°
Wind friction velocity, u_τ	5.46×10^{-3} m/s
Wind shear, τ	0.025 N/m^2
Wind direction, ϑ_w	30°

tive trends and conclusions obtained from results at 8 hours have been checked for robustness by comparing with results at other times. Any cases where trends and conclusions change substantially as functions of time are noted in the text.

Twelve different tracer fields are introduced to the simulations at day 12: (*i*) five passive air-sea boundary flux tracers (referred to as c_{Hi}, where $i = 1, 2, \ldots, 5$) and (*ii*) seven passive, initial finite source tracers (referred to as c_{Ij}, where $j = 1, 2, \ldots, 7$). The air-sea boundary flux tracers, summarized in Table 2.2, each have specified flux rates across the upper boundary given by Henry's law for diffusive flux of a gas across the air-sea interface [79, 80], namely

$$F_i = k_i(c_{air} - c_{Hi,0})\,, \tag{2.6}$$

where F_i is the downward flux rate across the boundary for the ith air-sea tracer (i.e., c_{Hi}), k_i is the tracer flux rate, or piston velocity, for each tracer, c_{air} is the concentration in air, or the partial pressure of the gas to be dissolved just above the boundary scaled by the Henry's law constant, and $c_{Hi,0}$ is the gas concentration c_{Hi} just below the boundary (initialized to 0 at the start of the simulation). The value of c_{air} is fixed at 1 in this study.

Each of the five air-sea flux tracers has a different constant value of k_i, as shown in

Table 2.2: Summary of tracers diffused across the air-sea interface according to Henry's Law in Eq. (2.6), showing the tracer flux rate, k_i, and corresponding characteristic transfer time scale, τ_i. Ratios of characteristic large scale τ_S and small scale τ_L fluid time scales relative to $\tau_i = h/k_i$ are also shown, where $\tau_S = h/w_s \approx 2 \times 10^7$s [1] and $\tau_L = h/\sqrt{\langle w'^2 \rangle} \approx 10^4$s.

Tracer c_{Hi}	k_i (m·s^{-1})	τ_i (s)	τ_S/τ_i	τ_L/τ_i
c_{H1}	2×10^{-2}	2.5×10^{3}	8×10^{3}	4
c_{H2}	2×10^{-3}	2.5×10^{4}	8×10^{2}	4×10^{-1}
c_{H3}	2×10^{-4}	2.5×10^{5}	8×10^{1}	4×10^{-2}
c_{H4}	2×10^{-5}	2.5×10^{6}	8	4×10^{-3}
c_{H5}	2×10^{-6}	2.5×10^{7}	8×10^{-1}	4×10^{-4}

Table 2.2. The range of tracer flux rates k_i for c_{H1}-c_{H5} in Table 2.2 has been chosen to span a range of timescales that match the characteristic timescales of both submesoscale eddies, where $\tau_S \approx 10^7$s, and Langmuir turbulence, where $\tau_L \approx 10^4$s. They can also be interpreted as representing a range of Schmidt (Sc) numbers for different gases, using the formula of [79] and the 5m/s windspeed corresponding to the modeled wind stress, namely

$$k_i = 0.31u^2\sqrt{\frac{660}{Sc}}\,. \tag{2.7}$$

This relation already includes the effects of ocean turbulence to some degree as it is based on observations [see the discussion in 81], while here turbulence plays an active role in setting the flux rate. These values should only be considered as a guide to order of magnitude. With this caveat, the Schmidt number for the fastest air-sea velocity ranges from 10^{-3} for c_{H1} to 10^5 for c_{H5}. Thus, for typical gases (e.g., CO_2, oxygen, and chlorofluorocarbons) and typical surface seawater temperature and salinity, the c_{H3} and c_{H4} tracers span the realistic range (where $Sc = 660$ for CO_2 in seawater at 20°C [79]). A wider range of values is used, so that the effects of transfer fast enough to rival Langmuir turbulence and slow enough to rival submesoscale processes can be examined. With these values for k_i, the ratio τ_S/τ_i extends from 8×10^3 to 8×10^{-1} when going from c_{H1} to c_{H5}, while τ_L/τ_i extends from 4 to 4×10^{-4} from c_{H1} to c_{H5}. Whenever these ratios are $\mathcal{O}(1)$, we may expect strong interactions between fluid dynamics and tracer uptake, so the present range of air-sea flux velocities crosses this threshold for both Langmuir and submesoscale turbulence. The choice of values for k_i in

Table 2.2, combined with the scale separation between submesoscale and Langmuir processes enabled by the wide range of scales in the simulations, allows an examination of the separate effects of submesoscale eddies and small-scale Langmuir turbulence on tracer distributions and evolution. All of the tracer fluxes in the simulations are observed to be exclusively from the air to the ocean, thus assuming an infinite reservoir of tracer and a rapid refreshing of the surface air above the ocean. Each of the tracers have periodic boundary conditions in horizontal directions, with no vertical fluxes at the bottom boundary and top boundary fluxes given by Eq. (2.6).

In a well-mixed layer of approximately constant depth h, the concentration of a tracer c_{Hi} subject to the flux law specified in Eq. (2.6) should increase as

$$c_{Hi} = c_{air}\left(1 - e^{-tk_i/h}\right) = c_{air}\left(1 - e^{-t/\tau_i}\right). \tag{2.8}$$

Thus, in Table 2.2, the timescale $\tau_i = h/k_i$ is used to categorize the rate of air-sea flux, where h is estimated as the initial mixed layer depth of -50m. This timescale is compared to $\tau_L = O(h/\sqrt{\langle w^2 \rangle})$ based on Langmuir vertical velocities from the simulation and $\tau_S \approx h/w_S$, where w_S is estimated as the eddy-induced vertical velocity resulting from the restratification streamfunction of [1]. If there is no turbulent transport or mixing, then only the surface grid cell would absorb tracer and it would saturate $h/\Delta z$ times faster, followed by spreading across the mixed layer on much slower diffusive timescales. For mixed layers that have not yet become fully saturated with tracer, turbulent diffusion provides much more rapid transport away from the surface, thereby maintaining a greater air-sea flux rate since surface waters are continually refreshed. It should be noted, however, that after the entire mixed layer becomes fully saturated, the air-sea flux rate will decrease regardless of the effects of turbulent diffusion, since only through the slow process of entrainment of water from below the mixed layer can any tracer-free water be brought near the surface.

The initial finite source tracers, denoted c_{Ij}, are conserved after their introduction to the domain at day 12, unlike the air-sea flux tracers. These finite source tracers are

distinguished by their different initial source locations, where the initial condition is given as

$$c_{Ij}(\mathbf{x}, t_0) = \begin{cases} 1 & \text{if } z = z_j \\ 0 & \text{otherwise} \end{cases}, \tag{2.9}$$

where t_0 denotes the initial time and z_j is the depth at which the tracer is introduced. The tracer concentration is initially uniform for all x and y at the given depth z_j, and the tracers are initialized over two grid cells in the vertical direction, giving an initial tracer field of depth 2.5m. The different values of z_j for the tracers in the present simulation are given in Table 2.3, where c_{I1} is a tracer released at the surface, c_{I7} is released at $z = -60$m, which is below the initial pycnocline of $H_{ML,0} = -50$m, and the other five initial source tracers are incrementally distributed at different depths within the mixed layer. Two of the finite initial concentration tracers (c_{I1} and c_{I7}, respectively) have been chosen to represent the initial source locations of tracers that typically originate at the surface, such as phytoplankton, and tracers typically stored at depth, such as nutrients. Tracers c_{I5} and c_{I6} are initialized at depths near which the pycnocline undergoes substantial variations due to the interplay between submesoscale eddies and Langmuir turbulence. At these depths, the influence of the near-surface convective boundary layer and a deeper layer unstable to symmetric instabilities, which are associated with submesoscale eddies, compete and give rise to widely different tracer distributions. Once again, each of the tracers have periodic boundary conditions in

Table 2.3: Summary of tracers released at different locations in the oceanic mixed layer. The initial tracer locations z_j are normalized in the last column by the initial mixed layer depth in the simulations, $H_{ML,0} = -50$m.

Tracer c_{Ij}	Physical location	z_j (m)	$z_j/H_{ML,0}$
c_{I1}	Surface	0	0
c_{I2}	Shallow mixed layer	-10	0.2
c_{I3}	Middle mixed layer 1	-20	0.4
c_{I4}	Middle mixed layer 2	-30	0.6
c_{I5}	Deep mixed layer	-40	0.8
c_{I6}	At initial pycnocline	-50	1
c_{I7}	Below initial pycnocline	-60	1.2

horizontal directions, but for the initial source tracers there are zero vertical flux conditions at both the top and bottom boundaries.

It should be noted that although the tracers included in the simulations are idealized, they are intended to provide insights into tracers relevant to the biogeochemistry of the upper ocean. The air-sea flux tracers provide insights into transport of chemical species and gases transferred at the air-sea interface. Similarly, the initial source tracers provide insights into biologically-relevant tracers that reside near the surface, such as phytoplankton or oil (e.g., c_{I1} and c_{I2}), and at depth, such as nutrients (e.g., c_{I6} and c_{I7}). The use of idealized tracers in the current study is consistent with the present focus on understanding the fundamental interactions between passive tracers and realistic submesoscale ocean turbulence. The tracers themselves are idealized in order to perform a parametric study of the effects of different initial source locations and surface flux rates on tracer properties. In the future, the present results will inform understanding of distributions and the evolution of more realistic tracers in the upper ocean.

2.3 Properties of Mixed Layer Tracers

Four primary metrics are used in the present analysis to examine the properties and evolution of tracers in the upper ocean: (*i*) three-dimensional (3D) concentration fields, which provide a qualitative understanding of tracer distributions, (*ii*) vertical profiles of $x-y$ averaged tracer concentrations, variances, and vertical fluxes, (*iii*) one-dimensional (1D) spectra calculated in the along-front direction (i.e., the x-direction, see Fig. 2.2), and (*iv*) multiscale vertical fluxes of both active (i.e., buoyancy) and passive tracers. In the following, these metrics are calculated for the air-sea flux tracers c_{H1}-c_{H5} (summarized in Table 2.2) and for the initial source tracers c_{I1}-c_{I7} (Table 2.3). Additional tracer properties related to modeling of tracer transport and phytoplankton production are examined in later sections.

The analysis herein is performed separately for different subsets of the domain, as shown

in Fig. 2.2. These subsets include the small-scale turbulence-dominated region between $y \simeq 14 - 17$km in Fig. 2.2 and the combined small-scale turbulence and large-scale eddy region between $y \simeq 6 - 9$km. The bounds of these regions are adjusted as the simulation progresses and the unstable front shifts to smaller y as a result of Ekman transport. These two regions are referred to in the following as the Langmuir only (LO) and submesoscale eddy (SE) regions, respectively.

In several cases in the following analysis, horizontal $(x - y)$ averages are calculated separately in the LO and SE regions. In these two regions, y averaging is performed only over the respective y bounds of the LO and SE regions, and averaging in the x direction is performed over the entire length of the domain since the flow fields are statistically homogeneous in the along-front direction. Horizontal spatial averages in these reduced-size regions are denoted $\langle\phi\rangle_{xy_*}$, where ϕ is a given flow or tracer quantity. Averages over the full 3D volume, which are used to normalize some of the results for the air-sea flux tracers, are denoted $\langle\phi\rangle_{xyz}$.

2.3.1 Air-Sea Flux Tracers

Figure 2.3 shows instantaneous 3D concentration fields for c_{H1}-c_{H3} and c_{H5} approximately 8 hours after the tracers are introduced to the simulations. The fields are each normalized by the average concentration calculated over the full 3D volume. Figure 2.3 shows that as tracer flux rate decreases, submesoscale features are increasingly visible in the normalized concentration fields. The fastest-injected tracer, c_{H1}, rapidly saturates (defined here as reaching the concentration in air of $c_{air} = 1$) the near-surface region and then the mixed layer, resulting in overall less horizontal and vertical variability of the tracer relative to the average concentration. Tracers c_{H3} and c_{H5} (the concentration field for c_{H4}, not shown, is similar), have less uniform concentrations in the vertical direction, with higher tracer concentrations near the surface. These tracers also have considerably more horizontal submesoscale variability than the tracers with faster flux rates.

Figure 2.3: Instantaneous snapshots of 3D tracer concentration fields for (a) c_{H1}, (b) c_{H2}, (c) c_{H3}, and (d) c_{H5} approximately 8 hours after the tracers are introduced to the simulations. The concentrations are normalized by the volume-averaged concentration $\langle c_{Hi} \rangle_{xyz}$ for each tracer.

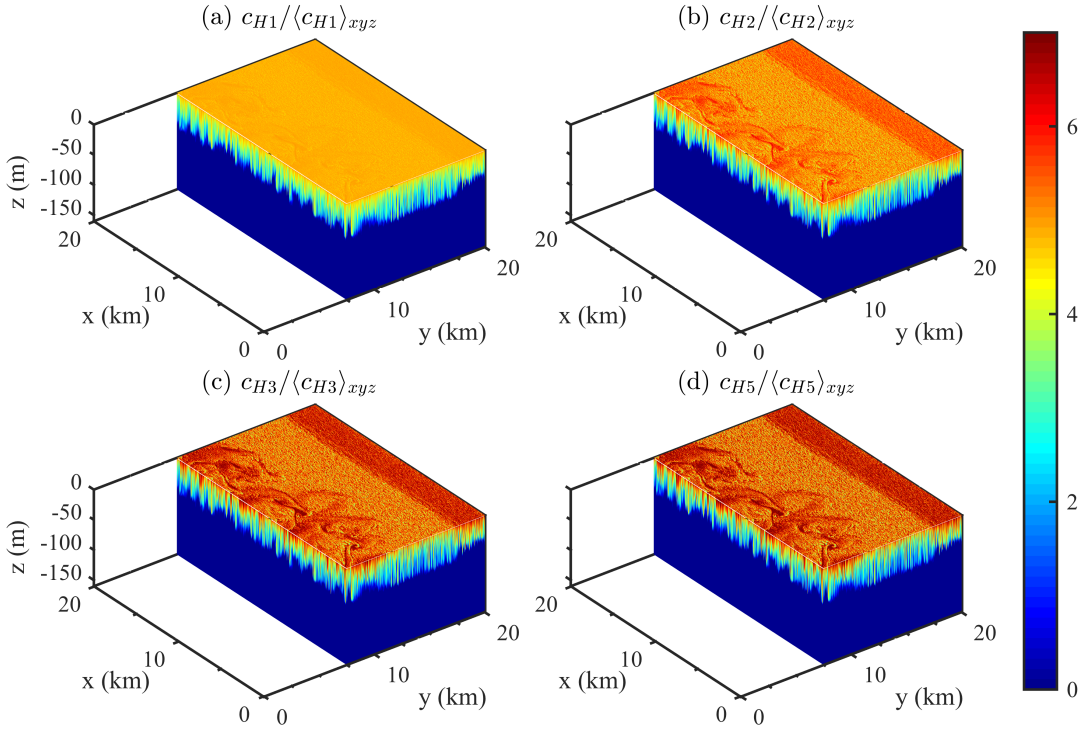

The saturation of the mixed layer for c_{H1} and c_{H2} can be seen quantitatively from the vertical profiles of average tracer concentration $\langle c_{Hi} \rangle_{xy*}$, vertical flux $\langle w' c'_{Hi} \rangle_{xy*}$, and tracer variance $\langle c'^2_{Hi} \rangle_{xy*}$ in Fig. 2.4. Panels (a)-(c) of this figure show tracer statistics after 1 hour and panels (d)-(f) show statistics after 8 hours. At early times, Fig. 2.4(a) shows that only concentrations of c_{H1} very near the surface have begun to approach the saturated value of $c_{air} = 1$, and there is still substantial vertical mixing of c_{H1} into the lower half of the domain, as shown in Fig. 2.4(b). At later times, however, Fig. 2.4(d) shows that the average concentrations of c_{H1} and c_{H2} are both close to 1 (i.e., the saturated value) down to a depth of $z \approx -40$m, effectively spanning the entire mixed layer. As a result, the difference $(c_{air} - c_{Hi,0})$ in the surface flux rate from Eq. (2.6) is small, resulting in reduced vertical tracer transport. This can be seen explicitly by comparing Figs. 2.4(b) and (e), where at

Figure 2.4: Vertical profiles of (a,d) average tracer concentration $\langle c_{Hi} \rangle_{xy*}$, (b,e) vertical tracer flux $\langle w' c'_{Hi} \rangle_{xy*}$, and (c,f) tracer variance $\langle c'^2_{Hi} \rangle_{xy*}$ for c_{H1}-c_{H5}. Panels (a)-(c) and (d)-(e) show profiles 1 and 8 hours after tracers are introduced to the simulations, respectively. Results are shown for the SE region (solid lines) and the LO region (dashed lines).

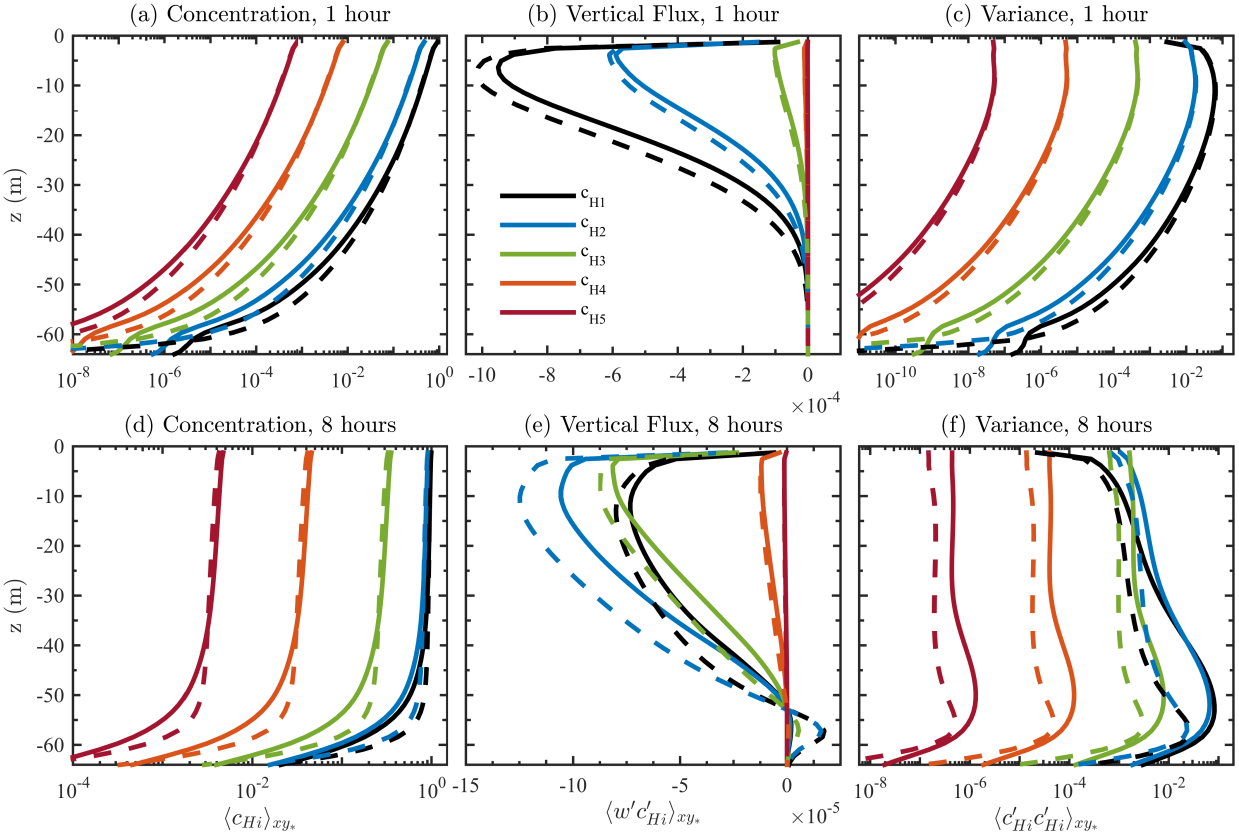

early times the vertical fluxes of c_{H1} and c_{H2} are much larger than for the other tracers, while at later times the flux of c_{H1} is actually smaller near the surface than that of both c_{H2} and c_{H3}. Similarly, comparison of Figs. 2.4(c) and (f) shows that the variances of c_{H1} and c_{H2} decrease near the surface at later times and that the variance of c_{H1} is lower than the variances of c_{H2} and c_{H3}.

Saturation of the mixed layer for c_{H1} and c_{H2} at later times is also evident in the time series of total tracer concentrations shown in Fig. 2.5. The average concentration in the mixed layer increases with time for all tracers, and an overall greater amount of tracer is present in the domain for larger k_i. Figure 2.5 shows, however, that there is a decrease in the

Figure 2.5: Time series of average tracer concentrations, $\langle c_{Hi} \rangle_{xy_*z}(t)$, in the 3D simulation volume, where averaging in the z direction is performed from $z = 0$ to -40m. Results are shown for the SE region (solid lines) and the LO region (dashed lines).

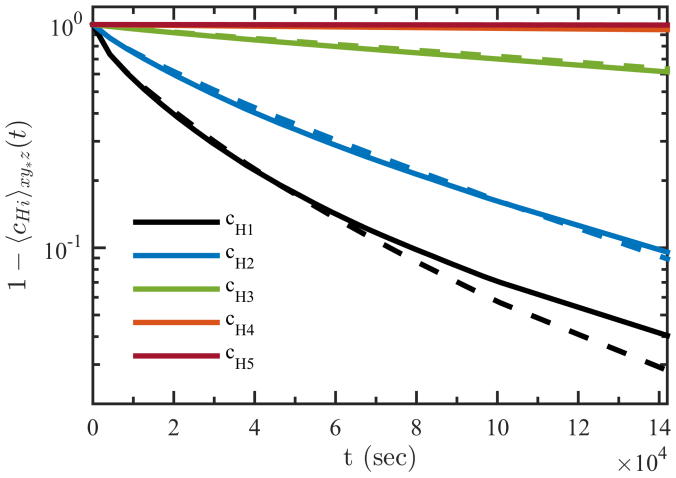

rate at which the tracer enters the domain for c_{H1} and c_{H2}. This occurs since vertical mixing is no longer effective at reducing the near surface tracer concentration when the mixed layer becomes saturated, resulting in smaller $(c_{air} - c_{Hi,0})$ and lower surface flux rates via Eq. (2.6).

In addition to the differences between c_{H1}-c_{H5} resulting from the different surface flux rates k_i, Figs. 2.3-2.5 indicate that there are also substantial differences in a given tracer field between the LO and SE regions, and that these differences depend on k_i. Within the LO region in Fig. 2.3, all tracers exhibit the same deeper penetration into the mixed layer as compared to the SE region. This is consistent with the dominance of small-scale Langmuir circulations in this region. An increase in vertical transport and a corresponding deepening of the mixed layer depth are known characteristics of Langmuir turbulence, as is a tendency toward restratification and suppression of turbulence by submesoscale eddies [4]. The increased penetration depth in the LO region is shown quantitatively in Fig. 2.4(d), where average tracer concentrations remain larger to greater depths in the LO region. This increased penetration is accompanied by an increase in the vertical flux in the LO region,

as shown in Figs. 2.4(b) and (e) (turbulent diffusivity is also larger in the LO region than in the SE region, as will be discussed in Section 2.4). The increased vertical flux also leads to a small decrease in surface concentrations within the LO region, as shown in Fig. 2.4(d). This represents the "flushing" of the surface layer by Langmuir turbulence, which in turn allows for an increase in the tracer flux rate into the domain at the air-sea interface, and an overall increase in tracer uptake in this region.

Figure 2.5 shows that the amount of tracer brought into the domain for tracer c_{H1} is larger in the LO region as compared to the SE region. This holds true for all tracers, although the difference is less pronounced for tracers with lower k_i (i.e., $c_{H2} - c_{H5}$). Similarly, the vertically-integrated tracer concentrations in Fig. 2.6 show that relative to tracer concentrations in the SE region, there is more tracer concentration in the LO region for

Figure 2.6: Vertically-integrated (top row) and corresponding x-z integrated (bottom row) tracer concentrations for (a) c_{H1}, (b) c_{H2}, (c) c_{H3}, and (d) c_{H5} approximately 8 hours after the start of the simulations. The vertical integration is performed for all N_z =128 gridpoints in the z direction and the horizontal integration is performed for all N_x = 4096 gridpoints in the x direction. The field and line plots are normalized by the full 3D volume-averaged concentrations $\langle c_{Hi} \rangle_{xyz}$. Here $[c_{Hi}]_{xz}$ denotes a concentration integrated in both the x and z directions, vertical dashed lines indicate the SE and LO regions, and horizontal gray bands in the bottom row represent the difference between the average x-z integrated concentrations of the LO and SE regions.

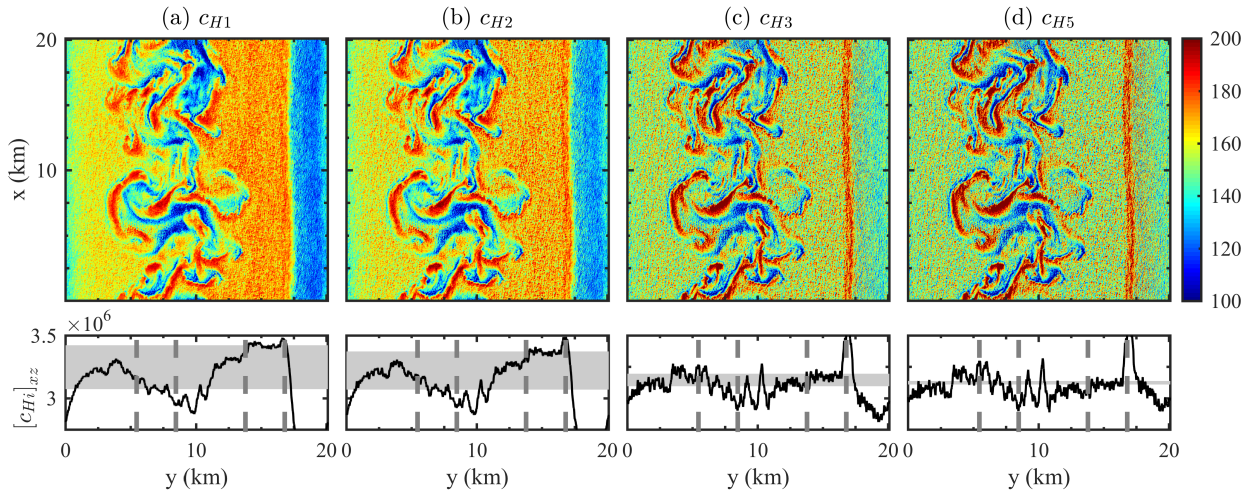

c_{H1} and c_{H2}, but the difference between the LO and SE regions decreases as k_i decreases. This trend is most likely due to the requirement that vertical mixing must be fast in order to overcome fast surface flux rates for high k_i; recall that in order for substantial vertical transport to occur via Eq. (2.6), a large difference between c_{Hi} and c_{air} must be maintained at the surface. Fast vertical circulations, which exist primarily in the LO region, are thus required to effectively introduce tracer to the domain. Overall, the increased vertical mixing in the LO region results in more uniform tracer concentrations, as indicated by the reduced tracer variance in the LO region as compared to the SE region shown in Fig. 2.4(f).

The dynamics are more complicated in the SE region where both large-scale eddies and small-scale Langmuir turbulence are active. Figure 2.3 shows that there are ridges of high tracer concentration that penetrate deep into the mixed layer, corresponding to the structures of larger submesoscale eddies and associated strong vertical jets. In between these ridges are regions near the surface dominated by smaller-scale structures similar to those in the LO region. As shown in Fig. 13 of [4], however, there is overall less penetration of these small-scale structures to depth when compared to the LO region, resulting in a shallower mixed layer in the SE region due to restratification by submesoscale eddies. The fields of vertically-integrated tracer concentration for c_{H1}-c_{H3} and c_{H5} in Fig. 2.6 show that there are large variations in the amount of tracer that has entered the domain in the SE region, with both the largest and the smallest local amounts of tracer found in the SE region.

It is important to contrast the effects of submesoscale eddies on passive tracer uptake and transport with their effects on buoyancy transport. Submesoscale eddies consistently transport buoyancy upward and extract kinetic energy from potential energy by lifting light parcels and sinking dense parcels [1, 18]. However, the reduction in passive tracer uptake in the SE region compared to the LO region, as shown in Figs. 2.3-2.5, cannot be explained by the mechanism of potential energy extraction alone, because there is no reason why tracer concentrations should correlate with submesoscale features without an intervening mechanism. Specifically, vertical transport of passive tracers by submesoscale eddies is only

indirectly related to vertical restratification of the mixed layer by such eddies. Figure 2.4(e) shows that vertical tracer flux is roughly 10-20% weaker in the SE region than in the LO region, but the vertical velocities associated with submesoscale eddies are only a hundredth those of Langmuir turbulence. Furthermore, in the cases where the difference is largest (e.g., c_{H1} and c_{H2}), there is little imprint of submesoscale eddies on surface concentrations [see Fig. 2.3(a)], indicating that the variation in the effects of vertical transport by such eddies near the surface is overshadowed by the rate of the incoming tracer. However, submesoscale features strongly suppress turbulence through their restratifying effects. The same is true of the stable front near $y = 20$km; this front has wind-driven restratification that suppresses turbulence (Fig. 2.3 shows uniform surface confinement of tracer concentrations between $y = 18 - 20$km, which can be interpreted as indicative of suppressed turbulence and is discussed in more detail in [4]). Care is needed in interpreting the effects of vertical fluxes carried by submesoscale features, as their vertical velocity scale is large when compared to mesoscales but diminutive when compared to boundary layer turbulence. The evidence here is that their indirect, restratifying effect is significantly more important for determining vertical passive tracer fluxes than their direct passive tracer flux.

In order to further quantify the properties of air-sea flux tracers in different flow regions and for different values of k_i, tracer spectra and their scaling exponents provide quantitative measures by which distributions of tracers can be characterized. Figure 2.7 shows 1D spectra in the x direction for tracers c_{H1}-c_{H3} and c_{H5} in the LO and SE regions at a depth of $z = -25$m. The spectra are shown as a function of wavenumber (k), with small wavenumbers corresponding to larger scales (e.g., submesoscale eddies) and larger wavenumbers corresponding to smaller scales (e.g., Langmuir turbulence).

Figure 2.7 shows that for all k_i, there is very little large-scale energy content in the LO region, particularly when compared to the SE region. This is due to the lack of any large-scale eddies in the LO region, as can be seen from the 3D volumes in Fig. 2.3. In the SE region, there is more energy at large scales, with a noticeable peak in the spectra at a spatial

Figure 2.7: Spectra along the x direction at a depth of z = -25m for tracers (a) c_{H1}, (b) c_{H2}, (c) c_{H3}, and (d) c_{H5} approximately 8 hours after the start of the simulations. The gray dash-dot lines show spectral slopes in the submesoscale and Langmuir-scale regions, and the vertical red dash-dot lines show the characteristic lengthscale of submesoscale eddies at 5km.

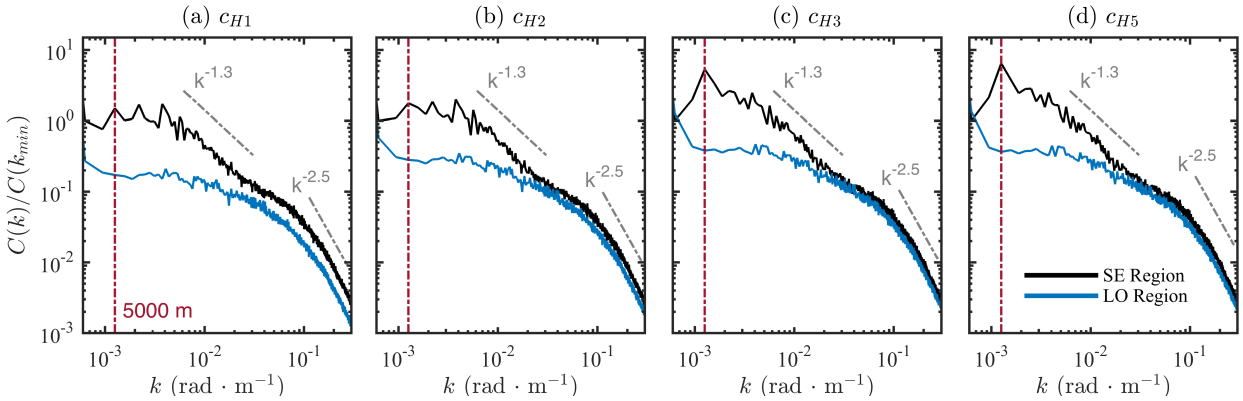

scale of 5km, roughly corresponding to the characteristic lengthscale of submesoscale eddies in the simulations. This peak is more pronounced for c_{H3}-c_{H5} where k_i is small, indicating that submesoscale eddies have a greater impact on tracer distributions when the timescales of these eddies and the surface flux rates are more closely matched (in particular, Table 2.2 shows that $\tau_S/\tau_i \sim 1$ for c_{H4}).

There are also much less pronounced peaks in all of the spectra in Fig. 2.7 at a spatial scale close to 10m, corresponding to the effects of small-scale Langmuir turbulence. In general, the spectra in the LO and SE regions are similar at small scales, but for c_{H1} where k_i is large there is overall less small-scale variance in the LO region as compared to the SE region. This is most likely due to reduced vertical transport in the SE region, which becomes particularly pronounced for high k_i, as well as to the lack of down-scale transfer of tracer variance in the LO region, where significant large-scale activity is absent.

Two distinct spectral slopes exist in the large- and small-scale regions of the spectra shown in Fig. 2.7. At large scales there is an approximate $k^{-1.3}$ slope in all of the spectra in the SE region and at small scales there is an approximate $k^{-2.5}$ scaling in both the LO and SE regions. By contrast, the scalings of buoyancy and kinetic energy spectra in the submesoscale

range are k^{-2} or steeper [Fig. 3 of 4], consistent with the idea that larger variance across the submesoscale range results from the extraction of potential energy by eddies. It should be noted that connecting the small-scale spectral decay with either a three-dimensional cascade or dissipative processes requires that further higher resolution simulations be performed in the future.

2.3.2 Initial Source Tracers

Figure 2.8 shows instantaneous 3D volumes for tracers c_{I1} and c_{I5}-c_{I7} (Table 2.3 shows the initialization depths). The surface tracer c_{I1} in Fig. 2.8(a) is distributed throughout the vertical extent of the mixed layer on a relatively short time scale, with very little indication remaining of its initial release location. This is shown quantitatively in Fig. 2.9(a) where

Figure 2.8: Instantaneous snapshots of 3D tracer concentration fields for (a) c_{I1}, (b) c_{I5}, (c) c_{I6}, and (d) c_{I7} approximately 8 hours after the tracers are introduced to the simulations. The color scale is logarithmic.

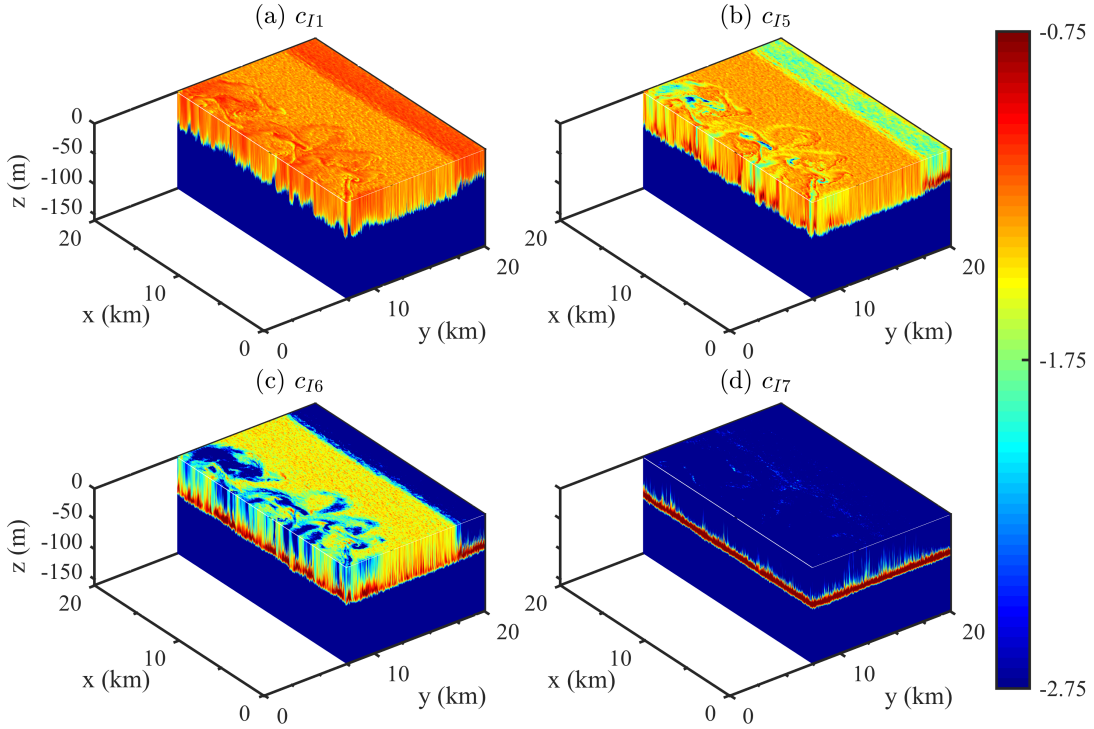

Figure 2.9: Vertical profiles of (a,d) average tracer concentration $\langle c_{Ij} \rangle_{xy*}$, (b,e) vertical tracer flux $\langle w' c'_{Ij} \rangle_{xy*}$, and (c,f) tracer variance $\langle c'^2_{Ij} \rangle_{xy*}$ for c_{I1}-c_{I4} in (a)-(c) and for c_{I5}-c_{I7} in (d)-(e). Results are shown approximately 8 hours after the start of the simulations for the SE region (solid lines) and the LO region (dashed lines). Horizontal dotted lines indicate the initial locations for each tracer.

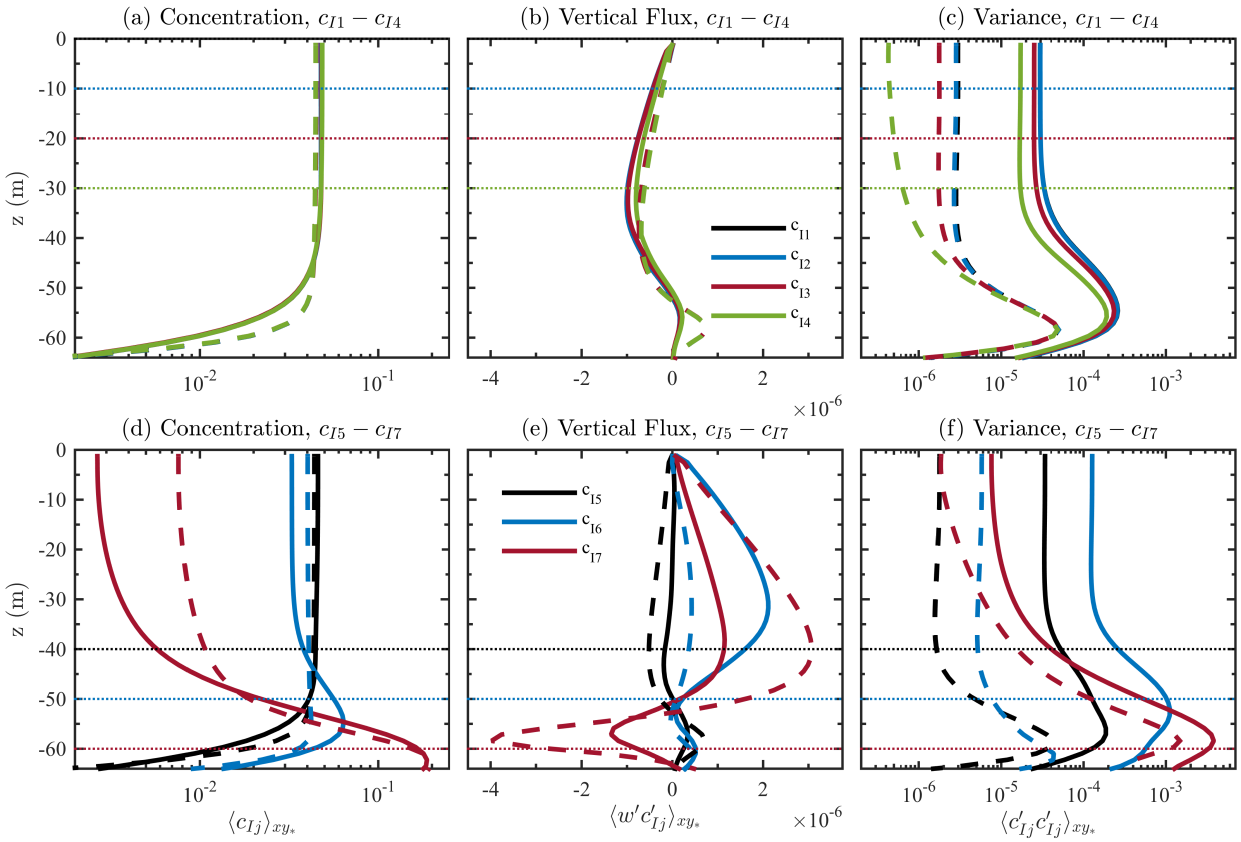

tracers c_{I1}-c_{I4} have essentially identical vertical profiles of average concentration $\langle c_{Ij} \rangle_{xy*}$. Figure 2.9(b) shows that vertical fluxes for these four tracers are also quite similar, with $\langle w'_i c'_{Ij} \rangle_{xy*} < 0$ over nearly the entire mixed layer. These negative fluxes represent downward transport of high tracer concentrations to greater depths throughout the mixed layer, along with entrainment of lower concentration water that is transported upwards. Below the mixed layer base, positive tracer fluxes are consistent with the gradient in tracer concentration in the partly stratified water. As a result of this vertical transport, tracers c_{I1}-c_{I4} are uniformly mixed down to roughly $z = -40$m, as shown by the variance profiles in Fig. 2.9(c).

Although c_{I1}-c_{I4} have largely identical properties since all of these tracers exist in the upper reaches of the mixed layer where vertical mixing is generally strong, Figs. 2.9(b) and (c) do show that the vertical flux and variance for c_{I4} are smaller in magnitude than for c_{I1}-c_{I3}. These differences become even more pronounced for c_{I5}-c_{I7}, and Fig. 2.8 shows that tracers c_{I6} and c_{I7} are still largely concentrated at their release depths, even within the LO region where mixing is enhanced. Figure 2.9(d) shows that there is reduced tracer concentration within the mixed layer as the initial source location deepens, with concentrations of c_{I7} in the mixed layer nearly an order of magnitude smaller than the concentrations of c_{I5} and c_{I6} [the same reduced mixed layer concentrations are also evident in Fig. 2.8(d)]. As a result of the lower release locations for c_{I5}-c_{I7}, the dominant transport of tracer concentration occurs upward, resulting in positive fluxes $\langle w'c'_{Ij}\rangle_{xy_*}$ for c_{I6} and c_{I7} in Fig. 2.9(e). As with tracers c_{I1}-c_{I4}, variances of c_{I5}-c_{I7} become relatively uniform within the mixed layer, as shown in Fig. 2.9(f).

Tracer variance is generally largest below the mixed layer base regardless of tracer release location and concentration profile. Three phenomena explain this effect. First, there is a transition layer where the most energetic downward plumes are able to transiently, but not uniformly, inject tracer into the stratified region. Second, there are many internal waves traveling along this stratification, triggered by the initiation of the model as well as the turbulence above and the shear. Third, there are inertial oscillations and submesoscale motions capable of triggering intermittent shear instabilities. The degree to which tracer variance is increased below the mixed layer is somewhat less pronounced in the SE region than in the LO region, partly due to the greater variability in mixed layer depth due to restratification by submesoscale eddies. Moreover, it is significant that Langmuir turbulence is able to enhance vertical mixing even for tracers released below the average location of the pycnocline (i.e., tracer c_{I7}). A more thorough investigation is warranted, but is beyond the scope of this paper.

As with the air-sea flux tracers discussed in the previous section, Figs. 2.8 and 2.9

also indicate that there are substantial differences in tracer properties in the LO and SE regions. Figure 2.8 shows that there is generally less tracer variability in the LO region as compared to the SE region, and that tracers are carried to greater depths in the LO region. The deeper tracer penetration is evident from the average concentration profiles in Fig. 2.9(a). This figure also shows that tracer concentrations are generally smaller in the LO region within the mixed layer, due to the conserved nature of the c_{Ij} tracers and the greater vertical extent over which the tracers are spread in the LO region. Figure 2.9(c) shows that tracer variance is smaller in the LO region, consistent with the qualitative picture provided by the 3D volumes in Fig. 2.8.

It is interesting to note that downward vertical flux is in fact stronger in the SE region than in the LO region, as shown in Fig. 2.9(b). This could either be due to the increased homogeneity of the tracer field in the LO region, or to the effectiveness of larger-scale vertical transport by submesoscale eddies in the SE region. However, as was argued before, the general effect of submesoscale eddies seems to be inhibition of turbulence, so the former is the more likely. The other front, which is wind-restratified and stable to submesoscale features, also strongly suppresses turbulence (see Fig. 2.8). As a result, the entrainment of tracers is significantly suppressed by both fronts, stable and unstable.

Differences between the LO and SE regions change somewhat for tracers c_{I5}-c_{I7}. Figure 2.8(c) shows that there are large regions near the unstable front where very little tracer concentration has been transported upwards to the surface. By contrast to the results for c_{I1}-c_{I4}, Fig. 2.8(c) actually indicates that there is more tracer above the mixed layer base and near the surface in the LO region as compared to the SE region. This is confirmed quantitatively in Fig. 2.9(d) where average tracer concentrations for c_{I6} and c_{I7} are generally larger in the LO region than in the SE region. Similarly, the vertical flux becomes substantially stronger in the LO region than in the SE region for c_{I7}, as shown in Fig. 2.9(e). These results indicate that for tracers released at depth, there is substantially enhanced vertical mixing in the LO region where Langmuir turbulence is dominant, and suppression of

vertical mixing in the submesoscale region tends to outweigh the additional vertical transport by submesoscale eddies themselves. This simulation example demonstrates that the combined passive tracer vertical transport by submesoscale and Langmuir turbulence is not just a simple addition of their individual fluxes; in the combined system these process are coupled through the intermediary of their effects on stratification and shear. At least for the tracers considered here, it is therefore critical to consider the driving of turbulence by surface forcing, and turbulence-submesoscale suppression or other interactions must be resolved or well-parameterized in order to capture this effect.

Another conceptual picture that emerges from Figs. 2.8 and 2.9 is that of a two-layer structure within the mixed layer, based on potential vorticity and symmetric instability. [21] have previously identified these two layers, which are distinguished by their different mechanisms of turbulence production: (*i*) in the *convective* layer, turbulence is generated by surface waves and fast buoyancy-driven instabilities, and is characterized by vertically uniform buoyancy fields, and (*ii*) in the *symmetric instability* layer, turbulence is driven by slower overturning symmetric instabilities due to slumping of lateral density gradients under the influence of rotation, and is characterized by vertical uniformity in potential vorticity. As found in [4], the transition depth between these two layers, defined by the buoyancy threshold, varies substantially between the SE and LO regions. Within the LO region, the effects of the convective layer penetrate more deeply and suppress the height of the second layer such that there is little to no symmetric instability layer before the onset of interior ocean stratification. In the SE region, the convective layer is significantly shallower, allowing for larger impacts of symmetric instabilities.

The present results provide further insights into the characteristics and locations of these two layers. Tracers c_{I1}-c_{I3} have been released fully in the convective layer and thus quickly mix throughout the full vertical extent of the mixed layer. Tracers c_{I6} and c_{I7} have been released at locations that lie primarily in the symmetric instability layer, particularly in the SE region, and thus there is significantly less vertical transport than in the LO region,

or than for c_{I1}-c_{I3}. Tracers c_{I4} and c_{I5}, which have initial sources at $z = -30$m and -40m, respectively, are released near the average transition between the convective and symmetric instability layers. In combination with the results from [4], the present results indicate that the localized depth at which this transition occurs varies between a maximum of roughly $z = -30$m within the SE region and a minimum of roughly $z = -60$ m within the LO region. Within the LO region, the convective layer is deepened by the effects of Langmuir turbulence, maintaining a bridge between the rapid convective layer mixing processes and the tracer stored lower down, enabling relatively large concentrations to still be quickly pulled up to the surface. However, within the SE region, the effects of Langmuir turbulence are weaker and the convective layer is shallower, cutting off this bridge and effectively lengthening the time scale of vertical transport in this region. Even though much of the SE region allows symmetric instability, which can reach more deeply than convective instability, the overall suppression of turbulence by submesoscale restratification wins out. For tracers to be brought to the surface, they first need to be transported vertically up to the depth of the convective layer via upwelling jets and symmetric instabilities associated with submesoscale eddies, which occur in compact, localized, and intense patches on much slower time scales. From here, the convective layer can then take over and rapidly transport the tracer upwards.

Finally, distributions of tracers can be quantitatively characterized using the spectra shown in Fig. 2.10. As with the air-sea flux tracer spectra shown in Fig. 2.7, there are spectral peaks near the submesoscale eddy characteristic lengthscale of 5km and the Langmuir lengthscale of 10m for the initial tracer spectra shown in Fig. 2.10. At small scales, the spectra follow a roughly $k^{-2.4}$ scaling for all tracers, similar to the $k^{-2.5}$ scaling observed at small scales for the air-sea flux tracers in Fig. 2.7. By contrast to the air-sea flux tracer results, however, the initial source tracers have generally steeper scaling laws in the submesoscale range (spanning $k^{-2.4}$ to $k^{-2.1}$), indicating that submesoscale feedback on air-sea fluxes plays an important role in establishing these spectra.

Figure 2.10: Spectra along the x direction at a depth of z = -25m for tracers (a) c_{I1}, (b) c_{I5}, (c) c_{I6}, and (d) c_{I7} approximately 8 hours after the start of the simulations. The light gray dashed lines show spectral slopes in the submesoscale and Langmuir-scale regions, and the vertical dashed lines show the characteristic lengthscale of submesoscale eddies at 5km.

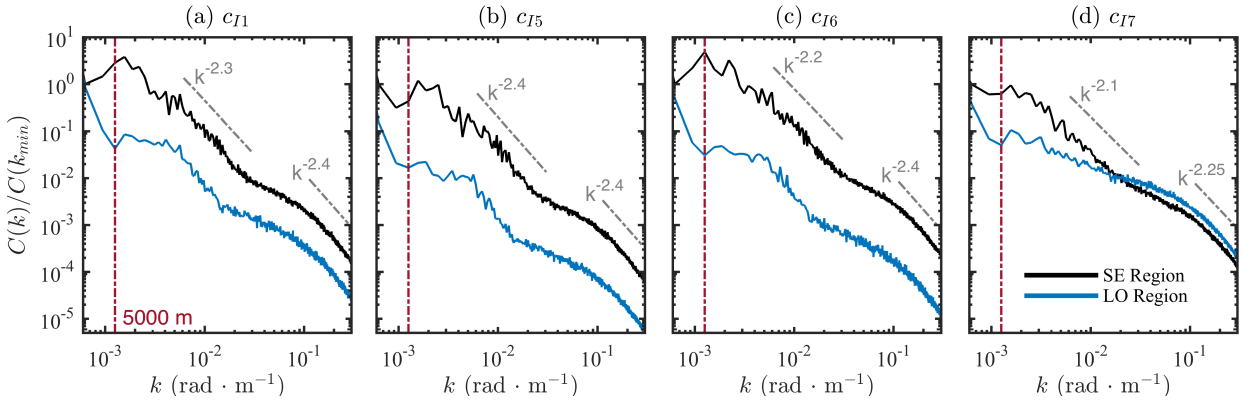

2.3.3 Multiscale Vertical Transport

As was done previously in [4], two-dimensional (2D) spectral decompositions are performed here with a wavenumber cutoff at $k_c = 2\pi/400$m in order to determine the relative contributions of submesoscale and Langmuir-scale motions to vertical fluxes of buoyancy and tracers. The decompositions are calculated using 2D horizontal fast Fourier transforms (FFTs) and 2D circularly-symmetric filtering at each depth. In addition to the usual averaging over all x, separate y subsection averaging is again performed over the SE and LO regions, allowing the relative large- and small-scale contributions to vertical transport to be examined within each of these two distinctly different flow regions. Low-pass-filtered fields, which contain all wavenumbers less than or equal to k_c, are assumed to be associated with 2D submesoscale eddies. High-pass-filtered fields, which contain all wavenumbers greater than k_c, are assumed to be associated with 3D boundary layer (or Langmuir) turbulence.

Figure 2.11 shows depth profiles of the total, low-pass, and high-pass vertical velocity magnitude $\langle w'w' \rangle_{xy_*}$, buoyancy flux $\langle w'b' \rangle_{xy_*}$, and passive tracer flux $\langle w'c' \rangle_{xy_*}$ for both the SE and LO regions. The scale decomposition in the LO region indicates that all vertical

Figure 2.11: Multiscale vertical fluxes (a) $\langle w'w' \rangle_{xy_*}$, (b) $\langle w'b' \rangle_{xy_*}$, (c) $\langle w'c'_{H1} \rangle_{xy_*}$, (d) $\langle w'c'_{I1} \rangle_{xy_*}$, (e) $\langle w'c'_{I5} \rangle_{xy_*}$, and (f) $\langle w'c'_{I7} \rangle_{xy_*}$ approximately 8 hours after the start of the simulations. Solid lines show results in the SE region and dashed lines show results in the LO region.

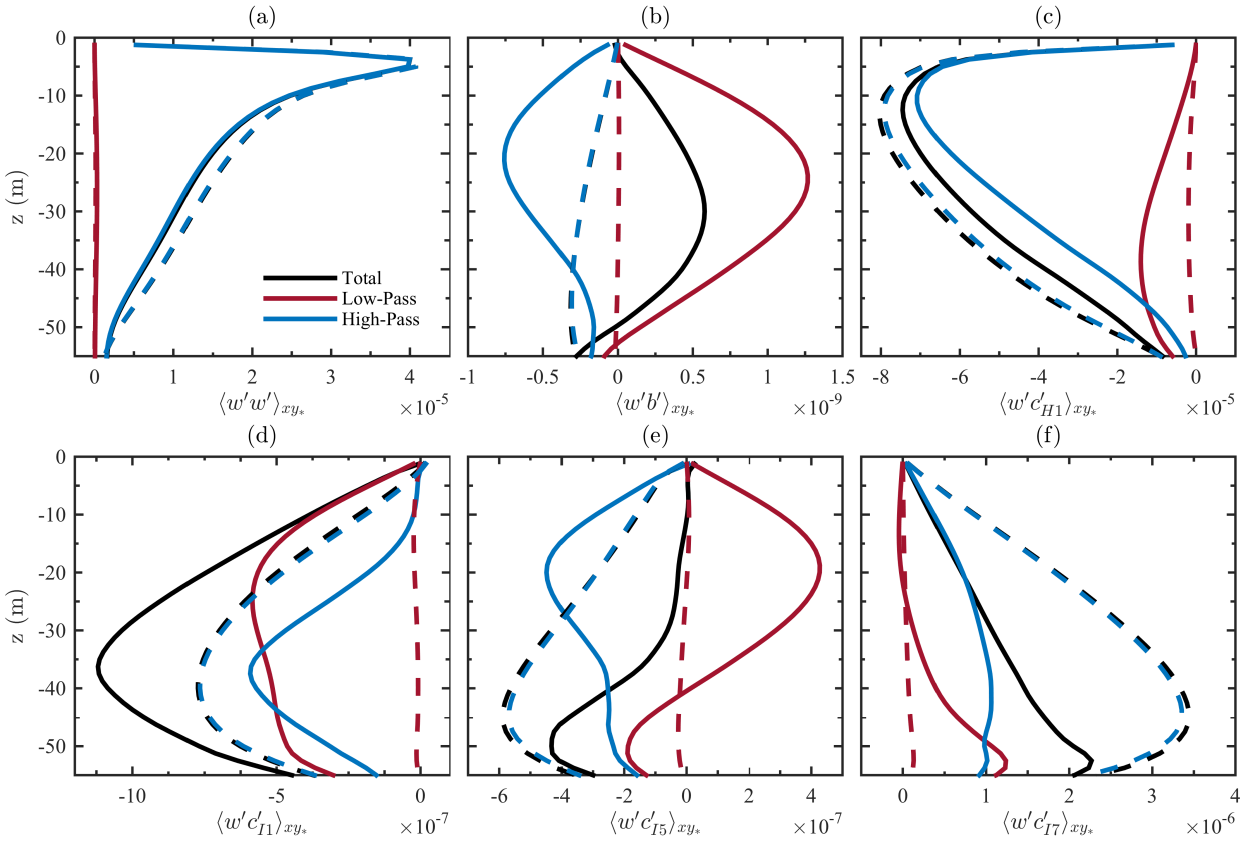

flux, regardless of quantity being transported, is almost entirely due to small, Langmuir-scale fluxes, with essentially no contribution coming from large scales. However, in the SE region, the scale decomposition reveals a much richer story. As was discussed in [4] and as can be seen in Fig. 2.11(a), most of the total vertical velocity in the SE region is associated with small-scale motions for all depths and is primarily confined to the upper surface layers, stemming from 3D boundary layer turbulence. Vertical flux of the active buoyancy tracer was also discussed in [4], where it was found that, in contrast to the vertical velocity, the total vertical buoyancy flux exhibits substantial amplitudes all of the way down to the mixed layer base in the SE region and remains largely positive, indicating a net restratifying effect

on the mixed layer. As shown in Fig. 2.11(b) and [4], however, the scale decomposition reveals that the positive net transport of buoyancy is actually comprised of two opposing larger magnitude fluxes, a positive (upwelling) large-scale flux that extends deeper into the mixed layer and attempts to restratify and restore buoyancy stability by carrying warm, less dense deep waters toward the surface and a negative (downwelling) small-scale flux that attempts to homogenize the mixed layer by transporting and mixing warmer surface waters down to greater depths. Due to the active nature of the buoyancy tracer, all of this transport corresponds to changes in the potential energy of the system. Therefore it may be sufficient, for parameterization purposes, to represent only the submesoscale restratification of buoyancy [1] and not the submesoscale transport of passive tracers [e.g., by the scalings in 82]. In this study, most effects of submesoscale eddies on passive tracers come through the suppression of turbulent mixing by increased stratification (although it may be challenging to arrive at the appropriate averaged suppression rate if submesoscale features are not resolved).

The additional coupling of passive tracers into the present analysis reveals a vastly different story than that for the active buoyancy tracer. Vertical flux of the air-sea flux tracer c_{H1} is shown in Fig. 2.11(c) and other than small differences in magnitude, vertical fluxes for all air-sea flux tracers exhibit the same behavior as c_{H1}. For these tracers, the majority of the vertical flux is due to small-scale motions, which are greatest within the surface convective layer and taper off at greater depths. The resulting transport acts to pull higher surface concentrations down to greater depths, in a consistent down-gradient direction.

The story is once again somewhat different for the passive initial source tracers. Figures 2.11(d)-(f) show vertical fluxes for the surface-released tracer, c_{I1}, the deep mixed layer released tracer, c_{I5}, and the tracer released below the initial pycnocline, c_{I7}. While each of these tracers appear to exhibit vastly different vertical profiles, a few consistent trends do appear. As with all of the other tracers in Fig. 2.11, vertical flux in the LO region is due primarily to small-scale motions, with negligible contributions from large scales. Addition-

ally, for all c_{Ij} tracers in the SE region below the convective layer ($z \lesssim -40$m), both large and small-scales fluxes are significant and similar in magnitude. By contrast, within the convective layer ($z \gtrsim -30$m), the similarity between the different c_{Ij} tracers vanishes and a dependency on tracer release depth emerges. For the surface-released tracer in the SE region shown in Fig. 2.11(d), both large- and small-scale motions work together to transport high surface concentrations to greater depths. For tracer c_{I5} released deep in the mixed layer, however, Fig. 2.11(e) indicates a balance between competing upwelling large-scale and downwelling small-scale motions, such that the net vertical flux for $z \gtrsim -30$m is close to zero. Lastly, for tracer c_{I7} released below the initial pycnocline, Fig. 2.11(f) shows that small-scale motions dominate large-scale motions in the mixed layer. These results all serve to show that multiscale vertical fluxes of tracers released at different depths and within different flow regions are often substantially different from each other and, contrary to suggestions in previous studies (e.g., [83]) that do not take into account the effects of vertical mixing by small-scale Langmuir turbulence, cannot be explained using the same vertical flux profile as for the active buoyancy tracer.

2.4 Mixed Layer Eddy Diffusivities

Results in the previous section have revealed that there are substantial differences in tracer properties and distributions depending on the type of tracer (e.g., air-sea flux or initial source), the surface flux rate, the initial source location, and the flow structure of the mixed layer (e.g., LO or SE regions). In the following, the analysis is extended to consider vertical eddy diffusivities for different tracers and different flow regions, with a view towards understanding prediction requirements for models of upper ocean tracer dynamics.

A common practice in both global and regional climate simulations is to relate tracer mixing processes at subgrid scales to known resolved-scale quantities using a subgrid-scale parameterization. The most widely used such parameterization is the gradient diffusion model, which relates turbulent vertical flux of a tracer c_i to the mean vertical gradient of

the tracer's concentration as

$$\langle w' c_i' \rangle = -K_i \frac{\partial \langle c_i \rangle}{\partial z} \,, \tag{2.10}$$

where $\langle \cdot \rangle$ represents an appropriate average (defined as $\langle \cdot \rangle_{xy_*}$ in the following) and the constant of proportionality K_i is termed the vertical turbulent eddy diffusivity. Underlying Eq. (2.10) is the implicit assumption that turbulent mixing is a purely down-gradient diffusive process achieved by local, small-scale, stochastic turbulent motions. This, in turn, implies that K_i should generally be positive, and negative values of K_i typically imply a breakdown of the gradient diffusion model in Eq. (2.10). Negative diffusivities can occur in flows with active tracers, which may require a counter-gradient flux as opposed to the down-gradient flux represented by Eq. (2.10) [84], as well as in flows where submesoscale eddies restratify the mixed layer, since such eddies induce both advective and diffusive eddy transport, which are anisotropic and tracer-distribution-dependent [82, 85]. Effects due to symmetric instabilities are similarly complex [53]. Therefore, although a scalar vertical diffusivity as in Eq. (2.10) is an oversimplification, it can aid in understanding tracer transport and also mimics common tracer transport parameterization practice.

Eddy diffusivities are estimated here from Eq. (2.10) using the observed values of $\langle w' c_i' \rangle_{xy_*}$ and $\langle c_i \rangle_{xy_*}$ for the air-sea flux tracers in Fig. 2.4 and for the initial source tracers in Fig. 2.9. The resulting eddy diffusivities K_{Hi} for the air-sea flux tracers are shown in Fig. 2.12 for both the LO and SE regions approximately 8 hours after the start of the simulations (results at other times exhibit similar trends). Eddy diffusivities are positive throughout the mixed layer for all tracers and in both the LO and SE regions, indicating that for air-sea flux tracers, the fundamental assumption of down-gradient transport underlying Eq. (2.10) is valid. For all tracers, K_{Hi} is largest near the surface where vertical mixing is strongest and peaks at depths of roughly $z = -13$m in the SE region and $z = -20$m in the LO region. Eddy diffusivities are larger in the LO region than in the SE region, consistent with the dominance of vertical transport by Langmuir turbulence in the LO region and the suppression of this

Figure 2.12: Profiles of vertical eddy diffusivities K_{Hi} approximately 8 hours after the start of the simulations for air-sea flux tracers c_{H1}-c_{H5} in the SE (solid lines) and LO (dashed lines) regions. Lines for tracers c_{H3}-c_{H5} are overlapping.

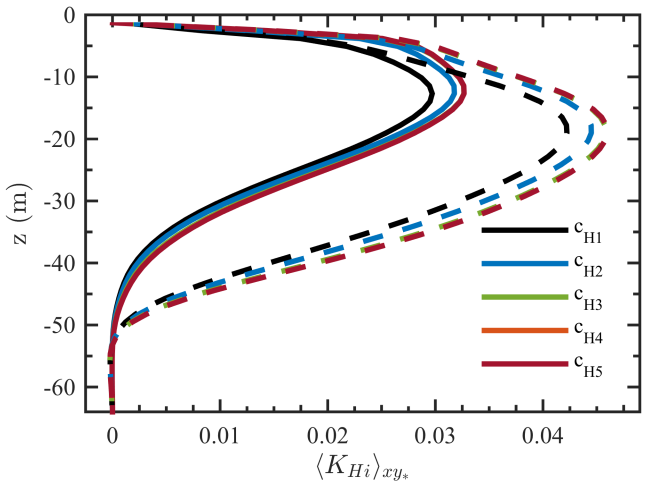

turbulence in the SE region. Although there are vertical jets associated with submesoscale eddies in the SE region, the restratifying effects of these eddies suppress the mixing effects of Langmuir turbulence, resulting in an overall decrease in the amount of vertical mixing seen in this region. Figure 2.12 shows that eddy diffusivities are identical for tracers with surface flux rates much lower than that of the dominant near surface mixing rate (i.e., tracers c_{H3}-c_{H5}). However, for higher flux rates (i.e., tracers c_{H1} and c_{H2}) saturation occurs near the surface, thereby decreasing vertical transport more than the associated decrease in the vertical mean gradient (relative decreases were examined but are not shown here), resulting in slightly smaller, yet persistent, values of the vertical eddy diffusivity.

Figure 2.12 indicates that there are large differences in the vertical eddy diffusivity between the SE and LO regions. Figure 2.13 provides a more refined picture of the spatial variability of K_{Hi} by showing the horizontal $(x-y)$ field of local eddy diffusivity and the vertical $(y-z)$ field of along-front eddy diffusivity for c_{H3}. The local eddy diffusivity is obtained by calculating $\langle w'c_i' \rangle_{xy}$ and $\langle c_i \rangle_{xy}$ over 1km^2 horizontal regions at each value of x and y. The along-front eddy diffusivity is obtained by calculating the x-averages $\langle w'c_i' \rangle_x$ and

Figure 2.13: Field of the vertical eddy diffusivity K_{I3} in a horizontal $x-y$ plane at z =-25m (top) and in a vertical $y-z$ plane (bottom) for the initial source tracer c_{I3} approximately 8 hours after the start of the simulations. The black contour lines show the depth of the mixed layer based on the buoyancy threshold $\Delta b > (\Delta b)_c$.

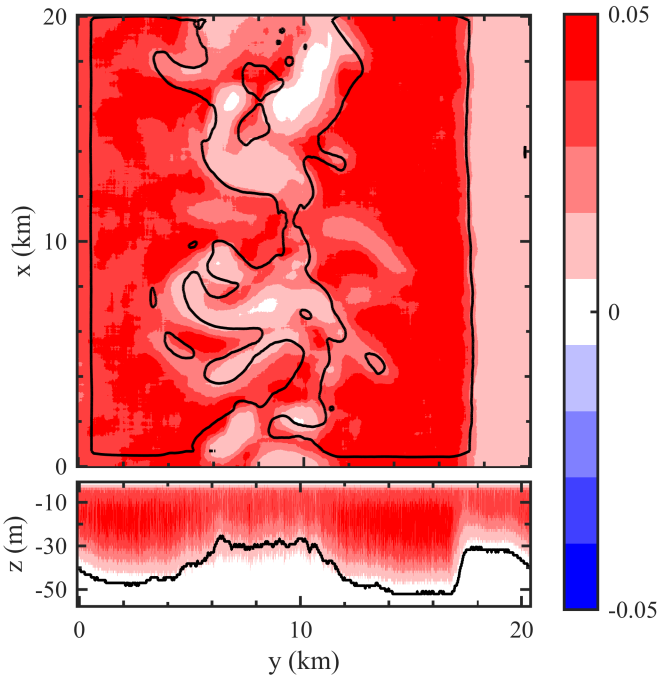

$\langle c_i \rangle_x$ at each value of y and z. Other than small differences in magnitude and vertical extent, vertical eddy diffusivities for all of the air-sea flux tracers exhibit the same spatial structure as that shown in Fig. 2.13 for c_{H3}.

As in Fig. 2.12, Fig. 2.13 shows that the eddy diffusivity field is everywhere positive at a depth of 25m and when averaged across the x direction (this positivity also holds for all other depths in the domain) and thus agrees with the fundamental assumption underlying Eq. (2.10) that turbulent transport is down-gradient. This is to be expected given the nature of the air-sea flux tracer boundary condition, which acts as a source of tracer at the surface. Due to the surface source of air-sea flux tracers, the largest tracer concentrations occur near the surface where small-scale, diffusive-like vertical mixing is dominant and large-scale submesoscale processes that can lead to counter-gradient transport, such as strong upwelling

plumes, are less prevalent [as previously discussed in Section 2.3.3 and shown in Fig. 2.11(c)].

Again consistent with Fig. 2.12, Fig. 2.13 shows that the vertical eddy diffusivity is suppressed in the SE region relative to the LO region. Moreover, Fig. 2.13 shows that regions of suppressed convective mixed layer depth correspond closely to regions of suppressed vertical eddy diffusivity. Mixed layer depth is determined here (see also [4]) as the value of z where the quantity $\langle \Delta b \rangle_{xy}/(\Delta b)_c$ (for the $x-y$ field) or $\langle \Delta b \rangle_x/(\Delta b)_c$ (for the $y-z$ field) is approximately one, where $(\Delta b)_c$ = -0.53 m s^{-2} and the average $\langle \cdot \rangle_{xy}$ is again over 1km^2 horizontal subregions. Reduced vertical eddy diffusivity is thus closely associated with a shallower mixed layer in the SE region; both effects are fundamentally due to restratification of the mixed layer by submesoscale eddies. Both the stable and unstable fronts have shoaled the mixed layer, the former by Ekman buoyancy fluxes and the latter by submesoscale eddy restratification.

It is somewhat more difficult to calculate vertical eddy diffusivities for the initial source tracers c_{I1}-c_{I7} since the vertical gradients of $\langle c_{Ij} \rangle$ are close to zero over nearly the entire mixed layer, as shown in Figs. 2.9(a) and (d). As a result, it is difficult to obtain meaningful profiles of vertical eddy diffusivities similar to Fig. 2.12 and, consequently, only spatial maps of vertical eddy diffusivity are calculated for the initial source tracers. The resulting Fig. 2.14 shows that vertical eddy diffusivities of the initial source tracers are vastly different from one another, both in the horizontal $x-y$ fields and the x-averaged $y-z$ fields. These differences could be due to actual differences in eddy diffusivity or due to the different velocity fields encountered by different tracers depending on where they were released. Additionally, tracers c_{I1} and c_{I6} exhibit large regions of negative eddy diffusivity, particularly in the SE region, which contradicts the fundamental assumption underlying the down-gradient diffusion model in Eq. (2.10). As with the air-sea flux tracers, Fig. 2.14 shows that a suppressed convective mixed layer depth corresponds to a suppression of vertical eddy diffusivity, but this does not predict the location of the negative K_{Ij}.

Further insights into the appearance of negative eddy diffusivities can be obtained by

Figure 2.14: Same as Fig. 2.13 but for tracers (a) c_{I1}, (b) c_{I6}, and (c) c_{I7}. Panel (d) shows the Ertel potential vorticity q defined in Eq. (2.11).

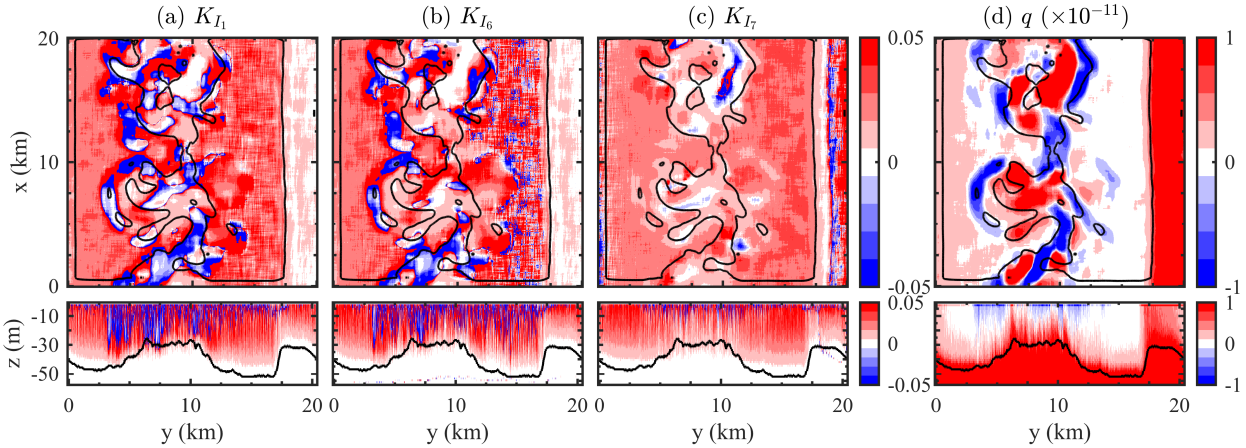

considering that wind-driven frontogenesis and symmetric instabilities associated with submesoscale eddies may serve as pathways for counter-gradient diffusion through non-stochastic large-scale transport by submesoscale processes, such as upwelling plumes. [86] proposed that in order for a flow to be unstable to symmetric instabilities, the Ertel potential vorticity, defined as

$$q = \boldsymbol{\omega}_a \cdot \nabla b \,, \tag{2.11}$$

must be negative, where $\boldsymbol{\omega}_a = \nabla \times \mathbf{u} + \mathbf{f}$ is the absolute vorticity. [53] have furthered this connection to cases that include an applied Stokes drift, as in the present study.

Figure 2.14(d) shows $x-y$ slices and x-averaged $y-z$ plots of potential vorticity, q. Initial qualitative inspection of the corresponding K_{Ij} and q fields suggests co-location of negative vertical eddy diffusivity and negative potential vorticity. This connection is made more quantitative in Fig. 2.15, which shows the pointwise mutual information (PMI) function [87–90] for vertical eddy diffusivity and potential vorticity at a depth of $z = -25$m for tracers c_{I1}, c_{I6}, and c_{I7}. Here the PMI function, denoted $I(q, K_{Ij})$, is defined as

$$I(q, K_{Ij}) = \log_{10}\left[\frac{P(q, K_{Ij})}{P(q)P(K_{Ij})}\right] , \tag{2.12}$$

where $P(q)$ and $P(K_{Ij})$ are marginal probability density functions and $P(q, K_{Ij})$ is a joint

Figure 2.15: Pointwise mutual independence function $I(q, K_{Ij})$ from Eq. (2.12) for tracers (a) c_{I1}, (b) c_{I6}, and (c) c_{I7} at a depth of $z = -25$m approximately 8 hours after the start of the simulations. Black contour lines correspond to $I(q, K_{Ij}) = 0$ where K_{Ij} and q are independent.

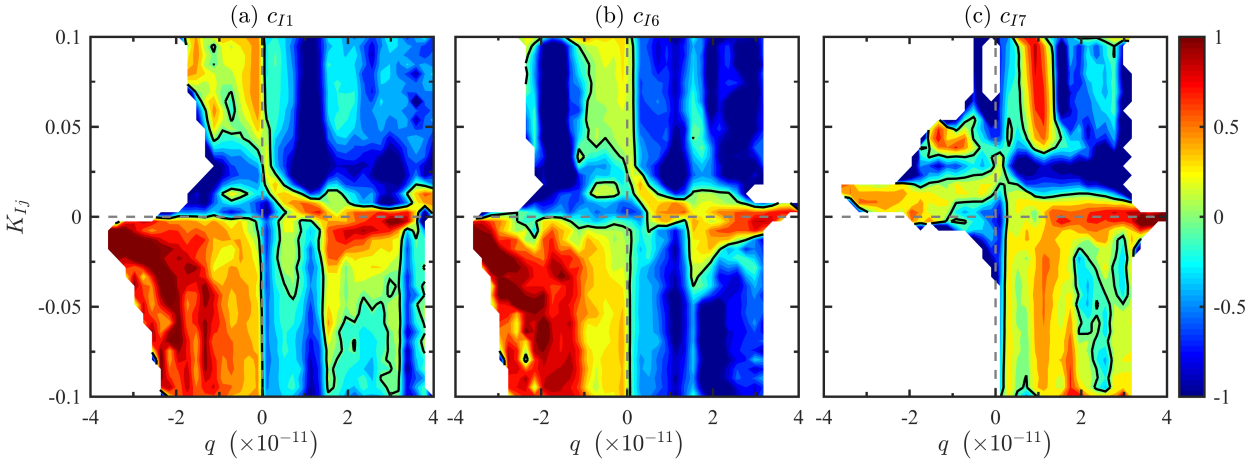

probability density function. Positive values of $I(q, K_{Ij})$ indicate a correlation between q and K_{Ij} while negative values indicate an anti-correlation. When $I(q, K_{Ij})$ is zero then q and K_{Ij} are independent.

Figure 2.15 shows that for c_{I1} and c_{I6}, there are large positive values of $I(q, K_{Ij})$ for negative eddy diffusivity and negative potential vorticity. This indicates that negative eddy diffusivity is correlated with negative potential vorticity, which means in turn that if the flow is unstable to symmetric instabilities, negative eddy diffusivities are likely to occur in the same region. It is intriguing that tracers initialized near the surface and those initialized near the mixed layer base both exhibit this behavior. Negative potential vorticity is sometimes expected from wind-front interactions [91], and these regions are frontal and oriented in roughly the down-wind direction. The potential vorticity criterion is a necessary, but not sufficient, condition for the presence of symmetric instabilities and is unchanged even in the presence of Stokes forces [53]. However, turbulent transport by symmetric instabilities is significantly affected by the presence of Stokes forces, and may contain considerable cross-isopycnal fluxes [53]. It should also be noted that negative potential vorticity and possibly

also symmetric instabilities are not a guarantee of counter-gradient diffusion, as is evident from the air-sea flux tracer results where no negative eddy diffusivities are observed. It is more likely that the vertical diffusivity is a poor diagnosis of tracer transport by symmetric instability, which is typically oriented largely along isopycnals rather than vertically [63], but in the presence of Stokes drift has larger cross-isopycnals directionality [53].

The correlation between negative K_{Ij} and negative q is only present during the initial phase of the tracer field evolution. Once the tracer has fully mixed throughout the mixed layer, the correlation between negative K_{Ij} and negative q fades. Closer examination of K_{Ij} at late times reveals that the vertical flux of the tracer $\langle w' c'_{Ij} \rangle$ becomes decoupled from the mean vertical gradient $\partial \langle c_{Ij} \rangle / \partial z$. The vertical gradient does, however, remain strongly correlated with q at all times. During the development phase, it can thus be hypothesized that gradients are strong and dictate the direction of tracer transport, leading to a strong correlation between negative K_{Ij} and q. As the tracers become well mixed throughout the mixed layer, both concentration gradients and fluxes become weaker and the coupling between K_{Ij} and q is lost.

2.5 Pseudo-Production of Phytoplankton

The initial source tracers c_{I1} and c_{I7} have been chosen in this study as a result of their relevance to phytoplankton production. The surface tracer c_{I1} has a release location similar to that where phytoplankton grow (i.e., near the surface due to light penetration) and tracer c_{I7}, which is initialized at $z = -60$m, is similar to nutrients that are stored at depth and that the phytoplankton require in order to grow. It is textitasized that the idealized tracers examined in this study are not intended to be direct approximations of realistic biologically-reactive tracers such as phytoplankton and nutrients. Rather, these tracers have been chosen to yield fundamental insights into fluid processes relevant to realistic tracer evolution, in the absence of potentially confounding effects due to biological reactivity.

A key characteristic of phytoplankton and nutrients is that they are both essentially

passive in the water column and rely largely on physical ocean mixing processes to bring them together. In the presence of both submesoscale eddies and Langmuir turbulence, however, it is not immediately clear exactly which processes are most effective at bringing these two tracers together. Submesoscale eddies ultimately act to restratify and decrease the depth of the mixed layer, but in the process can induce compact and intense upwelling that has been shown to increase nutrient vertical transport to the surface [6, 36, 45, 55–57, 63, 83, 91–95]. By contrast, Langmuir turbulence deepens the convective mixed layer, helping to bridge the gap between tracers stored at depth and surface-confined tracers. Within the SE region in the present study however, Langmuir suppression is the dominant effect of submesoscale activity.

Insights into how nutrients and phytoplankton are brought together in the mixed layer can be obtained by taking the product of the concentrations for c_{I1} and c_{I7}. Regions where this product is high would correspond to a higher rate of consumption of the tracer stored at depth and subsequent surface tracer growth. This product is used here as a surrogate for realistic biological production and is thus termed "pseudo-production" in the following.

Figure 2.16 shows a 3D volume of the tracer product $c_{I1} \cdot c_{I7}$ approximately 8 hours after the tracers are introduced to the simulations. Upon initial examination, the overall spatial structure of the product field resembles that of the c_{I7} concentration field [see Fig. 2.8(d)]. This occurs since c_{I1} is nearly uniformly distributed throughout the mixed layer, and thus differences in the product are due almost completely to the distribution of the tracer stored at depth. This indicates that turbulent mixing processes that are able to pull up deeply-stored tracers on relatively short time scales are most likely to promote accelerated surface tracer growth.

Notably, Fig. 2.16 shows that there is less pseudo-production within the SE region as compared to the LO region. The ability of Langmuir turbulence to deepen the convective mixed layer and access tracers stored at great depths promotes increased contact between a surface-released tracer and one that is stored at depth. Within the SE region, Langmuir

Figure 2.16: Instantaneous 3D snapshot of the pseudo-production, defined as the product $c_{I1} \cdot c_{I7}$, where tracer c_{I1} has an initial source at the surface and c_{I7} has an initial source at $z = -60$m. Results are shown approximately 8 hours after the start of the simulations and the color scale is logarithmic.

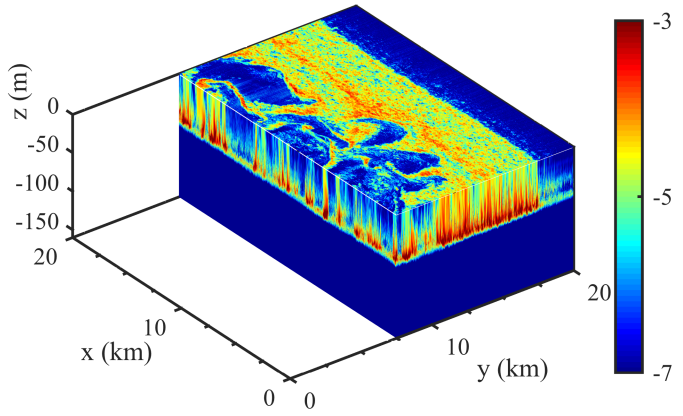

turbulence is weakened and restratification effects are strengthened, causing the mixed layer depth to become shallower and thus limit access of the faster convective layer to the tracer stored at depth. As a result, strong vertical upwelling plumes associated with submesoscale eddies serve as the primary mode of contact between the two tracers within this region. While these upwelling jets can contain more intense pseudo-production, their occurrence is intermittent and their effects are sparse in comparison to the well-mixed LO region, leading to an overall smaller average pseudo-production within the SE region. This is shown quantitatively in the vertical profiles of pseudo-production in Fig. 2.17, where the production within the mixed layer is larger in the LO region as compared to the SE region.

Figures 2.16 and 2.17 provide preliminary insights into processes that have the greatest potential to promote phytoplankton growth. While Langmuir turbulence in the LO region may provide greater contact between tracers at the surface and at depth, it simultaneously increases the mixed layer depth and thus the maximum depth to which surface tracers can be transported. In the context of real-world phytoplankton production, this could result in the reduction of phytoplankton residence time above the "Sverdrup depth," the critical depth at which photosynthesis is no longer nutrient-limited, but rather light limited [96]. In contrast,

Figure 2.17: Vertical profiles of the $x-y$ averaged pseudo-production, defined as the product $c_{I1} \cdot c_{I7}$, where tracer c_{I1} has an initial source at the surface and c_{I7} has an initial source at $z = -60$m. Profiles are shown approximately 8 hours after the start of the simulations for the SE region (solid line) and the LO region (dashed line).

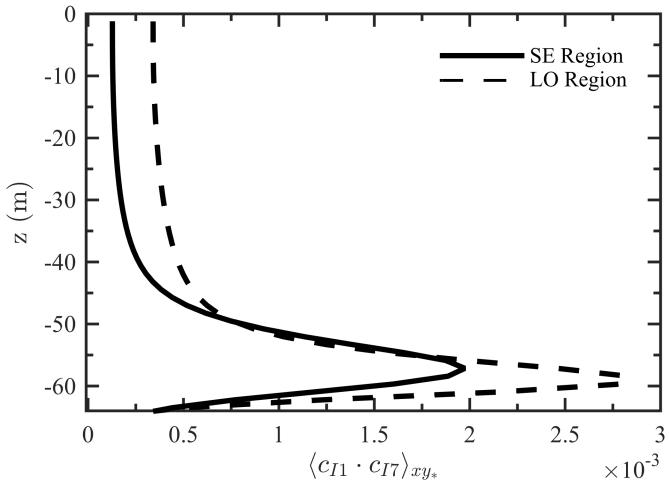

the SE region experiences a shoaling of the mixed layer, confining surface tracers to shallower depths. Again in the context of real-world phytoplankton production, submesoscale eddies may thus increase the likelihood of phytoplankton remaining above the Sverdrup depth, but may also limit contact between phytoplankton and nutrients due to reduced vertical mixing (with the exception of transport by intermittent and sparse submesoscale plumes).

It should be noted that the present study of idealized tracers provides only preliminary insights into phytoplankton production. In order to further understand real-world scenarios, a more complete study that accounts for light availability and many other highly-variable factors are necessary to understand the limits on growth in realistic scenarios [97].

2.6 Conclusions

In this chapter, a fundamental approach has been taken in order to examine the coupled effects of two different oceanic turbulent mixing processes, namely submesoscale eddies and small-scale Langmuir turbulence, on the spatial and temporal evolution of passive tracer

distributions. Results indicate that the rate of air-sea tracer flux into the domain, the initial location of a tracer source, and the flow regime all have profound effects on tracer evolution.

Examination of two different flow regions, the combined submesoscale eddy and Langmuir turbulence (SE) region and the Langmuir dominated (LO) region, reveal a substantial dependence of tracer properties on the relative strengths of restratifcation by submesoscale eddies and vertical mixing by Langmuir turbulence. The fast mixing enabled by small-scale Langmuir turbulence deepens the reach of the convective mixed layer, bringing more surface tracer concentration down and at-depth tracer concentration up, while the larger-scale, restratifying effects of submesoscale eddies suppress vertical mixing, except for a few strong, intermittent, and localized upwelling plumes. This dependency on flow regime is further shown to have an effect on the horizontally-averaged tracer vertical eddy diffusivity.

Vertical mixing of air-sea tracers depends on the ratio of characteristic timescales associated with the tracer flux rate into the domain and near-surface mixing processes, with three different regimes evident, depending on the value of this ratio. Analysis of different air-sea tracer flux rates reveals that vertical mixing is largely independent of tracer flux rate until this ratio becomes $\mathcal{O}(1)$. At this point, the tracer saturates near-surface layers and inhibits air-sea flux of the tracer into the domain. However, entrainment of deeper water can continue to maintain surface fluxes. Outside of this characteristic timescale matching, near-surface mixing processes are sufficiently fast to flush out the surface layer, permitting an uninhibited flux of the tracer into the domain. Air-sea fluxes with lower flux rates reveal significant effects of submesoscale features.

Tracers with different initial release depths exhibit vastly different distributions depending on their proximity to the mixed layer depth. It has been found that the evolution of tracers released at depths well within the fast convective mixed layer is largely independent of the tracer initial release location. By contrast, tracers released at depths near or below the convective mixed layer boundary exhibit vastly different spatial and temporal distributions that are heavily dependent on the initial release location as well as the shape of the bottom

of the convective mixed layer.

A multiscale analysis of tracer vertical transport reveals substantial differences between vertical fluxes of different tracers, particularly in the SE region. In the LO region, essentially all of the vertical transport is performed by small-scale motions for all tracers, but in the SE region, both large- and small-scale motions can play significant roles in tracer transport. This is particularly true for the initial source tracers, while the air-sea flux tracers are dominantly transported away from the surface by small-scale motions in both the SE and LO regions. Perhaps most importantly, comparisons with multiscale fluxes of buoyancy indicate that vertical fluxes of passive tracers are typically much different than vertical fluxes of buoyancy, an active tracer.

For tracers released at different initial depths, instances of negative vertical eddy diffusivity are observed, potentially corresponding to counter-gradient diffusion or transport by more complex structures than simply small-scale turbulent vertical mixing. Moreover, negative values of the eddy diffusivity are found to be preferentially co-located with negative potential vorticity. A mechanism resembling Stokes-influenced symmetric instability, which is indicated by the presence of negative potential vorticity [53, 86], may be the cause of the apparently negative eddy diffusivities, or it may be an advective aspect of frontogenesis not yet adequately understood in this context. For the initial development phase of the tracer, the correlation between negative eddy diffusivities and negative potential vorticity is strong. However, once the tracer is sufficiently mixed throughout the mixed layer, this correlation fades. During the initial development, eddy diffusivities and vertical fluxes are dictated by mean vertical gradients, with which the potential vorticity remains strongly coupled. As these gradients weaken and spread, however, eddy diffusivities and vertical fluxes are no longer strongly dictated by the gradient, leading to a decoupling with potential vorticity. These results are suggestive of counter-gradient diffusion occurring at certain times and locations in the present spin-down simulations, and the connection with negative potential vorticity deserves further study in the future.

Both tracer dependency on release depth and flow regime have been shown to have important consequences on productive contact between tracers that reside at the surface, such as phytoplankton, and those that are stored at depth, such as nutrients. The present results show that the tracer at depth is the limiting factor in a simple product and that the increased vertical transport occurring in the LO region promotes an overall greater average tracer product. However, determining whether this region would be more advantageous for a phytoplankton bloom relies on factoring in the averaged seasonal mixed layer depth, average seasonal light penetration depth, as well as the reactive time scale of the phytoplankton.

Ultimately, the present study has substantial consequences for reduced-order modeling of tracer dynamics and indicates that any physically-accurate passive tracer mixing parameterization should take into account dependancies related to the vertical structure of the mixed layer, the dominant flow regime (e.g., combined submesoscale-Langmuir dynamics or Langmuir-dominated dynamics), as well as the interaction between small-scale turbulent mixing and submesoscale eddies. Although many of these insights are likely to be independent of the spin-down configuration used here to generate submesoscale eddies, it is cautioned that the simulation performed in the present study represents only one particular physical configuration of the ocean (i.e., the stratification, wind strength, wave properties, etc.) and were of a limited time period. Therefore, the findings outlined here are not necessarily universal or representative of all circumstances. Future work for different physical configurations, longer temporal durations, and more realistic ocean conditions is required in order to determine the universality of the results presented herein.

Chapter 3

Small-Scale Turbulence with Reactive Tracers: Effects of Langmuir Turbulence on Upper Ocean Carbonate Chemistry

The previous chapter examined the effects of multiscale upper ocean turbulence on idealized, non-reactive tracers. Although this study revealed many fundamental interactions, inherent time scale interactions between biological and chemical tracers and submesoscale and small-scale processes were left unexamined. The final chapters of this dissertation explore these interactions. In this chapter, results from LES of carbonate chemical species in the presence of realistic mixed layer ocean turbulence are presented. The simulations explore the effects of wave-driven Langmuir turbulence by solving the wave-averaged Boussinesq equations with an imposed Stokes drift velocity. By varying the strength of the Langmuir turbulence, a relationship between the degree of enhancement (or reduction) of carbon that is fluxed across the air-sea interface and the strength of the Langmuir turbulence can be determined.

3.1 Introduction

This study explores the effects of upper ocean turbulent mixing processes on air-sea transfer and hydration of CO_2. We hypothesize that characteristics of upper ocean turbulent processes will affect the amount of CO_2 brought across the air-sea interface, and also influence the depth at which hydration occurs. Prior research on reacting flows has shown that the most significant couplings between reactive tracer evolution and flow physics occur when

flow mixing processes have timescales that rival reaction time scales. Langmuir turbulence, a surface-confined, three-dimensional, small-scale ocean process, has length and time scales on the order of $\mathcal{O}$(1-100 m) and $\mathcal{O}$(1-10 min), respectively. Once CO_2 transfers across the air-sea interface it reacts with seawater, or hydrates, to produce bicarbonate (HCO_3^-) and carbonate (CO_3^{2-}) in a series of reactions whose overall equilibrium time scale is approximately 10-25 s. Due to the similarity in their time scales, neither process can be assumed to be in steady-state and it is therefore necessary to solve the coupled time dependent equations for both the fluid dynamics and chemistry. Larger turbulent processes, such as those associated with submesoscale eddies or mesoscale features, are not examined here as they have much longer time scales $\mathcal{O}(\geq$ 1day) and, as such, are not likely to have strong interactions with carbonate chemical reaction rates. In effect, larger-scale processes are assumed to only set background conditions for small scale processes. Additionally, most biological reactions have time scales much longer than the characteristic time scale of Langmuir circulations and so significant direct tracer-flow couplings are not likely to occur, although indirect effects such as mixed layer deepening may be important.

Previous research has been performed concerning the effects of Langmuir turbulence on biological and chemical tracers. For example, studies have shown that Langmuir turbulence can give rise to tracer patchiness through the aggregation debris, plankton, nutrients, or oil within the convergence zones of its counter rotating cells [25, 98–105], as well as increase the vertical extent of tracers in the upper ocean due to its enhanced mixing effects [44, 106–116]. The effects of Langmuir circulation on sea-surface chemistry have also been examined [117–121], largely concerning the increase in aggregation of nutrients due to windrows and the precipitation of organic particles due to bubble injection from surface wave breaking. In many of these cases, however, tracer reactions were assumed to be sufficiently fast or slow in comparison to the dominant turbulent process and, as a result, significant tracer-flow couplings were not examined.

Although a few studies have looked at time-dependent carbonate chemistry within

the ocean, primarily chemical enhancement of air-sea flux and uptake of carbon by an individual phytoplankton cell, they have largely assumed that the flow is laminar/quiescent or well mixed by the background small-scale turbulence [122–131]. Many studies have also looked at the enhancement of CO_2 exchange rates across the air-sea interface as a function of wind-driven or grid-generated turbulence, wave breaking, and bubble injection. However, no studies have specifically included a time dependent CO_2 hydration mechanism [126, 132–140]. As a result, currently no study has focused on the potential affects of strong tracer-flow coupling between Langmuir circulations and upper ocean carbonate chemistry by simultaneously considering the time-dependent nature of both processes.

The overall goal of this study is to more accurately answer the question: does small-scale turbulence, and Langmuir turbulence in particular, affect the amount of carbon contained in the ocean? More importantly, what physics need to be taken into account when developing reduced-order parameterizations for the flux of CO_2 across the air-sea interface in ESMs? In this study, large eddy simulations (LES) are used to examine the effects of Langmuir turbulence on the evolution of reactive tracers, similar to those in carbonate chemistry, within the upper ocean from scales of 320 m down to 1 m. Comparisons are made between simulations with time dependent chemistry, equilibrium chemistry, and no chemistry for varying strengths of Langmuir turbulence. Simulations are also performed in the absence of Langmuir turbulence, where small-scale turbulence production is shear-driven only. By varying the strength of the Langmuir turbulence, a relationship between the degree of enhancement (or reduction) of carbon that is fluxed across the air-sea interface and the strength of the Langmuir turbulence can be determined.

In the following, the numerical simulations are outlined in Section 3.2, the carbonate chemistry model is described in Section 3.3, results and discussion are provided in Section 3.4, and finally conclusions are outlined in Section 3.5.

3.2 Numerical Simulations

The numerical model used for this study is the same NCAR LES model as used the previous chapter, with the same governing equations, Stokes drift forcing, and sub-grid scale model. All simulations are initialized with a mixed layer depth of $H_{ML,0} = -30$ m, with uniform stratification beneath this depth. Previous studies have shown that Langmuir turbulence exhibits a deepening effect on the mixed layer [4, 141], which is also observed in these simulations. The physical domain size of the simulations is 320m×320m×-96 m, with a computational grid of size 128^3, giving a horizontal resolution of 2.5 m and a vertical resolution of 0.75 m (a summary of these and other simulation parameters is provided in Table 3.1). Initially, the velocity field $\mathbf{u}$ is set to zero everywhere, periodic boundary conditions are used in horizontal $(x - y)$ directions, and a zero vertical velocity condition is applied at the bottom boundary. Boundary conditions for the top boundary for each simulation vary depending on the case. At the start of the simulations, a surface wind stress corresponding to a wind speed of approximately 5.75 m/s aligned with the x-axis is applied to the top boundary. For those simulations with Langmuir turbulence present, the strength of the Langmuir mixing is modified through the Stokes drift velocity, leaving the wind stress the same for all simulations.

Table 3.1: Summary of physical and computational parameters used in the numerical simulations.

Physical size, $L_x \times L_y \times L_z$	320m×320m×-96m
Grid size, $N_x \times N_y \times N_z$	128×128×128
Grid Resolution, $\triangle_x \times \triangle_y \times \triangle_z$	2.5m×2.5m×0.75m
Reference density, ρ_0	1000 kg/m^3
Coriolis parameter, $\mathbf{f}$	$0.729\times10^{-4}\text{s}^{-1}\hat{\mathbf{z}}$
Initial mixed layer depth, $H_{ML,0}$	-30m
Wind speed at 10m, U_{10}	5.75 m/s
Stokes drift direction, ϑ_s	0°
Wind friction velocity, u_τ	5.3×10^{-3} m/s
Wind shear, τ	0.025 N/m^2
Wind direction, ϑ_w	0°

Figure 3.1: Stokes drift velocity $u_s(z)$ used in Eq. 2.5 as a function of depth z for each of the Langmuir cases ($La = 0.4$: red, $La = 0.3$: blue, $La = 0.2$: green). The main plot shows $u_s(z)$ on linear axes and the inset shows $u_s(z)$ on semilog axes.

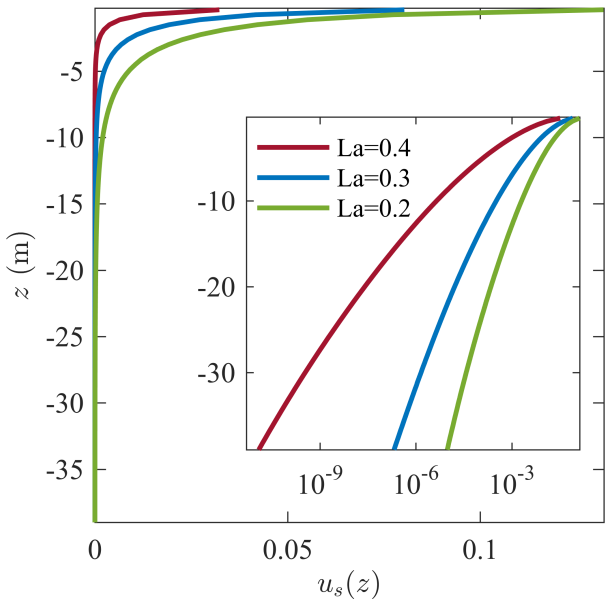

Table 3.2: Summary of Langmuir parameters used in each of the simulations. $La_t^2 = u_*/u_s(0)$, where u_* is the surface friction velocity and $u_s(0)$ is the Stokes drift velocity at the surface.

Label	La	$u_s(0)$ **(m s^{-1})**
NS	∞	0.000
La04	0.40	0.032
La03	0.30	0.080
La02	0.20	0.132

Four physical scenarios are examined: a single case with no Langmuir turbulence (only wind-driven shear turbulence) and three cases with increasing strengths of Langmuir turbulence. The strength of the Langmuir turbulence can be identified by its turbulent Langmuir number, which is defined as the ratio of mixing due to Langmuir turbulence over the mixing due to shear turbulence, $La_t^2 = u_*/u_s(0)$, where u_* is the surface friction velocity and $u_s(0)$ is the Stokes drift velocity at the surface. The turbulent Langmuir numbers for each of the four cases are listed in Table 3.2, where $La = \infty$ corresponds to the shear-only, non-Langmuir, case and $La = 0.20$ corresponds to the strongest Langmuir case. Figure 3.1 shows the vertical profiles of the Stokes drift for each of the three Langmuir cases.

3.3 Carbonate Chemistry Model

The carbonate chemistry model used for this study follows that of the [2] parameterization for carbonate chemical reactions in sea water, which has seven chemical species ($[CO_2]$, $[HCO_3^-]$, $[CO_3^{2-}]$, $[B(OH)_3]$, $[B(OH)_4^-]$, $[H^+]$, and $[OH^-]$), plus water (which is assumed to

have a constant concentration). The system of equations that describe the model are

$$\mathrm{CO_2 + H_2O} \underset{\mathrm{k_{-1}}}{\overset{\mathrm{k_{+1}}}{\rightleftharpoons}} \mathrm{HCO_3^- + H^+} \tag{3.1}$$

$$\mathrm{CO_2 + OH^-} \underset{\mathrm{k_{-4}}}{\overset{\mathrm{k_{+4}}}{\rightleftharpoons}} \mathrm{HCO_3^-} \tag{3.2}$$

$$\mathrm{CO_3^{2-} + H^+} \underset{\mathrm{k_{-5}^{H^+}}}{\overset{\mathrm{k_{+5}^{H^+}}}{\rightleftharpoons}} \mathrm{HCO_3^-} \tag{3.3}$$

$$\mathrm{HCO_3^- + OH^-} \underset{\mathrm{k_{-5}^{OH^-}}}{\overset{\mathrm{k_{+5}^{OH^-}}}{\rightleftharpoons}} \mathrm{CO_3^{2-} + H_2O} \tag{3.4}$$

$$\mathrm{H_2O} \underset{\mathrm{k_{-6}}}{\overset{\mathrm{k_{+6}}}{\rightleftharpoons}} \mathrm{H^+ + OH^-} \tag{3.5}$$

$$\mathrm{B(OH)_3 + OH^-} \underset{\mathrm{k_{-7}}}{\overset{\mathrm{k_{+7}}}{\rightleftharpoons}} \mathrm{B(OH)_4^-} \tag{3.6}$$

$$\mathrm{CO_3^{2-} + B(OH)_3 + H_2O} \underset{\mathrm{k_{-8}}}{\overset{\mathrm{k_{+8}}}{\rightleftharpoons}} \mathrm{B(OH)_4^- + HCO_3^-}\,. \tag{3.7}$$

Table 3.3 provides temperature and salinity dependent equations for each of the coefficients as well as values for the coefficients at $T = 25°\mathrm{C}$ and $S = 35$. It should be noted that this system of rate equations is closed, but is quite stiff and would require a prohibitively small time step to accurately and stably integrate within NCAR LES. To overcome this, two measures were taken. First, the time integration of the advection and chemistry was split [142] such that the advection remained within the native third-order Runge-Kutta (RK) scheme within the NCAR LES model and the chemistry was instead integrated in two half time steps, before and after the advection step, using an explicit second-order Runge-Kutta-Chebyshev (RKC) scheme. The RKC scheme has been shown to be capable of handling moderately stiff chemistry without the need for such a prohibitively small time step [143–145], making it well suited for this application. The second measure was to apply computational singular perturbation (CSP) analysis to the system of carbonate chemical equations, which analyzes the Jacobian matrix to identify any quasi-steady state species or partial equilibrium reactions [146–148]. From this analysis, it was determined that a quasi-steady state assumption for the rate equation of $[\mathrm{H^+}]$ was appropriate due to its relatively small concentration with respect to all other chemical species in the system. This leads to

Table 3.3: Summary of temperature and salinity dependent rate constant equations and values at a temperature of 25°C and salinity of 35 ppt for the carbonate chemistry model. $A_4 = 4.70 \times 10^7$ kg mol^{-1} s^{-1}, $E_4 = 23.2$ kJ mol^{-1}, $A_7 = 4.58 \times 10^{10}$ kg mol^{-1} s^{-1}, $E_7 = 20.8$ kJ mol^{-1}, $A_8 = 3.05 \times 10^{10}$ kg mol^{-1} s^{-1}, and $E_8 = 20.8$ kJ mol^{-1}. The temperature and salinity dependent equilibrium constant equations for K_1^*, K_2^*, K_W^*, and K_B^* are given in [3].

Symbol	**Equation**	**Value**	**Units**
k_{+1}	$\exp(1246.98 - 6.19 \times 10^4/T - 183.0\ln(T))$	0.037	s^{-1}
k_{-1}	$k_{+1}(T)/K_1^*(T,S)$	2.66 $\times 10^4$	kg mol^{-1} s^{-1}
k_{+4}	$A_4 \exp(-E_4/RT)$	4.05 $\times 10^3$	kg mol^{-1} s^{-1}
k_{-4}	$k_{+4}(T) \times K_W^*(T,S)/K_1^*(T,S)$	1.76 $\times 10^{-4}$	s^{-1}
$k_{+5}^{\mathrm{H}^+}$	constant	5.0 $\times 10^{10}$	kg mol^{-1} s^{-1}
$k_{-5}^{\mathrm{H}^+}$	$k_{+5}^{\mathrm{H}^+} \times K_2^*(T,S)$	59.4	s^{-1}
$k_{+5}^{\mathrm{OH}^-}$	constant	6.0 $\times 10^9$	kg mol^{-1} s^{-1}
$k_{-5}^{\mathrm{OH}^-}$	$k_{+5}^{\mathrm{OH}^-} \times K_W^*(T,S)/K_2^*(T,S)$	3.06 $\times 10^5$	s^{-1}
k_{+6}	constant	1.40 $\times 10^{-3}$	kg mol^{-1} s^{-1}
k_{-6}	$k_{+6}/K_W^*(T,S)$	2.31 $\times 10^{10}$	kg mol^{-1} s^{-1}
k_{+7}	$A_7 \exp(-E_7/RT)$	1.04 $\times 10^7$	kg mol^{-1} s^{-1}
k_{-7}	$k_{+7} \times K_W^*(T,S)/K_B^*(T,S)$	249	s^{-1}
k_{+8}	$A_8 \exp(-E_8/RT)$	6.92 $\times 10^6$	kg mol^{-1} s^{-1}
k_{-8}	$k_{+8} \times K_2^*(T,S)/K_B^*(T,S)$	3.26 $\times 10^6$	kg mol^{-1} s^{-1}

the following equation for the concentration of $[\mathrm{H}^+]$

$$[\mathrm{H}^+]_{qss} = \frac{k_{+1}\mathrm{CO}_2 + k_{-5}^{\mathrm{H}^+}\mathrm{HCO}_3^- + k_{+6}}{k_{-1}\mathrm{HCO}_3^- + k_{+5}^{\mathrm{H}^+}\mathrm{CO}_3^{2-} + k_{-6}\mathrm{H}^+}\,. \tag{3.8}$$

In order to determine the error incurred by invoking this assumption, a zero-dimensional test was performed where the system of ODE equations were perturbed by a 10% increase in CO_2 and a 10% decrease in the carbonate concentrations, maintaining zero net change in dissolved organic carbon (DIC), after which all species were allowed to relax back to their respective equilibrium values. Comparing the temporal evolution of the full and reduced sets of equations, less than a 10^{-5}% difference in the concentrations of all species, except for $[\mathrm{H}^+]$, was observed over the entire equilibration time ($\sim$ 60sec). Therefore, the reduced set of equations were determined to be sufficiently accurate for this study.

After applying these two measures, integration of the system of carbonate chemical equations within NCAR LES was reduced to a reasonable computational cost. The resulting reduced set of rate equations are given as

$$\frac{d[\mathrm{CO_2}]}{dt} = (-k_{+1} - k_{+4}[\mathrm{OH^-}])[\mathrm{CO_2}] + (k_{-4} + k_{-1}[\mathrm{H^+}])[\mathrm{HCO_3^-}]\,, \tag{3.9}$$

$$\begin{aligned}\frac{d[\mathrm{HCO_3^-}]}{dt} = {} & (k_{+1} + k_{+4}[\mathrm{OH^-}])[\mathrm{CO_2}] + (k_{-5}^{\mathrm{OH^-}} + k_{+8}[\mathrm{B(OH)_3}] + k_{+5}^{\mathrm{H^+}}[\mathrm{H^+}])[\mathrm{CO_3^{2-}}] \\ & +(-k_{-4} - k_{-5}^{\mathrm{H^+}} - k_{-8}[\mathrm{B(OH)_4^-}] - k_{-1}[\mathrm{H^+}] - k_{+5}^{\mathrm{OH^-}}[\mathrm{OH^-}])[\mathrm{HCO_3^-}]\,, \end{aligned} \tag{3.10}$$

$$\begin{aligned}\frac{d[\mathrm{CO_3^{2-}}]}{dt} = {} & (k_{-5}^{\mathrm{H^+}} + k_{-8}[\mathrm{B(OH)_4^-}] + k_{+5}^{\mathrm{OH^-}}[\mathrm{OH^-}])[\mathrm{HCO_3^-}] \\ & +(-k_{-5}^{\mathrm{OH^-}} - k_{+8}[\mathrm{B(OH)_3}] - k_{+5}^{\mathrm{H^+}}[\mathrm{H^+}])[\mathrm{CO_3^{2-}}]\,, \end{aligned} \tag{3.11}$$

$$\begin{aligned}\frac{d[\mathrm{B(OH)_3}]}{dt} = {} & (k_{-8}[\mathrm{B(OH)_4^-}])[\mathrm{HCO_3^-}] + (-k_{+8}[\mathrm{B(OH)_3}])[\mathrm{CO_3^{2-}}] \\ & +(-k_{+7}[\mathrm{B(OH)_3}][\mathrm{OH^-}] + k_{-7}[\mathrm{B(OH)_4^-}])\,, \end{aligned} \tag{3.12}$$

$$\begin{aligned}\frac{d[\mathrm{B(OH)_4^-}]}{dt} = {} & (-k_{-8}\mathrm{B(OH)_4^-})[\mathrm{HCO_3^-}] + (k_{+8}[\mathrm{B(OH)_3}])[\mathrm{CO_3^{2-}}] \\ & +(k_{+7}[\mathrm{B(OH)_3}][\mathrm{OH^-}] - k_{-7}[\mathrm{B(OH)_4^-}])\,, \end{aligned} \tag{3.13}$$

$$\begin{aligned}\frac{d[\mathrm{OH^-}]}{dt} = {} & (-k_{+4}[\mathrm{OH^-}])[\mathrm{CO_2}] + (k_{-4} - k_{+5}^{\mathrm{OH^-}}[\mathrm{OH^-}])[\mathrm{HCO_3^-}] + (k_{-5}^{\mathrm{OH^-}})[\mathrm{CO_3^{2-}}] \\ & +(k_{+6} - k_{-6}[\mathrm{H^+}][\mathrm{OH^-}] - k_{+7}[\mathrm{B(OH)_3}][\mathrm{OH^-}] + k_{-7}[\mathrm{B(OH)_4^-}])\,, \end{aligned} \tag{3.14}$$

$$[\mathrm{H^+}]_{qss} = \frac{k_{+1}[\mathrm{CO_2}] + k_{-5}^{\mathrm{H^+}}[\mathrm{HCO_3^-}] + k_{+6}}{k_{-1}[\mathrm{HCO_3^-}] + k_{+5}^{\mathrm{H^+}}[\mathrm{CO_3^{2-}}] + k_{-6}[\mathrm{OH^-}]}\,. \tag{3.15}$$

For all cases, all seven chemical species were initialized in the same manner with uniform concentrations throughout the domain, using values given in Table 3.4. Each tracer is subject to periodic boundaries in the horizontal direction and no vertical fluxes at both the bottom and top boundaries. After the turbulence has "spun-up" (approximately 7 virtual days)

and the chemical species have relaxed to their equilibrium values based upon temperature (salinity is constant throughout the domain), which takes an additional 60 virtual seconds, additional CO_2 is introduced into the domain through the top boundary. The CO_2 tracer is allowed to flux across the top boundary according to Henry's law for gas flux across the air-sea interface [79, 80]

$$F_{CO_2} = k_{CO_2}([CO_2]_{air} - [CO_2]_{z=0}), \tag{3.16}$$

where F_{CO_2} is the downward flux rate across the boundary, k_{CO_2} is the tracer flux rate, or piston velocity, $[CO_2]_{air}$ is the concentration in air, or the partial pressure of the species to be dissolved just above the boundary scaled by the Henry's law constant, and $[CO_2]_{z=0}$ is the species concentration just below the boundary. The value of $[CO_2]_{air}$ is fixed at a 10% increase above the initial mixed layer average CO_2 value. The piston velocity, k_{CO_2}, is given as a function of wind speed and Schmidt number, which is a function of temperature and salinity, according to [79]. Simulations were run for an additional 6 virtual hours after the CO_2 tracer is allowed to enter the domain. The simulations were stopped at this point, as 6 hours is the upper limit for which constant forcing could be applied, such as wind speed, Langmuir strengths, radiative heating, etc and remain valid. Simulations run longer than this should take into account variable forcing, such as the diurnal cycle of radiative heating. All results and analysis shown are for this time, unless otherwise stated.

Table 3.4: Summary of tracers. Values given correspond to approximate surface values at a temperature of 25°C, salinity of 35 ppt, alkalinity of 2427.89 μmol kg^{-1}, and DIC of 1992.28 μmol kg^{-1}.

Tracer	**Initial Value**
CO_2	7.56903 μmol kg^{-1}
HCO_3^-	1670.06 μmol kg^{-1}
CO_3^{2-}	314.655 μmol kg^{-1}
H^+	6.30928 $\times 10^{-3}$ μmol kg^{-1}
OH^-	9.60492 μmol kg^{-1}
$B(OH)_3$	296.936 μmol kg^{-1}
$B(OH)_4^-$	118.909 μmol kg^{-1}

Two additional sets of simulations were run: one in which each of the chemical species concentrations was calculated using a system of carbonate chemical equilibrium equations [2] and one in which there were no reactions. The physical scenarios of each these two sets of simulations were identical to the four above, save for the difference in how the chemical reactions were calculated. The first additional set of simulations with equilibrium chemistry mimics how carbonate chemistry is most commonly calculated within ESMs, where reactions are assumed to be instantaneous with respect to the dominant physical processes, and thus represent a system where reaction times are essentially zero. The second additional set of simulations, where no reactions exist, represents a system where reaction times are essentially infinite. The addition of these two sets of simulations thus give upper and lower bounds for ocean carbonate chemistry reaction times. The three different sets of simulations, with differing chemistry calculations, are referred to in the following as the Time-Dependent Chemistry (TC), the Equilibrium Chemistry (EC), and the No Chemistry (NC) simulations, respectively.

3.4 Results

Several metrics are used in the present analysis to examine the effects of Langmuir turbulence on upper ocean carbonate chemistry: (i) horizontal $(x-y)$ and vertical $(y-z)$ fields at the surface and middle of the domain, respectively, (ii) profiles of $x-y$ averaged concentration, vertical turbulent flux, and variance of DIC and CO_2 as a function of depth (z), (iii) change in volume integrated DIC as a function of time, (iv) plots of the percent enhancement of new carbon brought into the domain as a function of time, and (v) plots of $x-y$ averaged air-sea flux rate of CO_2 as a function of time. The following sections will discuss each of these. In order to understand how the strength of Langmuir turbulence affects the flux of CO_2 into the surface layer of the domain, a comparison between just the four different time-dependent chemistry cases is made first. While the overall magnitudes differ for the three chemistry cases, the over all trends are quite similar. Next, a comparison is made

between the results for the shear-only and $La = 0.3$ cases of the three different chemistry models. Lastly, the effects of coupling the varying strengths of Langmuir turbulence and the different chemistry models will be discussed.

Before the carbonate tracers are considered, it is worthwhile to first examine the vertical velocity and temperature fields for each turbulence case in order to understand the physical context in which the reactive tracers evolve. Figure 3.2 shows fields of vertical velocity (w) in a horizontal $x - y$ plane at the surface and in a $y - z$ plane in the middle of the domain for all four turbulence cases ($La = \infty, 0.4, 0.3, 0.2$). Most notably, the vertical velocity, both up- and down-welling, increases as a function of Langmuir turbulence strength, with the weakest vertical velocity within the shear-only, non-Langmuir, case and the strongest in the $La = 0.2$ case. This can be seen most clearly in the $y - z$ planes within the bottom panels, where both the magnitude and vertical reach of the Langmuir cases is much greater than the non-Langmuir case. Additionally, as the Langmuir strength is increased, the coherency of x directional convergent and divergent zones increases, which corresponds to the direction of aligned wind and waves, and gives rise to the recognized windrows of Langmuir turbulence.

Figure 3.3 shows the $x - y$ averaged temperature within the domain as a function of depth for each of the turbulence cases. While all simulations began with the same temperature profile (dashed gray line) and deviate from that initial profile, the Langmuir cases have deviated the most. The increased mixing associated with Langmuir turbulence has deepened the mixed layer depth by approximately 1-3 meters, depending on the case, over the course of the 7 day "spin-up" period. This deepening has not only increased the total volume of the mixed layer, and thereby increasing the short-term new carbon reservoir size, but also decreased the average temperature of the mixed layer by entraining cooler waters from below. While this decrease in temperature may not seem substantial in the larger context, air-sea flux of gases and carbonate chemistry can both be sensitive to temperature. As temperatures cool, CO_2 becomes more soluble in water, allowing for more CO_2 to enter the domain, however, reaction times also decrease, leaving carbon as CO_2 longer before it is

Figure 3.2: Fields of vertical velocity in a horizontal $x-y$ plane at the surface (top panels) and in a vertical $y-z$ plane in the middle of the domain (bottom panels) for the four different strengths of Langmuir turbulence (left to right: (a) $La = \infty$, (b) $La = 0.4$, (c) $La = 0.3$, and (d) $La = 0.2$).

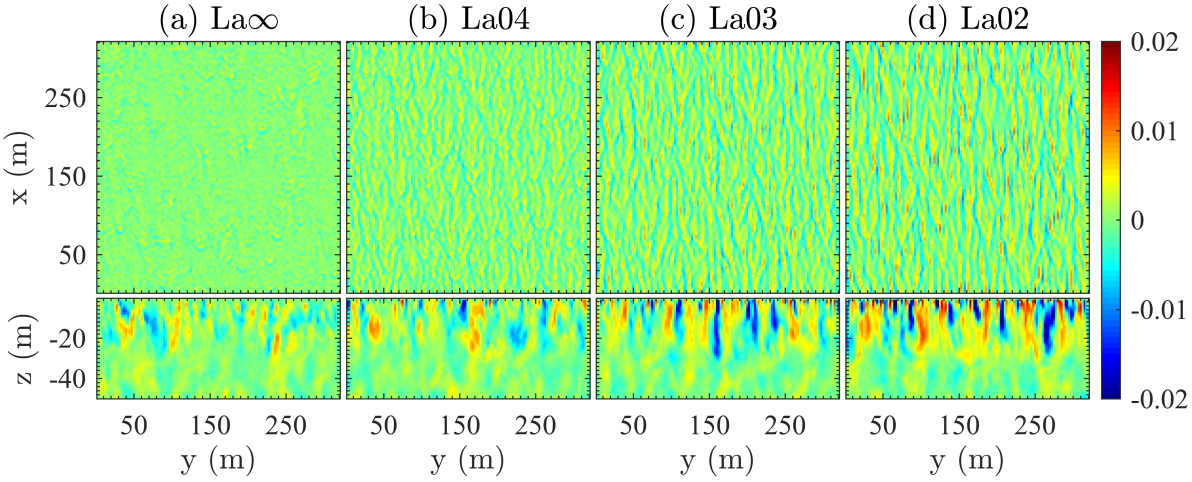

Figure 3.3: $x-y$ averaged temperature within the domain as a function of depth for the four different turbulence cases ($La = \infty$: black, $La = 0.4$: red, $La = 0.3$: blue, $La = 0.2$: green). The dashed gray line shows the initial temperature profile with uniform temperature above $z = -30$m and constant stratification below.

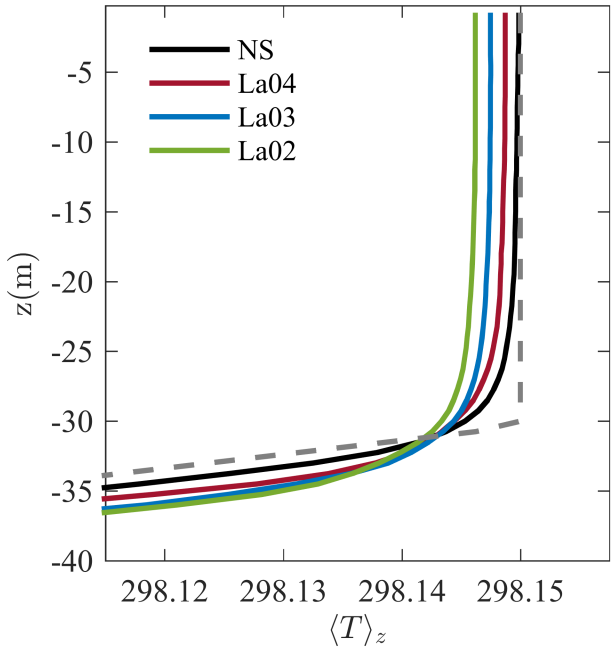

converted into bicarbonate and carbonate. This effect of temperature, i.e. the competition between increased solubility and decreased reaction times, is not directly considered within this study, however, future studies examining these effects within the context of Langmuir turbulence and carbonate chemistry are certainly warranted.

3.4.1 Effects of Langmuir Turbulence

Since there are multiple processes taking place in each of these simulations, it is helpful to first examine a conserved quantity such as DIC, which is the sum of all carbon containing species ($[CO_2], [HCO_3^-]$, and $[CO_3^{2-}]$). Figure 3.4 shows fields of DIC in a horizontal $x-y$ plane at the surface and in a $y-z$ plane in the middle of the domain for all four turbulence cases ($La = \infty, 0.4, 0.3, 0.2$) for the TC chemistry. The vertical distribution and concentration of DIC within the surface of the domain is quite different between the four cases. As the strength of the Langmuir turbulence is increased, additional carbon that has been introduced into the domain through the top surface is progressively brought further down into the mixed layer. This can be seen more clearly in Figure 3.5(a), where the strongest Langmuir cases ($La = 0.2$ and 0.3) have concentrations extending much further down in comparison to the non-Langmuir case. This is partially due to the fast mixing and increased vertical flux associated with Langmuir turbulence, but also the mixed layer deepening effect of Langmuir turbulence.

Figures 3.5(a) and (c) show the $x-y$ averaged concentration and variance for each turbulence case. In the non-Langmuir case, there is a much greater concentration and variance of DIC near the surface and very little near the base of the mixed layer. Conversely, the three Langmuir cases have progressively more uniform concentrations and lower variance throughout the depth of the mixed layer, with the most uniform case having the strongest Langmuir turbulence and the least uniform having the weakest Langmuir turbulence. Again, the more uniform vertical distribution and decreased variance of the three Langmuir cases, in comparison to the non-Langmuir case, can largely be attributed to the faster vertical

Figure 3.4: Fields of DIC in a horizontal $x-y$ plane at the surface (top panels) and in a vertical $y-z$ plane in the middle of the domain (bottom panels) for the four different turbulence cases (left to right: (a) $La=\infty$, (b) $La=0.4$, (c) $La=0.3$, and (d) $La=0.2$) for the time-dependent chemistry case.

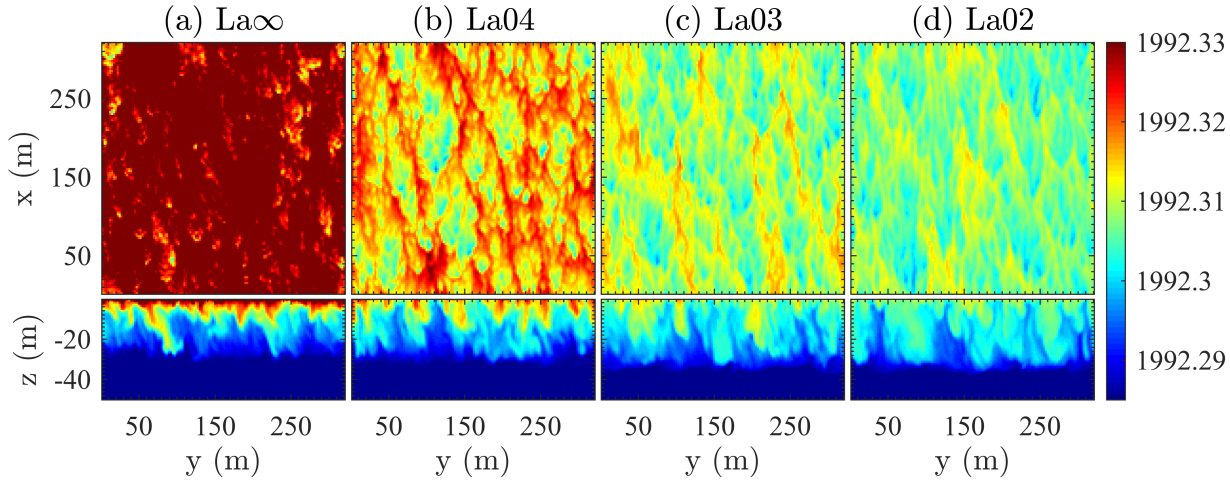

Figure 3.5: $x-y$ averaged (a) concentration, (b) vertical turbulent flux, and (c) variance of DIC within the domain as a function of depth for the four different turbulence cases (left to right: (a) $La=\infty$, (b) $La=0.4$, (c) $La=0.3$, and (d) $La=0.2$) for the time-dependent chemistry case.

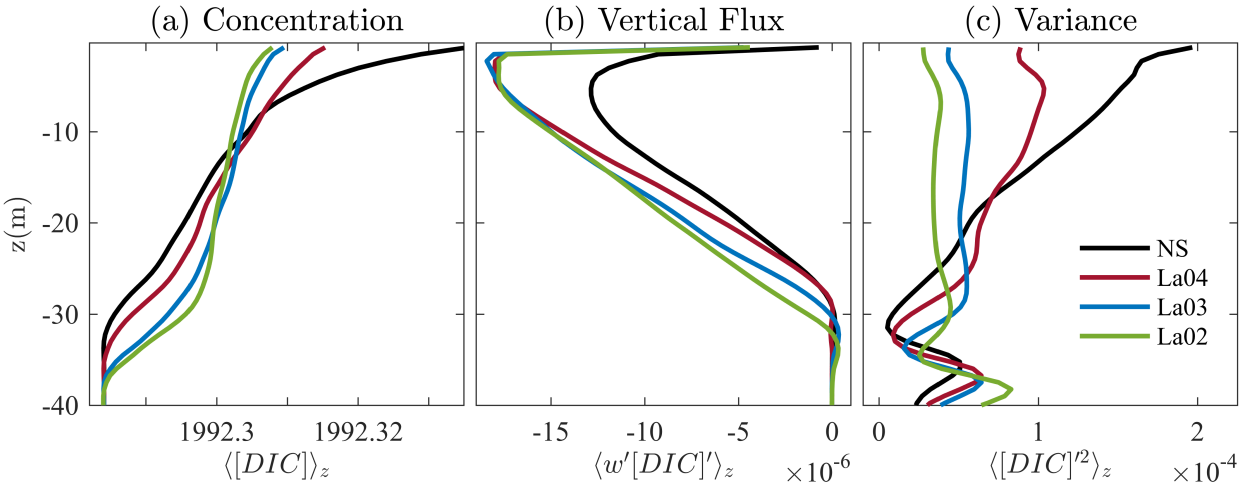

mixing associated with Langmuir turbulence. Figure 3.5(b) shows that the Langmuir cases all exhibit increased downward vertical flux near the surface in comparison to the non-Langmuir case. While their magnitudes are quite similar near the surface, the stronger Langmuir cases have sustained increased flux deeper into the domain.

From Figures 3.4 and 3.5, it is difficult to discern whether the presence of Langmuir turbulence decreases, increases, or has no affect on the amount of additional carbon brought into the domain in comparison to non-Langmuir turbulence. To clarify this, Figure 3.6 shows the total volume integrated change in DIC within the domain for each turbulence case. At first glance, it does not appear that the four cases are different from each other, however, the inset within Figure 3.6 shows the last 10 seconds of the simulations. Here it can clearly be seen that the Langmuir cases have brought in additional DIC in comparison to the non-Langmuir case.

While the Langmuir cases do appear to bring in more carbon into the domain, it is useful to further quantify this increase with respect to the non-Langmuir case. Figure 3.7 shows the percent enhancement in the volume integrated new DIC within the domain as a function of time for each of the four Langmuir cases, calculated according to the following equation

$$(\%\ \text{Enhancement})_i(t) = 100 \times \frac{\Delta DIC_i(t) - \Delta DIC_{NS}(t)}{\Delta DIC_{NS}(t)}\,, \tag{3.17}$$

where percent enhancement is in comparison to the non-Langmuir (NS) case and new (Δ) DIC is any additional carbon brought into the domain after the start of simulations. While the simulations have yet to reach steady-state with respect to percent enhancement, there is a clear trend of increased new carbon within the Langmuir cases in comparison to the non-Langmuir case. For these simulations, this configuration, and after 6 hours of constant forcing, the addition of Langmuir turbulence brings between 0.09-0.14% more carbon into the domain in comparison to the case with just wind-driven, shear turbulence. For reference, if these results were to be extrapolated out to the entire surface ocean, this would add

Figure 3.6: Change in volume integrated DIC within the domian as a function of time for each of the four different turbulence cases ($La = \infty$: black, $La = 0.4$: red, $La = 0.3$: blue, $La = 0.2$: green) for the time-dependent chemistry case. Inset shows change in DIC within the total domain for just the last 10 seconds of simulations.

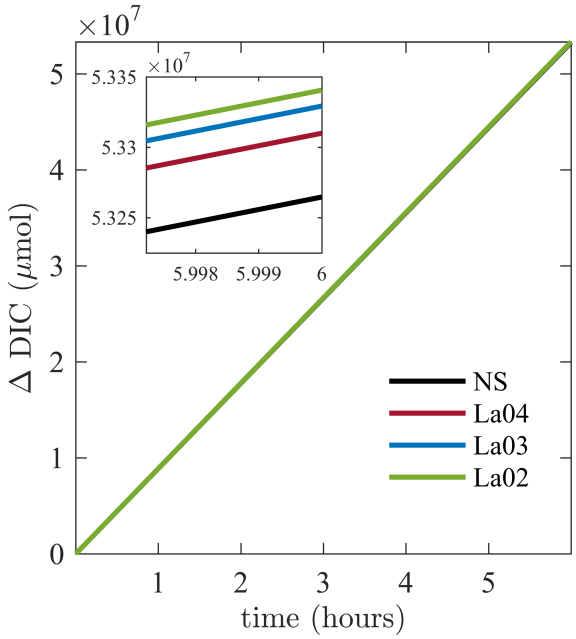

Figure 3.7: Percent enhancement of new DIC brought into the domain in comparison to the non-Langmuir case as a function of time for each of the four different turbulence cases ($La = \infty$: black, $La = 0.4$: red, $La = 0.3$: blue, $La = 0.2$: green) for the time-dependent chemistry case.

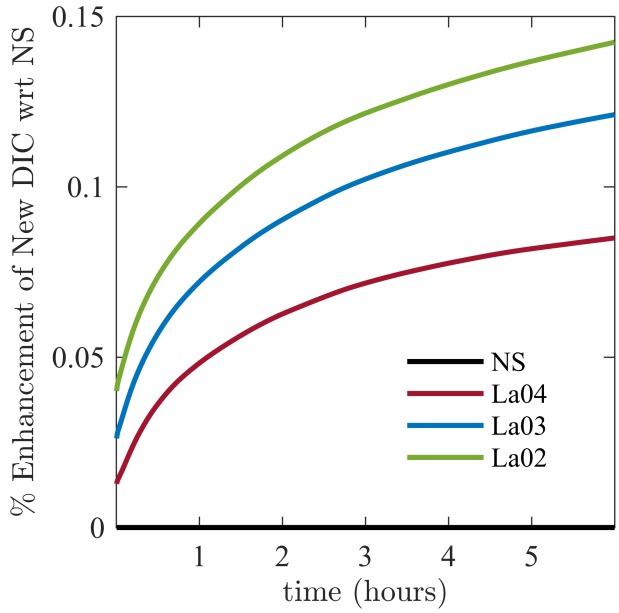

up to approximately ∼0.2-0.3 gigatons of extra carbon per year brought into the ocean due to the presence of Langmuir turbulence. Of course this is assuming that these exact conditions remain constant throughout that year across the entire ocean surface and that the air concentration of CO_2 is always a 10% increase above the ocean concentration, but it serves to demonstrate that Langmuir turbulence can have an appreciable affect on the uptake of carbon by the ocean.

This difference in new DIC brought into the domain is due to differences in the air-sea flux rate of CO_2 at the surface. Figure 3.8 shows the percent change in flux rate as a function of time for each of the four cases. All cases have a sharp initial decline in their air-sea flux rate, however, the non-Langmuir case continues to drop off at a faster rate in comparison to the three Langmuir cases. While the vertical distribution of DIC is helpful in quantifying the total additional carbon that has entered the domain, it is primarily the vertical distribution of CO_2 that causes this drop off in air-sea flux rate of CO_2, as seen in Figure 3.9(a), since the air-sea flux rate is only dependent on CO_2 concentration. If there is a build up CO_2 at the surface, the air-sea gradient in CO_2 concentration decreases, thereby decreasing the air-sea flux rate. If instead the concentration of CO_2 at the surface is kept lower for longer, the air-sea gradient in CO_2 can remain higher and the air-sea flux rate is not cut off as dramatically. Additionally, the decreased variance in CO_2 concentration at the surface for the Langmuir cases (Figure 3.9(c)), results in a decreased variance in CO_2 flux rate in Figure 3.10 in comparison to the non-Langmuir case.

There are two primary processes that affect the vertical distribution of CO_2 and the concentration and variance immediately at the surface: **(i)** the vertical turbulent flux of CO_2 and **(ii)** chemical reactions due to carbonate chemistry that convert CO_2 into bicarbonate and carbonate. First focusing on the vertical turbulent flux, which is directly affected by the presence of Langmuir turbulence, Figure 3.9(b) shows the $x-y$ averaged vertical turbulent flux of CO_2 as a function of depth for each of the four cases. There is a marked decrease in vertical turbulent flux for the non-Langmuir case, which allows for a build up CO_2 within

Figure 3.8: Percent change in the air-sea flux rate of carbon into the domain as a function of time for the four different turbulence cases ($La = \infty$: black, $La = 0.4$: red, $La = 0.3$: blue, $La = 0.2$: green) for the time-dependent chemistry case.

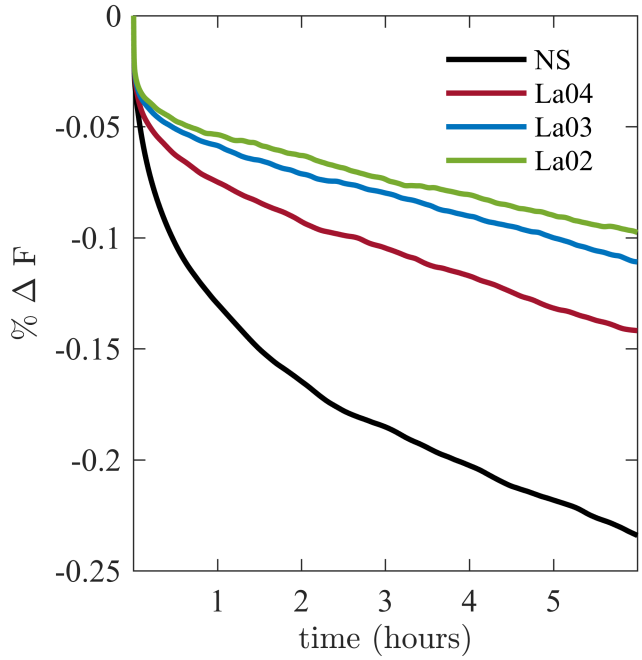

Figure 3.9: $x - y$ averaged (a) concentration, (b) vertical turbulent flux, and (c) variance of CO_2 within the domain as a function of depth for the four different turbulence cases ($La = \infty$: black, $La = 0.4$: red, $La = 0.3$: blue, $La = 0.2$: green) for the time-dependent chemistry case.

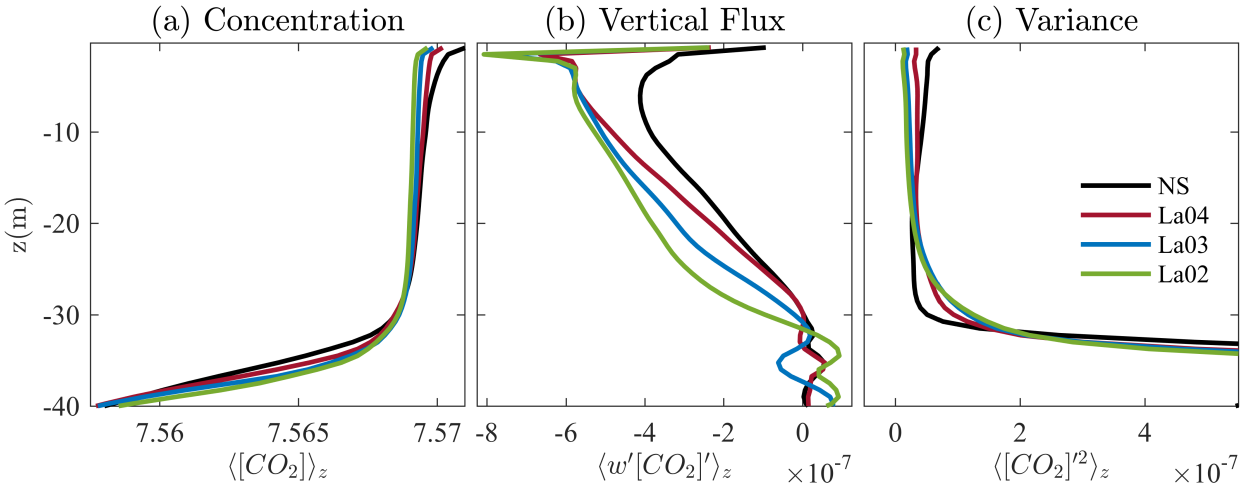

Figure 3.10: Relative change in the variance of the air-sea flux rate of carbon into the domain as a function of time for the three different Langmuir cases ($La = 0.4$: red, $La = 0.3$: blue, $La = 0.2$: green) with respect to the non-Langmuir case for the time-dependent chemsitry case.

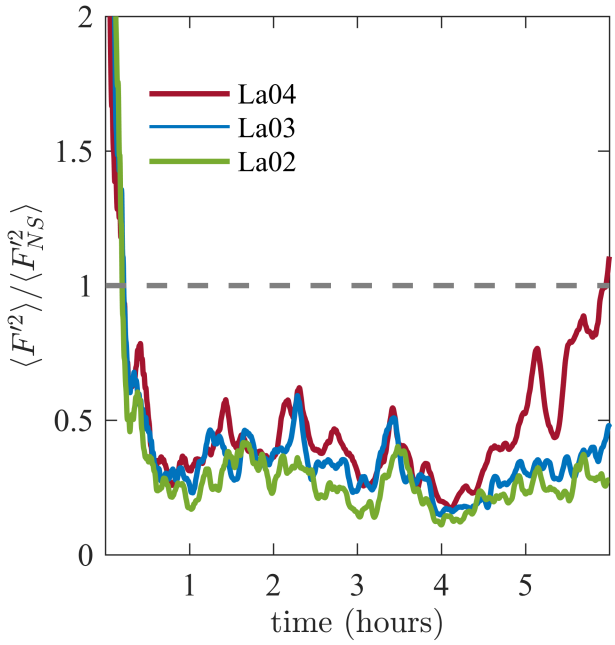

the surface layer, decreasing the air-sea gradient in CO_2, and slowing down the rate at which CO_2 can enter the domain. Conversely, the increased mixing associated with Langmuir turbulence flushes out the surface layer, maintaining a greater air-sea gradient in CO_2, and allowing for a greater air-sea rate. Langmuir turbulence additionally serves to homogenize the surface CO_2 concentration, which reduces the variability in flux rate. However, in these time-dependent chemistry cases (and also the equilibrium chemistry cases as will be shown in the proceeding section), the vertical turbulent flux is only part of the story. In the reactive cases, CO_2 is also being taken away from the surface via carbonate chemistry. In order to isolate these two effects, the next section explores the effect that chemistry has on the enhancement of DIC within the domain and the vertical distribution of CO_2.

3.4.2 Effects of the Chemistry Model

In order to isolate the effect of chemistry on the air-sea flux rate of CO_2 and the resultant enhancement of DIC within the domain, this section compares the shear-only, non-Langmuir, cases for each of the three chemistry models (time-dependent, equilibrium, and no chemistry). For reference, the $La = 0.3$ case is also examined within this section. Figure 3.11 shows the same volume integrated change in DIC within the domain as Figure 3.6, but now for each of the chemistry models (TC, EC, and NC), and the inset in panel shows the TC and EC cases for the last 10 seconds of the simulations. Both the TC and EC cases bring in more carbon into the domain in comparison to the NC case. This is to be expected since carbonate chemistry, in either time-dependent or equilibrium form, provides an additional sink of CO_2 from the surface layer. When comparing the TC and EC cases, it is helpful to remember that reactions in the EC case are instantaneous and thus carbon is instantly converted into its respective portions of CO_2, bicarbonate, and carbonate once it enters the domain, while the TC case has a finite time associated with this conversion. Considering this, it is not surprising that the EC case brings more carbon into the domain over the course of the simulations. With the TC case, CO_2 persists for a finite amount of time before

reacting and/or being taken away by advection, leaving an increased concentration of CO_2 near the surface, slowing down flux rates. With the EC case, this additional CO_2 is instantly converted and surface concentrations increase only slightly due to a total increase in DIC, so flux rates can remain higher. Notably, the same trend between the non-Langmuir case and $La = 0.3$ is seen for each of the different chemistry cases, however, the difference between the two varies based upon the chemistry model.

Figure 3.12 shows the same percent enhancement in the volume integrated new DIC within the domain as a function of time as Figure 3.7, but for each of the chemistry models (TC, EC, and NC) and now the percent enhancement is in comparison to the non-Langmuir, EC case. The non-Langmuir, EC case has been chosen in this section to be the model to compare to as this is the chemistry model and physical set-up used within many ESMs and so serves as the baseline result. Again, the general trends between the non-Langmuir and $La = 0.3$ cases are consistent across the different chemistry cases, with $La = 0.3$ having a greater enhancement, but the differences between the two are dependent on the chemistry model (TC/non-Langmuir to TC/$La = 0.3$: 0.12% increase, EC/non-Langmuir to EC/$La = 0.3$: 0.16% increase, and NC/non-Langmuir to NC/$La = 0.3$: 2.7% increase). Looking at the differences between the chemistry cases, the TC cases arrive at a pseudo steady-state decrease of 0.01% and 0.13% in comparison to the non-Langmuir, EC case. Again for reference, if extrapolated out to the entire ocean for a year, this finite-time "delay" in CO_2 conversion due to the TC chemistry would result in a $\sim$0.02-0.3 gigaton decrease in the uptake of carbon by the ocean in comparison to the instantaneous EC chemistry. In contrast, the NC case, continually decreases in the amount of additional carbon it brings into the domain in comparison to both of the reacting cases, with a much greater drop off in the non-Langmuir case over time.

Figure 3.13 shows the air-sea flux rate of CO_2 as a function of time for the three chemistry cases. It is immediately noticeable that the NC case has a dramatic drop off in air-sea flux rate, so much so that the y-axis is now logarithmic in order to clearly show all

Figure 3.11: Change in volume integrated DIC within the domian as a function of time for each of the three different chemistry cases (TC: solid, EC: dot-dot, NC: dash-dot) for the non-Langmuir (black) and $La = 0.3$ cases (blue). Inset shows change in DIC within the total domain for just the last 10 seconds of simulations.

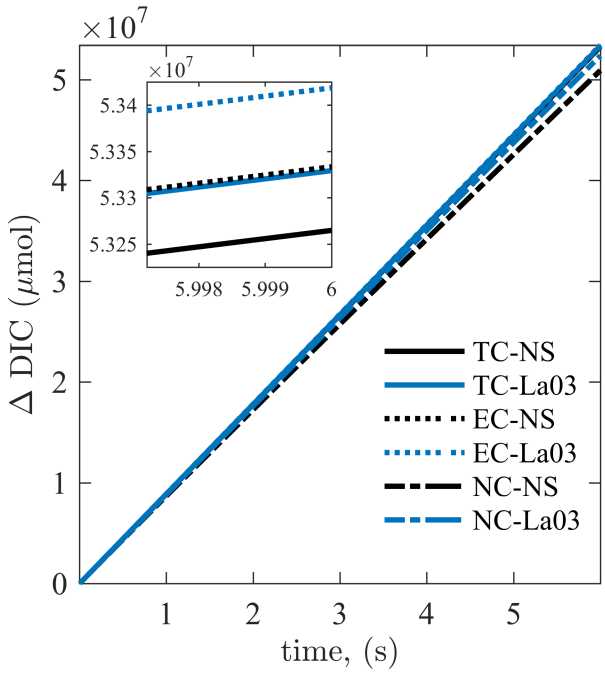

Figure 3.12: Percent enhancement of new DIC brought into the domain in comparison to the equilibrium chemistry case as a function of time for each of the three different chemistry cases (TC: solid, EC: dot-dot, NC: dash-dot) for the non-Langmuir (black) and $La = 0.3$ cases (blue).

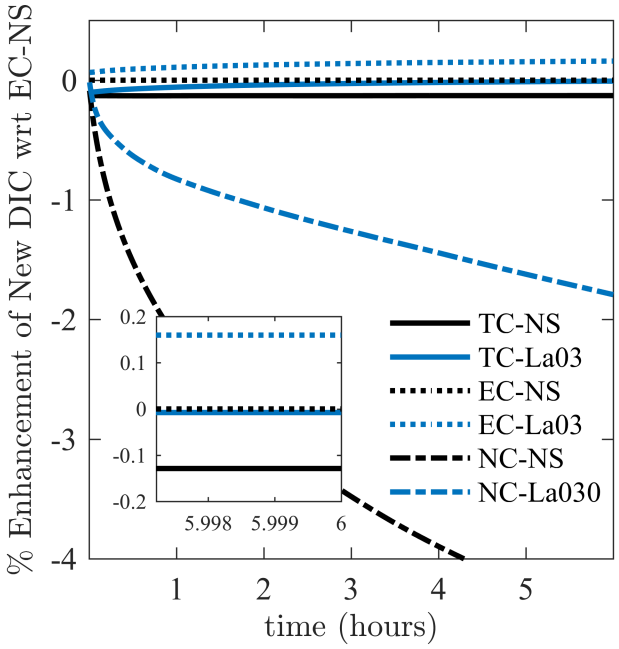

Figure 3.13: Percent change in the air-sea flux rate of carbon into the domain as a function of time for the three different chemistry cases (TC: solid, EC: dot-dot, NC: dash-dot) for the non-Langmuir (black) and $La = 0.3$ cases (blue). y-axis is logarithmic.

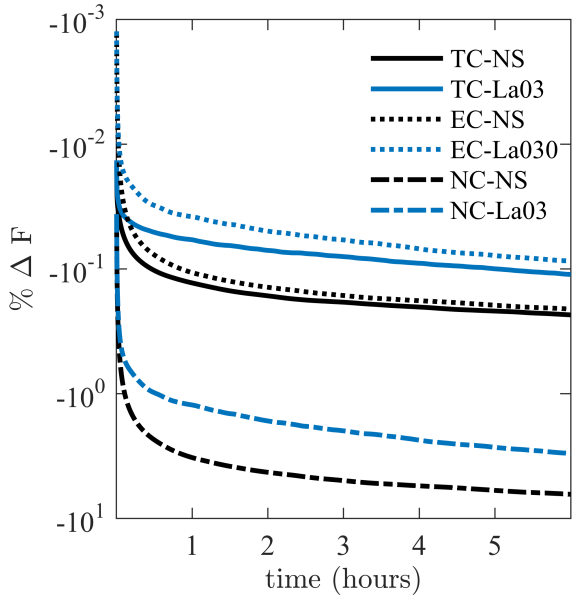

three cases on the same figure. The two reactive cases (TC and EC), instead, have much higher sustained air-sea flux rates. As was stated previously, the air-sea flux rate is primarily dependent on the vertical distribution of CO_2 within the domain. Figure 3.14(a) shows the $x-y$ averaged concentration of CO_2 as a function of depth. The NC case has much greater concentrations of CO_2 near the surface, which decreases the air-sea gradient of CO_2 and lessens the air-sea flux rate. Again, two primary processes effect the vertical distribution of CO_2, the vertical turbulent flux of CO_2 and chemical reactions due to carbonate chemistry. While the vertical turbulent flux of CO_2 for the NC case is much greater than either the TC or EC case, see Figure 3.14(b), the primary reason the concentration of CO_2 at the surface is greater and air-sea flux rate is less in the NC case is due to the lack of chemical reactions. Both the TC and EC cases convert CO_2 into bicarbonate and carbonate, thereby reducing the standing concentration of CO_2 at the surface. This maintains a greater air-sea gradient of CO_2 and allows for more CO_2 to enter the domain. For the reacting cases, the EC cases have elevated flux rates in comparison to the TC case. This is due to the decreased surface concentration of CO_2 in the EC cases (Figure 3.14(a)) and results in the enhanced amount of new DIC brought into the domain. Variance in CO_2 concentration near the surface, seen in Figure 3.14(c), is largest in the NC-NS case and smallest in the EC and TC-La030 cases (not discernible from the figure, however). Figure 3.15 shows the effect this concentration variance has on the variance in flux rate, where the normalizing case is the EC-NS case. While there is a large difference between the non-Langmuir and Langmuir cases (comparing black to blue lines), which was concluded in the previous section as a result of the increased homogenizing effect of fast mixing Langmuir turbulence, there is also a difference between the different chemistry cases (comparing solid, dashed, and dot-dot lines). The absence of reactions increases the variance in flux rate dramatically, again, so much so that the y-axis is logarithmic in order to show the difference. However, differences in the type of reaction (EC vs. TC) do not appear to have a significantly different affect on the variance in flux rate and it is primarily the type of turbulence that dominates.

Figure 3.14: $x-y$ averaged (a) concentration, (b) vertical turbulent flux, and (c) variance of CO_2 within the domain as a function of depth for the three different chemistry cases (TC: solid, EC: dot-dot, NC: dash-dot) for the non-Langmuir (black) and $La = 0.3$ cases (blue).

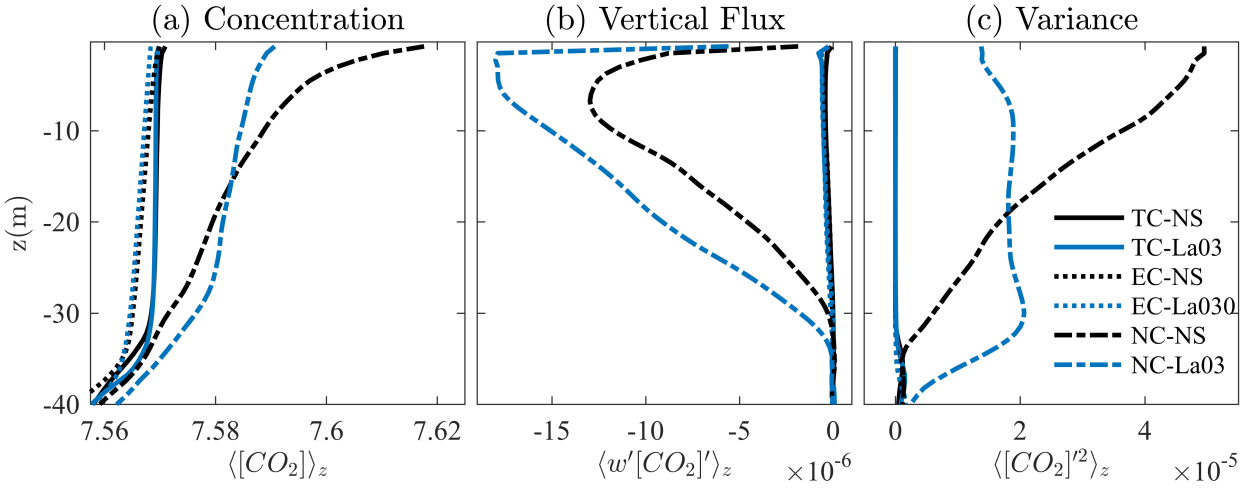

Figure 3.15: Relative change in the variance of the air-sea flux rate of carbon into the domain as a function of time for the three different chemistry cases (TC: solid, EC: dot-dot, NC: dash-dot) with respect to the equilibrium chemsitry, non-Langmuir case for the non-Langmuir (black) and $La = 0.3$ cases (blue). y-axis is logarithmic.

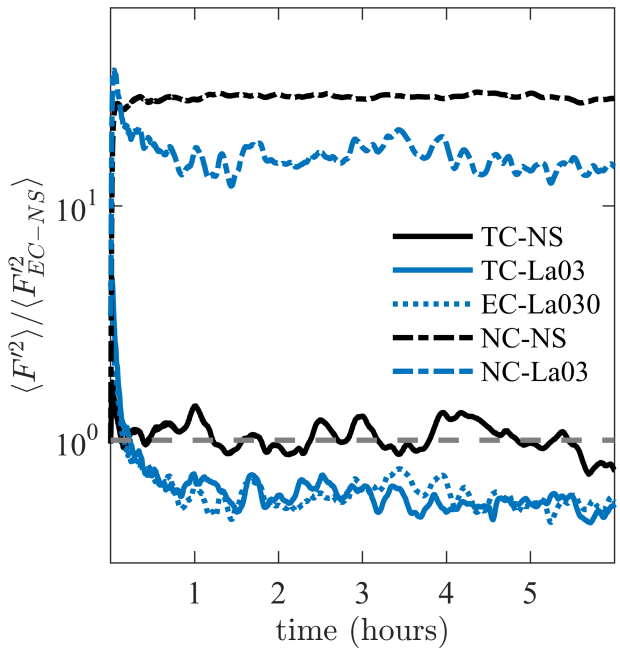

3.4.3 Effects of Langmuir Turbulence and the Chemistry Model

It is clear from the previous sections that both the turbulent vertical flux of CO_2 and chemical reactions due to carbonate chemistry are important in determining the air-sea flux rate of CO_2. However, it is beneficial to examine the combined effects of both. Figure 3.16 shows the percent enhancement in the volume integrated new DIC within the domain at 6 hours into the simulation for each of the three chemistry cases, (a) TC, (b) EC, and (c) NC, for each of the four different turbulence cases. All values have been normalized by the non-Langmuir, time-dependent case which lies at the zero in the left most panel. As was concluded before in the previous sections, in each chemistry case, the Langmuir turbulence cases have an increased enhancement of new DIC in comparison to the non-Langmuir case. Similarly, the equilibrium chemistry case has increased enhancement in comparison to the time-dependent chemistry, which in turn has increased enhancement in comparison to the no-chemistry case. However, it is now clear that the amount of increase that Langmuir turbulence, and also increased strength in Langmuir turbulence, provides is a function of the chemistry model. Langmuir turbulence in the no-chemistry case provides a large increase in the enhancement over just wind-driven shear turbulence, as well as successive increases in the strength of the Langmuir turbulence. Conversely, in both the reactive cases (TC and EC), the enhancement that Langmuir turbulence and increased in Langmuir turbulence strength provide is much smaller. This is to say that, not surprisingly, the presence of chemistry accounts for a large amount of the additional carbon that can be "taken-up" by the domain. However, there are small, and quite interesting, differences between the two reactive cases. For the EC case, the presence of Langmuir turbulence results in a greater enhancement than in the TC case, yet successive increases in Langmuir strength in the EC case have less of an influence on enhancement than compared to the TC case. This can be seen by the (slightly) greater jump from the NS to $La = 0.4$ markers, but a smaller slope between the Langmuir strengths in the EC case panel. So if the tracer reacts with sea water, such as CO_2 does,

Figure 3.16: Percent enhancement of new DIC brought into the domain in comparison to the non-Langmuir, time-dependent chemistry case for the three different chemistry cases ((a) TC = squares, (b) EC = circles, (c) NC = triangles) for each of the four different turbulence cases (La = ∞: black, La = 0.4: red, La = 0.3: blue, La = 0.2: green). Gray dashed lines are a least-square fit for the decrease in percent enhancement as a function of Langmuir number and the gray number is the slope of that fit.

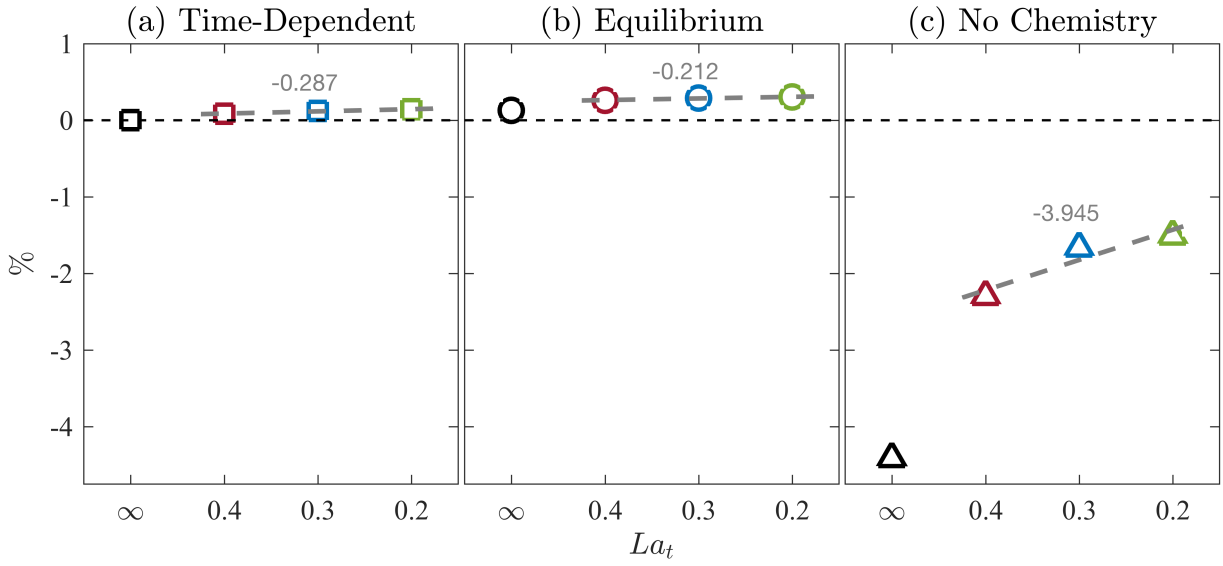

the reactive nature of the tracers accounts for most of the additional tracer brought into the domain, with Langmuir turbulence and the specific form of the chemistry model accounting for a smaller difference. However, if the tracer does not react with sea water, such as O_2, the effects of Langmuir turbulence become much more pronounced and important.

3.4.4 Resolution Study

In order to verify that these results are robust to resolution of the simulations, a resolution study was performed. Four sets of different resolution simulations were run, where the computational grid size was swept through 64^3, 128^3, 256^3, and 512^3, resulting in a horizontal resolution sweep of 5m, 2.5m, 1.25m, and 0.625m, respectively, with corresponding vertical resolutions of 1.5m, 0.75m, 0.375m, and 0.1875m, respectively. The simulations were only run out to 90 seconds, primarily due to computational expenses of the higher resolution runs, however, this was long enough to conclude that the overall conclusions with respect to trends are robust to the resolution used. The absolute conclusions are not expected to remain constant as resolution was changed, since changing the resolution effectively changes the Reynolds number of the simulation in an LES context and a fair comparison of results is no longer appropriate. Panel (a) in Figures 3.17 and 3.18 shows the change in volume integrated DIC within the domain, similarly to Figures 3.6 and 3.11, and panel (b) shows the percent enhancement of new DIC brought into the domain with respect to the non-Langmuir, time-dependent chemistry case and the non-Langmuir, equilibrium chemistry case, respectively, similarly to Figures 3.7 and 3.12. In all cases, the $La = 0.3$ case has an increased amount of carbon brought into the domain with respect to the corresponding resolution non-Langmuir case and the equilibrium chemistry, non-Langmuir case has an increased amount of carbon brought into the domain with respect to the corresponding resolution time-dependent, non-Langmuir case.

Figure 3.17: (a) Change in volume integrated DIC within the domain over 90 seconds for four different resolutions (64^3; black, 128^3; red, 256^3; blue, 512^3; green) for the non-Langmuir (solid) and $La = 0.3$ cases (dot-dot). Inset shows change in DIC within the total domain for just the last 0.05 seconds. (b) Percent enhancement new DIC brought into the domain over 90 seconds by the $La = 0.3$ case in comparison to the non-Langmuir case for four different resolutions (64^3; black, 128^3; red, 256^3; blue, 512^3; green).

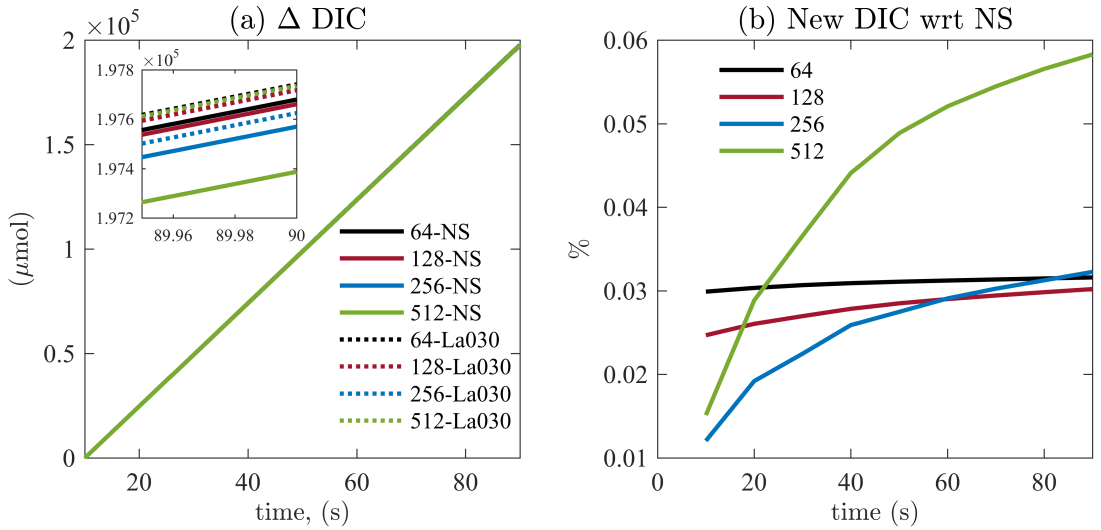

Figure 3.18: (a) Change in volume integrated DIC within the domain over 90 seconds for four different resolutions (64^3; black, 128^3; red, 256^3; blue, 512^3; green) for the time-dependent chemistry (solid) and equilibrium chemistry cases (dot-dot). Inset shows change in DIC within the total domain for just the last 0.05 seconds. (b) Percent enhancement new DIC brought into the domain over 90 seconds by the time-dependent chemistry case in comparison to the equilibrium chemistry case for four different resolutions (64^3; black, 128^3; red, 256^3; blue, 512^3; green).

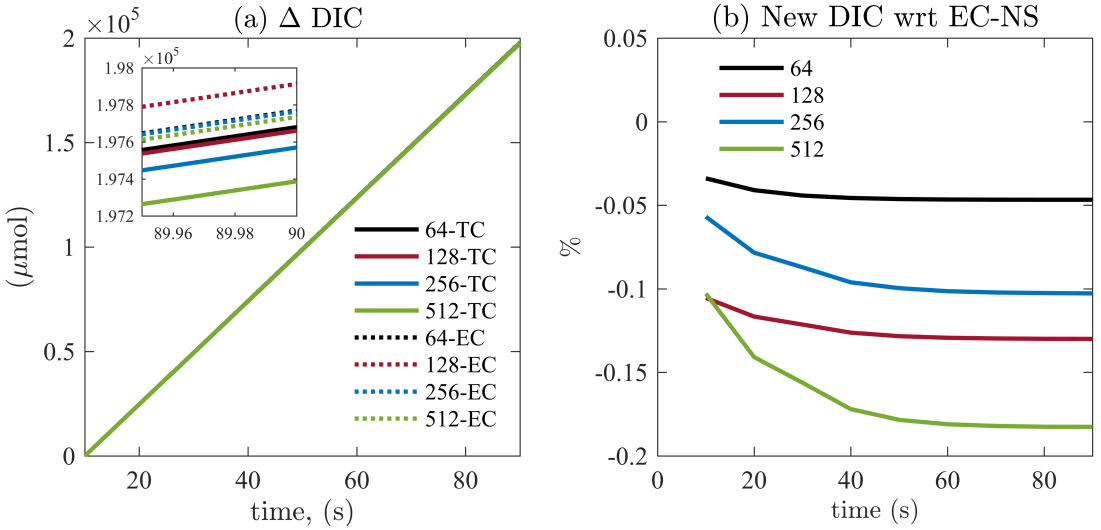

3.5 Conclusions

A set of simulations spanning four different strengths of Langmuir turbulence, from none at all with wind-driven turbulence only to quite strong, and three different types of carbonate chemistry models, from infinitely slow non-reactive chemistry to finite-time chemistry to infinitely fast equilibrium chemistry, were performed in order to determine the effect the presence of Langmuir turbulence has on upper ocean carbonate chemistry. A time-dependent seven-species carbonate chemistry model was integrated into the NCAR-LES model using an RKC integration method and a quasi-steady-state assumption for the hydrogen ion concentration, along with an equilibrium chemistry model commonly used in ESMs and an additional set of seven non-reactive tracers. After an appropriate "spin-up" period, the simulations with different chemistry models were allowed to run for an additional 6 hours after CO_2 was allowed to enter the domain from the top boundary according to a Henry's Law flux rate. Simulations were constantly forced at the top boundary with either just wind-driven shear turbulence or a combination of wind-driven shear turbulence and wave-driven Langmuir turbulence. Results show that the presence of Langmuir turbulence increases the flux rate of CO_2 into the domain approximately $\mathcal{O}(0.1\%)$ in comparison to just wind-driven shear turbulence and as the strength of Langmuir turbulence increases, so does the flux rate of CO_2. Additionally, infinitely fast equilibrium chemistry increases the flux rate of CO_2 into the domain by approximately $\mathcal{O}(0.1\%)$ in comparison to the time-dependent chemistry and by approximately $\mathcal{O}(1-10\%)$ in comparison to the non-reactive chemistry. Both of these effects are due to the ability of each process to remove CO_2 from the surface layer of the domain. Processes that keep the concentration of CO_2 low at the surface increase the overall flux rate of CO_2 into the domain. The combination of different turbulence forcing and chemistry models adds additional complexity, as the impact of Langmuir turbulence, and its increased strength, on the flux rate of CO_2 were found to be different, and opposing, depending on the chemistry model used. While these percent changes are not large with

respect to the global air-sea flux of CO_2, they are on the order of basin-scale differences in flux rate between different ESMs. Current ESM simulations make two assumptions: (*i*) that all small-scale process such as wind-driven shear turbulence and wive-driven turbulence have the same affect and can be parameterized in the same way and (*ii*) that carbonate chemistry is virtually instantaneous in comparison to local turbulent process and thus can be represented by an equilibrium chemistry model. Results from this study suggest that not only can the invoking of these two assumptions potentially lead to errors in the estimate of CO_2 entering the ocean, but that the combination of invoking these two assumptions together is not a simple superposition of errors, but more complex and non-linear.

Chapter 4

Reactive Tracer Development: Development and Testing of a Reduced Order Biogeochemical Model

Within this chapter, a newly developed reduced-order biogeochemical model is presented that is complex and flexible enough to capture open ocean ecosystem dynamics, but reduced enough to incorporate into complex numerical simulations without significant added computational cost. The model follows a biological and chemical functional group approach, allows for the development of critical non-Redfield ratios, and exchanges matter in terms of carbon, nitrogen, and phosphate; a technique taken from its more complex counterparts. However, it eliminates certain processes, such as benthic, silicate, and iron influences, and parameterizes others, such as the bacterial loop, in order to reduce the overall computational cost of the model. The model explicitly tracks 17 state variables, broken up into phytoplankton, zooplankton, dissolved organic matter, particulate organic matter, and inorganic nutrient groups. After presenting the proposed model, its is coupled it to the 1D Princeton Ocean Model (POM) and calibrated and validated using data from the Sargasso Sea. A sensitivity study is performed and the most sensitive parameters are numerically optimized within the model. Results after optimization show good agreement with test case data, including the ability to capture the initial bloom, a subsurface chlorophyll maximum, and the correct bloom intensity. In comparison to reduced order models of similar size, correlations between model output and field data are generally greater. Root mean squared errors are lower for the model proposed here, showing that, with minimal increase in complexity,

significant improvements in ecosystem modeling can be achieved.

4.1 Introduction

Biogeochemical (BGC) tracers and their interactions with upper ocean physical processes, from the basin scales down to the millimeter-size turbulence dissipation scale, are critical for understanding the role of the ocean in the global carbon cycle. These interactions can cause multi-scale spatial and temporal heterogeneity in tracer distributions [6, 36–50] that can, in turn, greatly affect carbon exchange rates between the atmosphere and interior ocean, net primary productivity, and carbon export [149–154]. However, significant gaps in our understanding of how these biophysical interactions develop and evolve still exist, thus limiting our ability to accurately predict critical exchange rates. In order to better understand these interactions, there is a need for both realistic and accurate physical and BGC models that can be coupled together. Relatively realistic and accurate physical models exist, given sufficient resolution and computational resources. The actual resolution and computational cost needed to achieve a realistic and accurate physical model is the topic of many other studies, but at least the exact equations that describe the physics (i.e., the Navier-Stokes equations) are known. However, due to the vast diversity and complexity of ocean ecology, even when only considering the lowest trophic levels, accurately modeling the BGC component can be quite difficult. Put simply, there are no known governing equations for ocean biology.

As such, two different approaches to modeling BGC processes are often taken when faced with this challenge. The first is to increase model complexity and include equations for every known (and even unknown) BGC process. Often, these models include species functional types, or multiple classes of different phytoplankton and/or zooplankton, that each serve a specific functional role within the ecosystem, such as calcifiers or nitrogen fixers. The justification for this approach is that a particular phytoplankton and/or zooplankton groups serve as important system feedback pathways and without these feedbacks explicitly

represented, there is little hope of accurately representing the target ecosystem [155, 156]. In many cases, these models contain variable intra- and extra-cellular nutrient ratios, as well, which are important when accounting for different nutrient regimes within the global ocean and species diversity of non-Redfield nutrient ratio uptake [157]. While these more complex models have been shown to be more easily adaptable to capture vastly different dynamics than those they were calibrated for [158, 159], these models contain many more parameters than their simplified counterparts, most of which are inadequately bounded by either observational and experimental values [68], such as phytoplankton mortality, zooplankton grazing rates, and bacterial remineralization rates. Additionally, because of their increased complexity, it is often difficult to ascertain what processes are responsible for the development of a particular event, and so they can be ill-suited for process studies. Lastly, while these highly complex models are regularly used within global ESMs, they are difficult and sometimes impossible to integrate within high-fidelity, high-resolution physical models at submesoscales (e.q. Smith *et al.* [69]), such as those used for small-scale fundamental understanding and parameterization development studies.

The second approach is to decrease complexity and severely truncate the number of equations used to describe the dynamics of an ecosystem. Such approaches include the well-known nutrient-phytoplankton-zooplankton-detritus (NPZD) class of models. These models provide more transparency when it comes to understanding the dominant forcing underlying an event, have significantly fewer unknown parameters, and can be more easily integrated within complex physical models. However, while they are often capable of reproducing the overall general distributions of chlorophyll, primary production, and nutrients [156], they have been shown to underperform in capturing complex ecosystem dynamics and often struggle in regions of the ocean for which they were not calibrated [159].

Although both of these approaches have their respective advantages, particularly given their vastly different objectives, the disconnect between reduced-order BGC models used within small-scale parameterization studies and the more complex BGC models used within

global ESMs, poses a problem. The lack of direct comparison between the two makes the process of 'scaling-up' of newly developed parameterizations, 'downscaling' of BGC variables within nested-grid studies, and overall inter-comparison between different physical fidelity models much more difficult. All of this motivates the development of a BGC model that is reduced enough to be usable within a high-resolution, high-fidelity physical model for process studies and parameterization development, but is still complex enough to capture important ecosystem feedback dynamics and easily adaptable such that it is able to capture the dynamics of vastly different ecosystems throughout the ocean, as required by ESMs.

In order to address this need, we have developed the reduced-order, 17 state variable Biogeochemical Flux Model (BFM17). Most high-fidelity, high-resolution physical models are capable of integrating 17 additional tracer equations without too much additional computational cost. BFM17 also follows a biological and chemical functional group approach, allows for variable non-Redfield intra- and extra-cellular ratios, and exchanges matter through units of carbon, nitrate, and phosphate. Most notably, BFM17 also includes a phosphate budget, the importance of which has historically been underplayed, even though recent observational data has indicated its potential importance as a limiting nutrient, particularly in the Atlantic Ocean [160]. In order to reduce model complexity, certain processes for which field data is lacking are parameterized, such as bacterial remineralization. Here the model is calibrated for open ocean conditions using observational data from the Sargasso Sea, and so further assumptions are made with this application in mind, such as the lack of a benthic system due to only modeling the upper water column and the absence of limiting nutrients such as iron and silicate.

While other reduced-order BGC models have been calibrated using data from the Sargasso Sea, such as those developed by [161–169], all employ less than 10 species and do not appear to use a chemical functional group approach. With a minimal increase in the number and complexity of equations, such as those associated with tracking phosphate in addition to carbon and nitrate and including both particular and dissolved organic nutrient

budgets, we postulate that a significant increase in model accuracy can be achieved over these other models. Additionally, with this increase in model complexity, the disparate gap between complexity of BGC models used in small-scale studies and global-scale studies is reduced, simplifying 'scaling-up' and 'downscaling' efforts.

In the following, the 0D BFM17 model is introduced in Section 4.2, it is coupled to a 1D physical model in Section 4.3, a discussion of the methods used to calibrate and validate the model with field data collected within the Sargasso Sea are presented in Section 4.4, a sensitivity study of the model is performed within Section 4.5, parameter optimization of the new model is presented within Section 4.6, and lastly, both optimized results, a skill assessment, and a brief comparison to other similar BGC models are discussed in Section 4.7.

4.2 Biogeochemical Flux Model 17 (BMF17)

The 17 state equation Biogeochemical Flux Model (BFM17) is a reduced-order model derived from the original 56 state equation Biogeochemical Flux Model (BFM) [170] which follows the biological and chemical functional group approach. With this approach, functional groups are partitioned into living, non-living organic, and non-living inorganic groups and exchange of matter occurs through units of carbon, nitrate, and phosphate. The approach used to reduce the model was by expert opinion, starting with the assumption that this model is to be used for upper open-ocean, oligotrophic regions and so variable internal nutrient dynamics are important and must be kept within the model. Only one phytoplankton and one zooplankton group are included as they are the bare minimum needed within a BGC model and already account for 6 state equations. Both dissolved and particulate organic matter are included in order to account for both nutrient recycling and carbon export due to particle sinking, both of which are important in this region. Remineralization of nutrients is provided by parameterized bacteria closure terms, thus reducing complexity, yet maintaining critical nutrient recycling. Lastly, we track chlorophyll, dissolved oxygen, phos-

phate, nitrate, and ammonium, as their distribution and availability can greatly enhance or hinder important biological and chemical processes. Notable omissions from this model are silicate and iron. While all of these have been shown to be important components of certain ecosystems, we have chosen here to largely focus on targeting an open ocean ecosystem which is not iron and/or silicate limited. In order to apply this model to a region in which these are important, such as the Southern Ocean, some representation of these processes should be included. Additionally, the original benthic system within BFM was also removed as it is assumed upper ocean ecosystems are not substantially influenced by a benthic system and any water column influences from depth can be taken into account using boundary conditions that are discussed within Section 4.4. A schematic of the functional groups defined in the present model, along with their interaction which each other, is shown in Fig. 4.1.

4.2.1 Equations

Within the BFM17 model, phytoplankton, zooplankton, particulate organic matter, and dissolved organic matter are defined as zero-dimensional vectors comprised of 3 constituents (carbon, nitrogen, and phosphate). Therefore, any of these functional groups can be expressed as the sum of source and sinks of each constituents. The detailed equations for each of the 17 constituents that make up the BFM17 model are presented in the following Section 4.2.2. A summary of the 17 constituents is provided in Table 4.2, definitions for abbreviations used in each equation are defined in Table 4.3, and a summary of parameter values and their descriptions are provided in Tables 4.4-4.6.

4.2.1.1 Environmental Parameters

The 0D BFM17 directly interacts with the environment through temperature and irradiance inputs. Temperature directly affects all physiological processes within the model

Figure 4.1: Flow chart for the 17 state equation biogeochemical flux model.

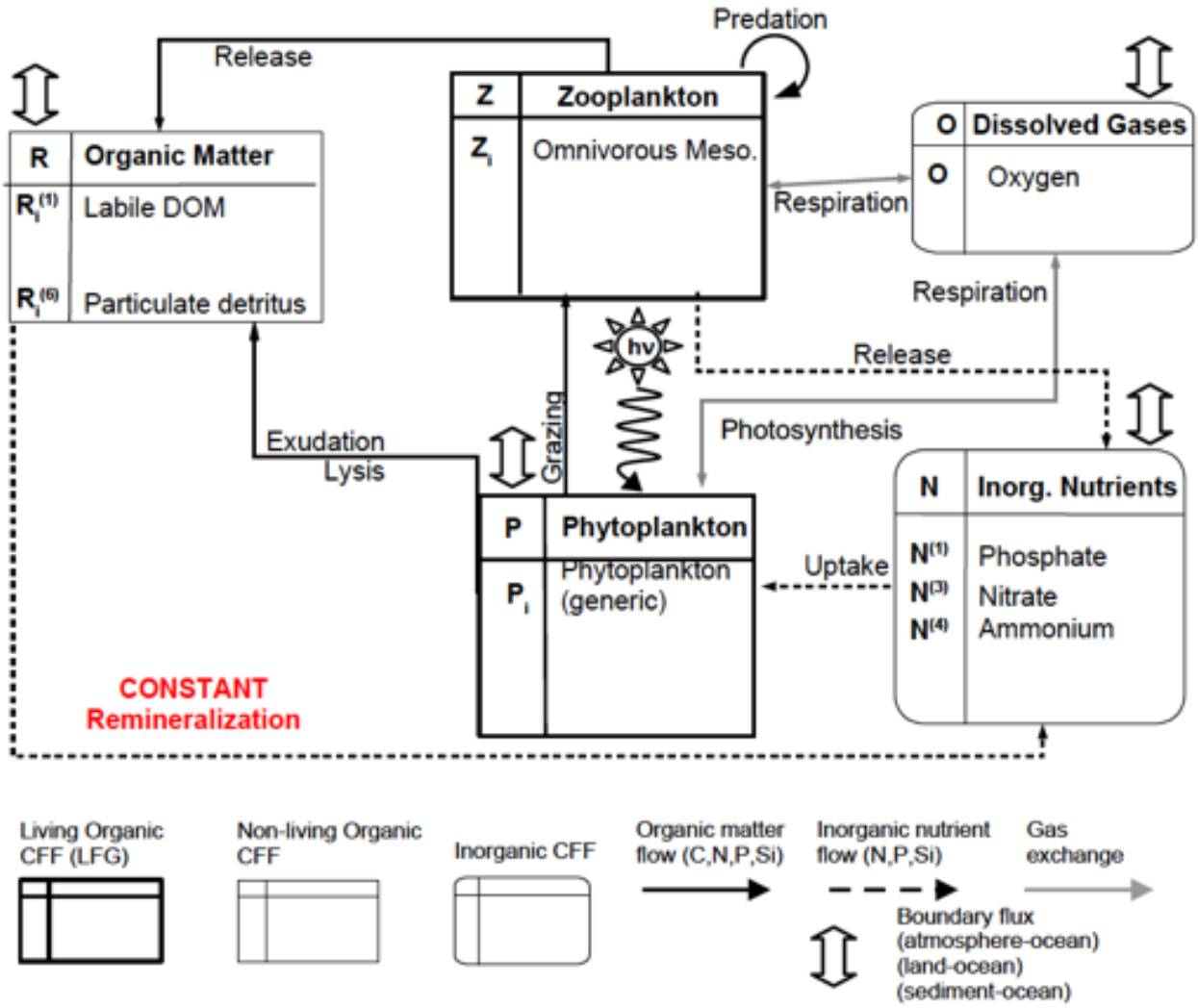

and is parameterized in the following non-dimensional way

$$f^T = Q_{10}^{\frac{T-T^*}{T^*}}\,, \tag{4.1}$$

where T^* is a base temperature and Q_{10} is a coefficient which differs for each process. In contrast to temperature, irradiance only directly affects phytoplankton, serves as their primary energy source for growth and maintenance, and is a function of the incident solar radiation at the sea surface. Within BFM17, the amount of photosynthetic available radiation (PAR)

at any given location is parameterized according to the Lambert-Beer model

$$E_{PAR}(z) = \varepsilon_{PAR} Q_S \exp\left(\lambda_w z + \int_z^0 \lambda_{bio}(z')dz'\right), \tag{4.2}$$

where Q_S is the short-wave surface irradiance flux, ε_{PAR} is the fraction of PAR within Q_S, λ_{bio} is the light extinction due to suspended biological particles, and λ_w is the background light extinction due to water. The biological extinction term is dependent on phytoplankton chlorophyll and particulate detritus and is written as

$$\lambda_{bio} = c_P P_l + c_{R^{(6)}} R_c^{(6)}, \tag{4.3}$$

where c_P and $c_{R^{(6)}}$ are the specific absorption coefficient of phytoplankton and particulate detritus, respectively.

4.2.1.2 Phytoplankton Equations

Phytoplankton in the model are composed of three constituents (carbon, phosphorous, and nitrogen) for which source terms can broken be up into gross primary production (*gpp*), respiration (*rsp*), cell lysis (*lys*), nutrient uptake (*upt*), exudation (*exu*), and predation (*prd*). The following section details the source terms for each of the three phytoplankton constituents.

(1) Phytoplankton - Carbon

$$\frac{\partial \mathbf{P_c}}{\partial \mathbf{t}} = \frac{\partial \mathbf{P_c}}{\partial \mathbf{t}}\bigg|_{\mathbf{CO_2}}^{\mathbf{gpp}} - \frac{\partial \mathbf{P_c}}{\partial \mathbf{t}}\bigg|_{\mathbf{CO_2}}^{\mathbf{rsp}} - \frac{\partial \mathbf{P_c}}{\partial \mathbf{t}}\bigg|_{\mathbf{R_c^{(1)}}}^{\mathbf{lys}} - \frac{\partial \mathbf{P_c}}{\partial \mathbf{t}}\bigg|_{\mathbf{R_c^{(6)}}}^{\mathbf{lys}} - \frac{\partial \mathbf{P_c}}{\partial \mathbf{t}}\bigg|_{\mathbf{R_c^{(1)}}}^{\mathbf{exu}} - \frac{\partial \mathbf{P_c}}{\partial \mathbf{t}}\bigg|_{\mathbf{Z_c}}^{\mathbf{prd}} \tag{4.4}$$

(2) Phytoplankton - Phosphorous

$$\frac{\partial \mathbf{P_p}}{\partial \mathbf{t}} = \frac{\partial \mathbf{P_p}}{\partial \mathbf{t}}\bigg|_{\mathbf{N^{(1)}}}^{\mathbf{upt}} - \frac{\partial \mathbf{P_p}}{\partial \mathbf{t}}\bigg|_{\mathbf{R_p^{(1)}}}^{\mathbf{lys}} - \frac{\partial \mathbf{P_p}}{\partial \mathbf{t}}\bigg|_{\mathbf{R_p^{(6)}}}^{\mathbf{lys}} - \frac{\partial \mathbf{P_p}}{\partial \mathbf{t}}\bigg|_{\mathbf{Z_p}}^{\mathbf{prd}} \tag{4.5}$$

(3) Phytoplankton - Nitrogen

$$\frac{\partial \mathbf{P_n}}{\partial \mathbf{t}} = \frac{\partial \mathbf{P_n}}{\partial \mathbf{t}}\bigg|_{\mathbf{N^{(3)}}}^{\mathbf{upt}} + \frac{\partial \mathbf{P_n}}{\partial \mathbf{t}}\bigg|_{\mathbf{N^{(4)}}}^{\mathbf{upt}} - \frac{\partial \mathbf{P_n}}{\partial \mathbf{t}}\bigg|_{\mathbf{R_n^{(1)}}}^{\mathbf{lys}} - \frac{\partial \mathbf{P_n}}{\partial \mathbf{t}}\bigg|_{\mathbf{R_n^{(6)}}}^{\mathbf{lys}} - \frac{\partial \mathbf{P_n}}{\partial \mathbf{t}}\bigg|_{\mathbf{Z_n}}^{\mathbf{prd}} \tag{4.6}$$

Phytoplankton gross primary production is dependent on two non-dimensional regulation factors for temperature and light, the maximum photosynthetic rate, and the current local concentration of phytoplankton

$$\left.\frac{\partial P_c}{\partial t}\right|_{CO_2}^{gpp} = f_P^T f_P^E r_P^0 P_c \,, \tag{4.7}$$

where f_P^T is the temperature regulation factor for phytoplankton described in Section 4.2.1.1, r_P^0 is the maximum photosynthetic rate, and $f_P^E = 1 - \exp\left(-E_{PAR}/E_K\right)$ is the light regulation factor of [171], where $E_k = \left(r_P^0/\alpha_{chl}^0\right)\left(P_c/P_l\right)$ and α_{chl}^0 is the maximum light utilization coefficient.

Phytoplankton respiration is parameterized as the sum of the basal respiration and activity respiration rates

$$\left.\frac{\partial P_c}{\partial t}\right|_{CO_2}^{rsp} = b_P f_P^T P_c + \gamma_P \left.\frac{\partial P_c}{\partial t}\right|_{CO_2}^{gpp} \,, \tag{4.8}$$

where b_P is the basal specific respiration rate and γ_P is the activity respiration fraction.

Phytoplankton lysis includes all mortality due to mechanical, viral, and yeast cell disruption processes and is partitioned between particulate and dissolved detritus. Structural parts of the cell are released to particulate detritus, while the internal cytoplasm is released to dissolved detritus.

$$\left.\frac{\partial P_i}{\partial t}\right|_{R_c^{(1)}}^{lys} = \left(1 - \varepsilon_P^{n,p}\right)\left(\frac{h_P^{p,n}}{f_P^{n,p} + h_P^{n,p}} d_P^0 P_i\right) \,, \quad i = c, n, p \,, \tag{4.9}$$

$$\left.\frac{\partial P_i}{\partial t}\right|_{R_c^{(6)}}^{lys} = \varepsilon_P^{n,p}\left(\frac{h_P^{p,n}}{f_P^{n,p} + h_P^{n,p}} d_P^0 P_i\right) \,, \quad i = c, n, p \,, \tag{4.10}$$

where $h_P^{p,n}$ is the nutrient stress threshold, d_P^0 is the maximum specific nutrient-stress lysis rate, and

$$\varepsilon_P^{n,p} = \min\left(1, \frac{p_p^{min}}{P_p/P_c}, \frac{n_p^{min}}{P_n/P_c}\right) \,, \tag{4.11}$$

which ensures that nutrients within the structural parts of the cell, which are less degradable, are always released particulate detritus. $f_P^{n,p} = \min\left(f_P^n, f_P^p\right)$ is the multiple nutrient

limitation term, which allows for the internal storage of nutrients and is dependent on the respective nutrient limitation terms for both nitrate and phosphate

$$f_P^n = \min\left[1, \max\left(0, \frac{P_n/P_c - n_p^{min}}{n_P^{opt} - n_P^{min}}\right)\right], \tag{4.12}$$

$$f_P^p = \min\left[1, \max\left(0, \frac{P_p/P_c - p_p^{min}}{p_P^{opt} - p_P^{min}}\right)\right], \tag{4.13}$$

where n_p^{min} and p_p^{min} are the minimum phytoplankton quotas for nitrogen and phosphorus, respectively, and n_p^{opt} and p_p^{opt} are the optimal phytoplankton quotas for nitrogen and phosphorus, respectively.

Nutrient uptake threshold control within BFM17 combines both the intracellular quota (Droop equations) and external concentration (Monod equations) approaches [172]. Phytoplankton uptake of inorganic nitrogen is the minimum between a diffusion-dependent uptake rate (when internal nutrient quotas are low) and a rate that is based upon balanced growth needs and any excess uptake

$$\Sigma_{j=3,4}\left.\frac{\partial P_n}{\partial t}\right|_{N^{(j)}}^{upt} = \varepsilon_P^{(i)} \min\left[\left(a_P^n \frac{h_P^n}{h_P^n + N^{(4)}} N^{(3)} + a_P^n N^{(4)}\right) P_c, n_P^{opt} G_P + \nu_P \left(n_P^{max} - \frac{P_n}{P_c}\right) P_c\right], \tag{4.14}$$

where the first term is the diffusion-dependent uptake, the second is balanced uptake, and the third is excess uptake. Balanced uptake is a function of net primary production, given as

$$G_P = \max\left(0, \left.\frac{\partial P_c}{\partial t}\right|_{CO_2}^{gpp} - \left.\frac{\partial P_c}{\partial t}\right|_{R_c^{(1)}}^{exu} - \left.\frac{\partial P_c}{\partial t}\right|_{CO_2}^{rsp} - \left.\frac{\partial P_i}{\partial t}\right|_{R_c^{(1)}}^{lys} - \left.\frac{\partial P_i}{\partial t}\right|_{R_c^{(6)}}^{lys}\right). \tag{4.15}$$

When the phytoplankton nitrogen uptake rate is positive, the relative portions from nitrate and ammonium are determined with the following fractions

$$\varepsilon_P^{(3)} = \frac{a_P^n \frac{h_P^n}{h_P^n + N^{(4)}} N^{(3)}}{a_P^n N^{(4)} + a_P^n \frac{h_P^n}{h_P^n + N^{(4)}} N^{(3)}}, \tag{4.16}$$

$$\varepsilon_P^{(4)} = \frac{a_P^n N^{(4)}}{a_P^n N^{(4)} + a_P^n \frac{h_P^n}{h_P^n + N^{(4)}} N^{(3)}}. \tag{4.17}$$

However, a preference for ammonium is achieved through the following saturation function

$$\nu_P = \max\left(0.05, \frac{G_P}{P_c}\right) . \tag{4.18}$$

When phytoplankton inorganic nitrogen uptake rate is negative, the entire nitrogen flux goes to the dissolved organic nitrogen pool, $R_n^{(1)}$.

Inorganic phosphorus uptake is similar to that of nitrogen, in that it is the minimum of a diffusion-dependent rate and a balanced growth/excess uptake rate, however it comes entirely from one pool

$$\left.\frac{\partial P_p}{\partial t}\right|_{N^{(1)}}^{upt} = \min\left[a_P^p N^{(1)} P_c, p_P^{opt} G_P + \nu_P \left(p_P^{max} - \frac{P_p}{P_c}\right) P_c\right] . \tag{4.19}$$

Just like with nitrogen, if the uptake rate is positive, it comes from the inorganic phosphate pool and if it is negative, the entire phosphorus flux goes to the dissolved organic phosphorus pool, $R_p^{(1)}$.

If phytoplankton cannot equilibrate their fixed carbon with sufficient nutrients, this carbon is not assimilated and is instead released in the form of dissolved inorganic carbon, otherwise known as exudation. Exudation within BFM17 is parameterized as

$$\left.\frac{\partial P_c}{\partial t}\right|_{R_c^{(1)}}^{exu} = \left[\beta_P + (1-\beta_P)(1-f_P^{n,p})\right] \left.\frac{\partial P_c}{\partial t}\right|_{CO_2}^{gpp} \tag{4.20}$$

where β_P is the excreted fraction of primary production.

Lastly, predation of phytoplankton within BFM17 is solely performed by zooplankton and is equal and opposite to the zooplankton predation terms that will be presented in the next section.

4.2.1.3 Zooplankton Equations

Zooplankton in the model are composed of three constituents (carbon, phosphorous, and nitrogen) for which source terms can broken be up into growth due to predation of phytoplankton (*prd*), respiration (*rsp*), and release due to excretion/egestion (*rel*). The following section details the source terms for each of the three zooplankton constituents.

(4) Zooplankton - Carbon

$$\frac{\partial \mathbf{Z_c}}{\partial \mathbf{t}} = \frac{\partial \mathbf{Z_c}}{\partial \mathbf{t}}\bigg|_{\mathbf{P_c}}^{\mathbf{prd}} - \frac{\partial \mathbf{Z_c}}{\partial \mathbf{t}}\bigg|_{\mathbf{CO_2}}^{\mathbf{rsp}} - \frac{\partial \mathbf{Z_c}}{\partial \mathbf{t}}\bigg|_{\mathbf{R_c^{(1)}}}^{\mathbf{rel}} - \frac{\partial \mathbf{Z_c}}{\partial \mathbf{t}}\bigg|_{\mathbf{R_c^{(6)}}}^{\mathbf{rel}} \tag{4.21}$$

(5) Zooplankton - Phosphorous

$$\frac{\partial \mathbf{Z_p}}{\partial \mathbf{t}} = \frac{\partial \mathbf{Z_p}}{\partial \mathbf{t}}\bigg|_{\mathbf{P_p}}^{\mathbf{prd}} - \frac{\partial \mathbf{Z_p}}{\partial \mathbf{t}}\bigg|_{\mathbf{R_p^{(1)}}}^{\mathbf{rel}} - \frac{\partial \mathbf{Z_p}}{\partial \mathbf{t}}\bigg|_{\mathbf{R_p^{(6)}}}^{\mathbf{rel}} - \frac{\partial \mathbf{Z_p}}{\partial \mathbf{t}}\bigg|_{\mathbf{N^{(1)}}}^{\mathbf{rel}} \tag{4.22}$$

(6) Zooplankton - Nitrogen

$$\frac{\partial \mathbf{Z_n}}{\partial \mathbf{t}} = \frac{\partial \mathbf{Z_n}}{\partial \mathbf{t}}\bigg|_{\mathbf{P_n}}^{\mathbf{prd}} - \frac{\partial \mathbf{Z_n}}{\partial \mathbf{t}}\bigg|_{\mathbf{R_n^{(1)}}}^{\mathbf{rel}} - \frac{\partial \mathbf{Z_n}}{\partial \mathbf{t}}\bigg|_{\mathbf{R_n^{(6)}}}^{\mathbf{rel}} - \frac{\partial \mathbf{Z_n}}{\partial \mathbf{t}}\bigg|_{\mathbf{N^{(4)}}}^{\mathbf{rel}} \tag{4.23}$$

Zooplankton predation of phytoplankton is primarily dependent on the availability of phytoplankton and their capture efficiency

$$\frac{\partial Z_i}{\partial t}\bigg|_{P_i}^{prd} = \frac{F_i}{F_c}\left(f_Z^T r_Z^0 \frac{F_c}{F_c + h_Z^F} Z_c\right), \quad i = c, n, p, \tag{4.24}$$

where $F_i = \delta_{Z,P} e_{Z,P} P_i$ and is the food availability, $\delta_{Z,P}$ is the availability of phytoplankton, $e_{Z,P}$ is the capture efficiency, f_Z^T is the temperature regulating factor for zooplankton growth, r_Z^0 is the potential specific growth rate, and h_Z^F is the Michaelis constant for total food ingestion.

Zooplankton respiration is the sum of active and basal metabolism rates, where active respiration is the cost of nutrient ingestion, or predation, (1 - assimilation - egestion)

$$\frac{\partial Z_c}{\partial t}\bigg|_{CO_2}^{rsp} = (1 - \eta_Z - \beta_z)\frac{\partial Z_i}{\partial t}\bigg|_{P_i}^{prd} + b_Z f_Z^T Z_c \tag{4.25}$$

where η_Z is the assimilation efficiency, β_Z is the excreted fraction uptake, b_Z is the basal specific respiration rate.

The excretion/egestion term is a sum of zooplankton excretion/egestion and mortality. Excretion/egestion is the portion of ingested nutrients, or predation, that has not been assimilated or used for respiration. Zooplankton mortality is parameterized as the sum

of a constant mortality rate and a oxygen dependent regulation factor. The total excretion/egestion term is partitioned into particulate and dissolved organic matter.

$$\left.\frac{\partial Z_i}{\partial t}\right|_{R_i^{(1)}}^{rel} = \varepsilon_Z^i \beta_Z \left.\frac{\partial Z_i}{\partial t}\right|_{P_i}^{prd} + \left(d_{0Z} + d_Z^0 \left(1 - f_Z^0\right) f_Z^T Z_i\right) , \tag{4.26}$$

$$\left.\frac{\partial Z_i}{\partial t}\right|_{R_i^{(6)}}^{rel} = \left(1 - \varepsilon_Z^i\right) \left.\frac{\partial Z_i}{\partial t}\right|_{R_i^{(1)}}^{rel} , \tag{4.27}$$

where ε_Z^i is the fraction that is excreted to the dissolved pool.

4.2.1.4 Dissolved Organic Matter Equations

Dissolved organic matter in the model is composed of three constituents (carbon, phosphorous, and nitrogen) for which source terms can broken be up into phytoplankton lysis (*lys*) and exudation (*exu*), zooplankton excretion/egestion (*rel*), and remineralization. The following section details the source terms for each of the three DOM constituents.

(7) Dissolved Organic Matter - Carbon

$$\frac{\partial \mathbf{R_c^{(1)}}}{\partial \mathbf{t}} = \left.\frac{\partial \mathbf{P_c}}{\partial \mathbf{t}}\right|_{\mathbf{R_c^{(1)}}}^{\mathbf{lys}} + \left.\frac{\partial \mathbf{P_c}}{\partial \mathbf{t}}\right|_{\mathbf{R_c^{(1)}}}^{\mathbf{exu}} + \left.\frac{\partial \mathbf{Z_c}}{\partial \mathbf{t}}\right|_{\mathbf{R_c^{(1)}}}^{\mathbf{rel}} - \alpha_{\mathbf{R^{(1)})}}^{\mathbf{sink_c}} \mathbf{R_c^{(1)}} \tag{4.28}$$

(8) Dissolved Organic Matter - Phosphorous

$$\frac{\partial \mathbf{R_p^{(1)}}}{\partial \mathbf{t}} = \left.\frac{\partial \mathbf{P_p}}{\partial \mathbf{t}}\right|_{\mathbf{R_p^{(1)}}}^{\mathbf{lys}} + \left.\frac{\partial \mathbf{Z_p}}{\partial \mathbf{t}}\right|_{\mathbf{R_p^{(1)}}}^{\mathbf{rel}} - \alpha_{\mathbf{R^{(1)})}}^{\mathbf{N^{(1)}}} \mathbf{R_p^{(1)}} \tag{4.29}$$

(9) Dissolved Organic Matter - Nitrogen

$$\frac{\partial \mathbf{R_n^{(1)}}}{\partial \mathbf{t}} = \left.\frac{\partial \mathbf{P_n}}{\partial \mathbf{t}}\right|_{\mathbf{R_n^{(1)}}}^{\mathbf{lys}} + \left.\frac{\partial \mathbf{Z_n}}{\partial \mathbf{t}}\right|_{\mathbf{R_n^{(1)}}}^{\mathbf{rel}} - \alpha_{\mathbf{R^{(1)})}}^{\mathbf{N^{(4)}}} \mathbf{R_n^{(1)}} \tag{4.30}$$

All terms except for remineralization have been defined in previous sections. Remineralization of dissolved organic matter by bacteria is parameterized within BFM17 as $\alpha_{R^{(1)}}^{sink_i} R_i^{(1)}$ where the rate is proportional to the local concentration of that dissolved constituent and $\alpha_{R^{(1)})}^{sink_i}$ is a constant that controls the rate at which the respective dissolved constituent is remineralized and returned to the pool of inorganic carbon, nitrate, or phosphate.

4.2.1.5 Particulate Organic Matter Equations

Particulate organic matter in the model is composed of three constituents (carbon, phosphorous, and nitrogen) for which source terms can broken be up into phytoplankton lysis (*lys*) and exudation (*exu*), zooplankton excretion/egestion (*rel*), and remineralization. The following section details the source terms for each of the three POM constituents.

(10) Particulate Organic Matter - Carbon

$$\frac{\partial \mathbf{R_c^{(6)}}}{\partial \mathbf{t}} = \frac{\partial \mathbf{P_c}}{\partial \mathbf{t}}\bigg|_{\mathbf{R_c^{(6)}}}^{\mathbf{lys}} + \frac{\partial \mathbf{P_c}}{\partial \mathbf{t}}\bigg|_{\mathbf{R_c^{(6)}}}^{\mathbf{exu}} + \frac{\partial \mathbf{Z_c}}{\partial \mathbf{t}}\bigg|_{\mathbf{R_c^{(6)}}}^{\mathbf{rel}} - \alpha_{\mathbf{R^{(6)})}}^{\mathbf{sink_c}} \mathbf{R_c^{(6)}} \tag{4.31}$$

(11) Particulate Organic Matter - Phosphorous

$$\frac{\partial \mathbf{R_p^{(6)}}}{\partial \mathbf{t}} = \frac{\partial \mathbf{P_p}}{\partial \mathbf{t}}\bigg|_{\mathbf{R_p^{(6)}}}^{\mathbf{lys}} + \frac{\partial \mathbf{Z_p}}{\partial \mathbf{t}}\bigg|_{\mathbf{R_p^{(6)}}}^{\mathbf{rel}} - \alpha_{\mathbf{R^{(6)})}}^{\mathbf{N^{(1)}}} \mathbf{R_p^{(6)}} \tag{4.32}$$

(12) Particulate Organic Matter - Nitrogen

$$\frac{\partial \mathbf{R_n^{(6)}}}{\partial \mathbf{t}} = \frac{\partial \mathbf{P_n}}{\partial \mathbf{t}}\bigg|_{\mathbf{R_n^{(6)}}}^{\mathbf{lys}} + \frac{\partial \mathbf{Z_n}}{\partial \mathbf{t}}\bigg|_{\mathbf{R_n^{(6)}}}^{\mathbf{rel}} - \alpha_{\mathbf{R^{(6)})}}^{\mathbf{N^{(4)}}} \mathbf{R_n^{(6)}} \tag{4.33}$$

All terms except for remineralization have been defined in previous sections. Remineralization of particular organic matter by bacteria is parameterized within BFM17 as $\alpha_{R^{(6)}}^{sink_i} R_i^{(6)}$ where the rate is proportional to the local concentration of that particulate constituent and $\alpha_{R^{(6))}}^{sink_i}$ is a constant that controls the rate at which the respective particulate constituent is remineralized and returned to the pool of inorganic carbon, nitrate, or phosphate.

4.2.1.6 Dissolved Nutrient and Chlorophyll Equations

Dissolved nutrients in the model are composed of four constituents (oxygen [O], phosphate [$N^{(1)}$], nitrate [$N^{(3)}$], and ammonium [$N^{(4)}$]) for which source terms can broken be up into phytoplankton gross primary production (*gpp*) and nutrient uptake (*upt*), phytoplankton and zooplankton respiration (*rsp*), zooplankton excretion/egestion (*rel*), remineralization (*rel*), nitrification (*nit*), and denitrification (*denit*). Phytoplankton chlorophyll in the model

is comprised of one constituent for which source terms can be broken up into chlorophyll synthesis (*syn*) and chlorophyll loss (*loss*). The following section details the source terms for each of these constituents.

(13) Dissolved Oxygen

$$\frac{\partial \mathbf{O}}{\partial \mathbf{t}} = \mathbf{\Omega_c^o}\left(\left.\frac{\partial \mathbf{P_c}}{\partial \mathbf{t}}\right|_{\mathbf{CO_2}}^{\mathbf{gpp}} - \left.\frac{\partial \mathbf{P_c}}{\partial \mathbf{t}}\right|_{\mathbf{CO_2}}^{\mathbf{rsp}} - \left.\frac{\partial \mathbf{Z_c}}{\partial \mathbf{t}}\right|_{\mathbf{CO_2}}^{\mathbf{rsp}} - \alpha_{\mathbf{R^{(6)}})}^{\mathbf{sink_c}}\mathbf{R_c^{(6)}} - \alpha_{\mathbf{R^{(1)}})}^{\mathbf{sink_c}}\mathbf{R_c^{(1)}}\right) - \mathbf{\Omega_n^o}\left.\frac{\partial \mathbf{N^{(4)}}}{\partial \mathbf{t}}\right|_{\mathbf{N^{(3)}}}^{\mathbf{nit}} \tag{4.34}$$

(14) Dissolved Phosphate

$$\frac{\partial \mathbf{N^{(1)}}}{\partial \mathbf{t}} = -\left.\frac{\partial \mathbf{P_p}}{\partial \mathbf{t}}\right|_{\mathbf{N^{(1)}}}^{\mathbf{upt}} + \alpha_{\mathbf{R^{(1)}})}^{\mathbf{N^{(1)}}}\mathbf{R_p^{(1)}} + \alpha_{\mathbf{R^{(6)}})}^{\mathbf{N^{(1)}}}\mathbf{R_p^{(6)}} + \left.\frac{\partial \mathbf{Z_p}}{\partial \mathbf{t}}\right|_{\mathbf{N^{(1)}}}^{\mathbf{rel}} \tag{4.35}$$

(15) Dissolved Nitrate

$$\frac{\partial \mathbf{N^{(3)}}}{\partial \mathbf{t}} = -\left.\frac{\partial \mathbf{P_n}}{\partial \mathbf{t}}\right|_{\mathbf{N^{(3)}}}^{\mathbf{upt}} + \left.\frac{\partial \mathbf{N^{(3)}}}{\partial \mathbf{t}}\right|_{\mathbf{N^{(4)}}}^{\mathbf{nit}} \tag{4.36}$$

(16) Dissolved Ammonium

$$\frac{\partial \mathbf{N^{(4)}}}{\partial \mathbf{t}} = -\left.\frac{\partial \mathbf{P_n}}{\partial \mathbf{t}}\right|_{\mathbf{N^{(4)}}}^{\mathbf{upt}} + \alpha_{\mathbf{R^{(1)}})}^{\mathbf{N^{(4)}}}\mathbf{R_n^{(1)}} + \alpha_{\mathbf{R^{(6)}})}^{\mathbf{N^{(4)}}}\mathbf{R_n^{(6)}} + \left.\frac{\partial \mathbf{Z_p}}{\partial \mathbf{t}}\right|_{\mathbf{N^{(1)}}}^{\mathbf{rel}} - \left.\frac{\partial \mathbf{N^{(4)}}}{\partial \mathbf{t}}\right|_{\mathbf{N^{(3)}}}^{\mathbf{nit}} \tag{4.37}$$

(17) Chlorophyll

$$\frac{\partial \mathbf{P_l}}{\partial \mathbf{t}} = \left.\frac{\partial \mathbf{P_l}}{\partial \mathbf{t}}\right|^{\mathbf{syn}} - \left.\frac{\partial \mathbf{P_l}}{\partial \mathbf{t}}\right|^{\mathbf{loss}} \tag{4.38}$$

All terms except for nitrification have been defined in previous sections. Nitrification is a source term for inorganic nitrogen and is parameterized as a sink of ammonium and oxygen

$$\left.\frac{\partial N^{(3)}}{\partial t}\right|_{N^{(4)}}^{nit} = \Lambda_{N^{(4)}}^{nit} f_n^T \frac{O}{O + h_o} N^{(4)} \tag{4.39}$$

where $\Lambda_{N^{(4)}}^{nit}$ is the specific nitrification rate, f_n^T is the temperature regulating factor for the nitrification process, and h_o is the half saturation for chemical processes.

Phytoplankton chlorophyll is unique with respect to all other constituents within the model in that it is largely a diagnostic variable (save for its influence on light extinction within

the water column). The phytoplankton chlorophyll source term is made up of only two terms, chlorophyll synthesis and loss. Net chlorophyll synthesis is a function of acclimation to light conditions, availability of nutrients, and turnover rate

$$\left.\frac{\partial P_l}{\partial t}\right|^{syn} = \rho_{chl} G_P - \frac{P_l}{P_c}\left(\left.\frac{\partial P_c}{\partial t}\right|^{lys}_{R_c^{(1)}} + \left.\frac{\partial P_c}{\partial t}\right|^{lys}_{R_c^{(6)}} + \left.\frac{\partial P_c}{\partial t}\right|^{rsp}_{CO_2}\right) \tag{4.40}$$

where ρ_{chl} regulates the amount of chlorophyll in the phytoplankton cell. ρ_{chl} is computed according to a ratio between the realized photosynthetic rate (gross primary production) and the maximum potential photosynthesis proposed by [173]

$$\rho_{chl} = \theta^0_{chl} \frac{f^E_P r^0_P P_c}{\alpha^0_{chl} E_{PAR} P_l} \tag{4.41}$$

where α^0_{chl} is the maximum chlorophyll to carbon quota. Chlorophyll loss is simpler and is just a function of predation, where the amount of chlorophyll transferred back to the infinite sink is proportional to the carbon predated by zooplankton.

4.2.2 0D Test

A test run of the zero-dimensional BFM17 model was run for 10 years with sinusoidal forcing for the temperature, salinity, 10m wind-speed, and PAR where winter and summer values were (20°C, 30°C), (36.98, 36.45), (200 W/m^2, 300 W/m^2), and (6.5 m/s, 3.5 m/s), respectively. Figure 4.2 plots the seasonal cycle of surface chlorophyll, phosphate, and nitrate over that 10 year period showing that consistent and stable seasonal cycle with reasonable ecosystem values can be maintained by the reduced model.

4.3 Coupled Physical-Biogeochemical Flux 17 Model

In the following sections, we describe the coupled one-dimensional physical and BFM17 model. The coupled physical and BFM17 model is a time-depth model that integrates in time the following equation for all 17 biological state variables (A_j)

$$\frac{\partial A_j}{\partial t} = \left.\frac{\partial A_j}{\partial t}\right|_{bio} - (W + W_E + v^{sed})\frac{\partial A_j}{\partial z} + \frac{\partial}{\partial z}\left(K_H \frac{\partial A_j}{\partial z}\right). \tag{4.42}$$

Figure 4.2: 10 year seasonal cycle of surface (a) chlorophyll, (b) phosphate, and (c) nitrate from test run of 0D BFM17.

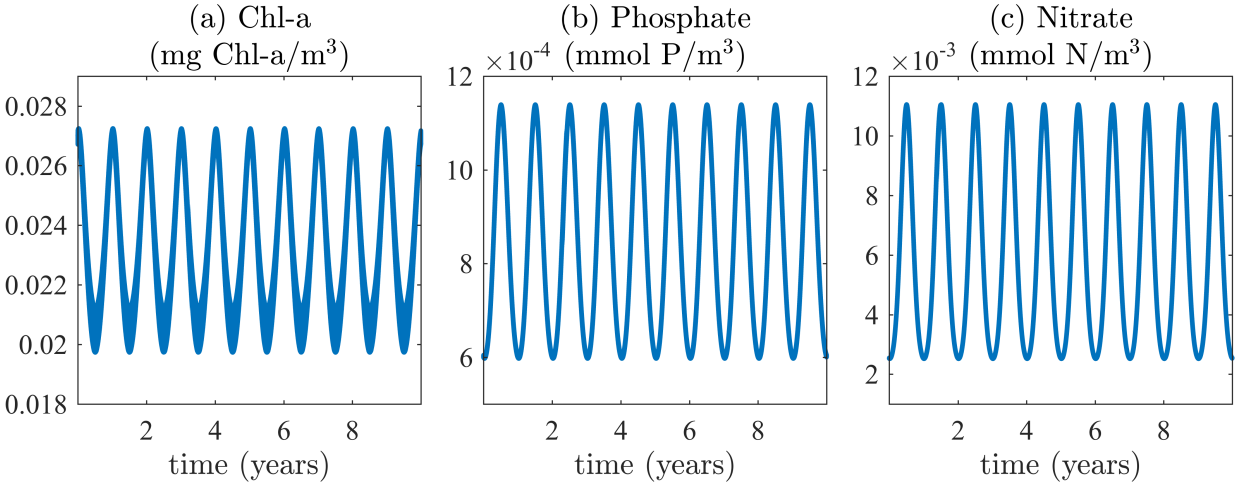

v^{sed} is the settling velocity of the species ($v^{sed} = 0$ for all dissolved species) and comes from the specific assumptions within BFM17 as well as the first term on the right hand side, which accounts for sources and sinks within each species due to biological and chemical reactions. The specific form of this first term for each of the 17 species is provided by BFM17 and were discussed in the previous Section 4.2.2. The physical model provides W as the large-scale general circulation velocity, W_E as the mesoscale eddy vertical velocity, and K_H as the vertical eddy diffusivity term. Surface boundary conditions for the coupled model variable A_j are

$$K_H \frac{\partial A_j}{\partial z}\bigg|_{z=0} = 0\,, \tag{4.43}$$

for all variables except for oxygen, which has the following form

$$K_H \frac{\partial A_j}{\partial z}\bigg|_{z=0} = F_j\,, \tag{4.44}$$

where F_j is the air-sea interface flux of oxygen computed according to [79]. Bottom boundary conditions for phytoplankton, zooplankton, dissolved organic matter, and particulate organic matter are

$$K_H \frac{\partial A_j}{\partial z}\bigg|_{z=-H} = \left(W + W_E + v^{sed}\right) A_j\,, \tag{4.45}$$

and for oxygen, phosphate, and nitrate are

$$K_H \frac{\partial A_j}{\partial z}\bigg|_{z=-H} = \lambda_j \left(A_j|_{z=-H} - A_j^* \right) , \tag{4.46}$$

where λ_j and A_j^* are the corresponding relaxation velocity and observed at-depth climatological field data value, respectively, of that species. Lastly, the bottom boundary condition of ammonium is dependent on the at-depth gradient of dissolved organic nitrogen

$$K_H \frac{\partial [N^{(4)}]}{\partial z}\bigg|_{z=-H} = \kappa_j \frac{\partial [R_n^{(6)}]^*}{\partial z} , \tag{4.47}$$

where κ_j is a relaxation diffusivity.

The one-dimensional Princeton Ocean Model [174] physical equations are solved in order to get the turbulent diffusivity term within Eq. 4.42. POM is used in a "diagnostic" mode, in which one-dimensional vertical profiles of temperature and salinity are linearly interpolated in time from given climatological monthly profiles and the model prognostically computes the horizontal velocities (U, V) and the turbulent viscosity and diffusivity (K_M, K_H) using a surface climatological wind stress. POM solves the following differential equations for momentum

$$\frac{\partial U}{\partial t} - fV = \frac{\partial}{\partial z}\left(K_M \frac{\partial U}{\partial z} \right) , \tag{4.48}$$

$$\frac{\partial V}{\partial t} + fU = \frac{\partial}{\partial z}\left(K_M \frac{\partial V}{\partial z} \right) , \tag{4.49}$$

where $f = 2\Omega \sin\phi$ is the Coriolis force, Ω is the angular velocity of the Earth, and ϕ is the latitude. The vertical diffusivities are calculated using the closure hypothesis of [175], which takes the form of $K_M(z) = qlS_H$, where S_H is an empirical function given in [175]. Here q is the turbulent kinetic energy and l is a turbulent length scale, given by the following

equations

$$\frac{\partial}{\partial t}\left(\frac{q^2}{2}\right) = \frac{\partial}{\partial z}\left(K_M \frac{\partial q^2/2}{\partial z}\right) + P_s + P_b - \varepsilon\,, \tag{4.50}$$

$$P_s = -\left\langle wu\right\rangle \frac{\partial U}{\partial z} - \left\langle wv\right\rangle \frac{\partial V}{\partial z}\,, \tag{4.51}$$

$$P_b = \beta g \left\langle w\theta\right\rangle_v\,, \tag{4.52}$$

$$\frac{\partial}{\partial t}\left(q^2 l\right) = \frac{\partial}{\partial z}\left(K_M \frac{\partial q^2 l}{\partial z}\right) + E_1\left[P_s + P_b\right] - \frac{q^3}{B_1}\tilde{W}\,, \tag{4.53}$$

where P_s and P_b are the turbulent kinetic energy production shear and buoyancy, respectively, ε is the dissipation due to turbulence, β is the coefficient of thermal expansion, g is gravity, θ is potential temperature, $\tilde{W}$ is a function of the distance between rigid boundaries, and E_1 and B_1 are empirical constants. Boundary conditions for U and V are

$$K_M \frac{\partial U}{\partial z}\bigg|_{z=0} = \tau_w^{(x)}\,, \tag{4.54}$$

$$K_M \frac{\partial V}{\partial z}\bigg|_{z=0} = \tau_w^{(y)}\,, \tag{4.55}$$

$$K_M \frac{\partial \overleftarrow{U}}{\partial z}\bigg|_{z=-H} = 0\,, \tag{4.56}$$

where $\tau_w^{(x)}$ and $\tau_w^{(y)}$ are the components of the surface wind stress. The boundary conditions for the turbulent kinetic energy are

$$q^2\big|_{z=0} = B_1^{2/3}\frac{\left|\overleftarrow{\tau}_w\right|}{C_d}\,, \tag{4.57}$$

$$q^2\big|_{z=-H} = 0\,. \tag{4.58}$$

4.4 Field Validation and Calibration Data

4.4.1 Study Site Description

Field data for calibration and validation was collected from the Bermuda Atlantic Time-series Study (BATS) and the Bermuda Testbed Mooring (BTM) sites, which are located in the Sargasso Sea (31°40' N, 64°10' W) in the North Atlantic subtropical gyre. Both sites

are a part of the US Joint Global Ocean Flux Study (JGOFS) program. Data has been collected from the BATS site since 1988 and the BTM site since 1994 and is freely available at http://bats.bios.edu/index.html and http://opl.ucsb.edu/html-old/btm.html. Ref. [176] provides an overview of the biogeochemistry in the general BATS and BTM area. Winter mixing allows nutrients to be brought up into the mixed layer, producing a bloom between January and March. As thermal stratification intensifies over the summer months, this nutrient supply is cut off. At this point a subsurface chlorophyll maximum can be observed around 100m. Stoichiometric ratios of carbon, nitrate, and phosphate are often non-Redfield and in contrast to many oligotrophic regimes phosphate is the dominant limiting nutrient [160, 176–181].

4.4.2 Data Processing

The region encompassing the BATS site is characterized as being an open ocean, oligotrophic region that is phosphate limited. Motivation for choosing the BATS region includes the extensive, long time series data available for this region, the prevalence of oligotrophic regimes within the open ocean, and its phosphate limited characteristic (which is unique in the global ocean), as this allows us to demonstrate the ability of BFM17 to capture difficult non-Redfield ratio regimes (which are not unique in the global ocean). Data from the BATS area is used in this study for two purposes: (i) as initial, boundary, and forcing conditions for the simulations and (ii) as target fields to compare the results of the simulations and help guide parameter value optimization. In addition to the BATS data, we use surface data from the Bermuda Testbed Mooring (BTM) such as the 10m wind speed and photosynthetically available radiation (PAR). For each variable, we compute monthly averages over the 27 years for the BATS data and 23 years (not continuous) for the BTM data. Additionally, for the BATS data, we interpolate the data to a 1m vertical grid resolution and then vertically smooth in order to maintain a positive buoyancy gradient, thereby eliminating any false introduction of spurious buoyant mixing due to interpolation and averaging. Figure 4.3

Figure 4.3: Sargasso Sea Physical Variables: Climatological monthly averaged (a) temperature (C) and (b) salinity (-). Monthly averaged surface (c) PAR (W/m^2) and (d) 10m Wind Speed (m/s). Mean (e) seasonal general circulation W velocity (m/s) and (f) bimonthly mesoscale eddy W velocity (m/s).

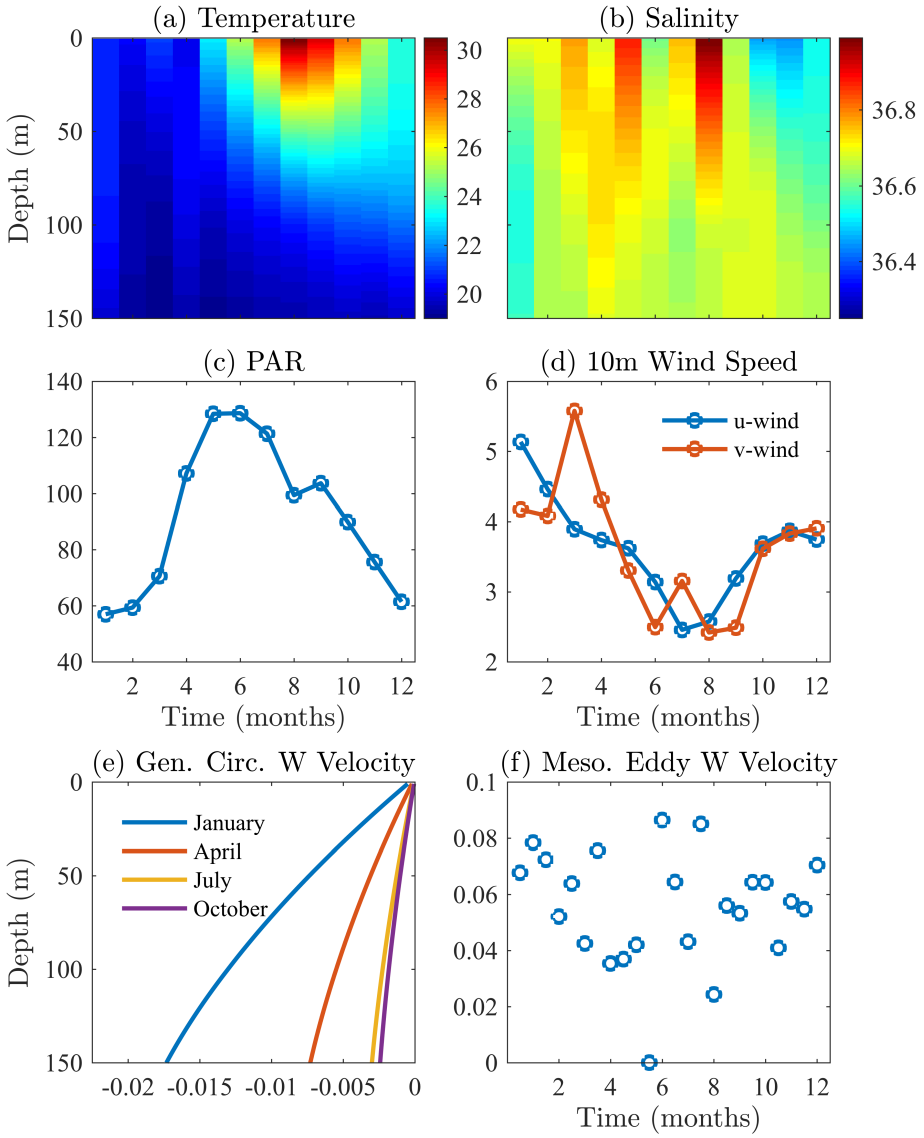

shows the monthly climatological profiles of both the (a) temperature and (b) salinity using the BATS data and the (c) PAR and (d) 10m wind speed using the BTM data. Similar processing is done on the biological variables, which will largely serve as the target fields in evaluating the performance of BFM17 and optimization of parameters. Figure 4.4 shows the

Figure 4.4: Sargasso Sea Biological Variables: Climatological monthly averaged (a) chlorophyll (mg Chl-a/m^3), (b) oxygen (mmol O/m^3), (c) nitrate (mmol N/m^3), (d) phosphate (mmol P/m^3), (e) particulate organic nitrogen (PON - mg N/m^3), (f) and net primary production (NPP - mg C/m^3/day).

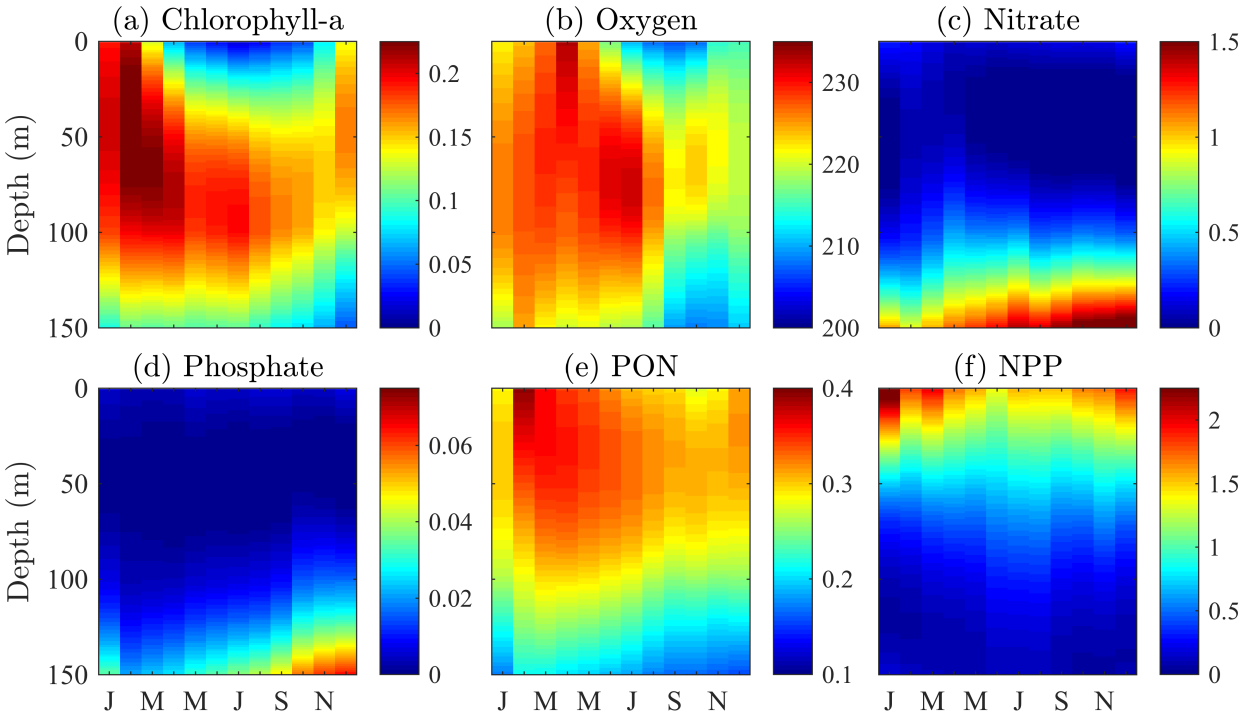

(a) chlorophyll, (b) oxygen, (c) nitrate, (d) phosphate, (e) particulate organic nitrogen, and (f) net primary production fields from the BATS data.

4.4.3 Inputs to the Physical Model

The physical mode computes density from temperature and salinity, and surface wind stress from the 10m wind-speed, both provided by BATS data, and uses it in the turbulence closure model for the computation of the turbulent viscosity and diffusivity. This approach eliminates any drifts in temperature and salinity that might occur due to improper parameterizations of lateral mixing in a one-dimensional model and therefore provides greater reliability. In addition to the 10m wind-speed, temperature, and salinity, BFM17 requires

monthly varying PAR at the surface. For all the monthly mean input data sets, a Killworth correction [182] is applied to the monthly averages in order to account for monthly mean errors due to linear interpolation to the model time step. The temperature, salinity, 10m wind speed, and PAR are shown in Fig. 4.3(a-d).

Lastly, we imposed both a general circulation (W) and a mesoscale eddy (W_E) vertical velocity. The form of both velocities has been adopted from [7], where they are zero at the surface and reach their maximum near the base of Ekman layer, which is assumed to be at or below the bottom boundary of these simulation. The general large scale upwelling/downwelling circulation due to Ekman pumping can be described by the following equation

$$W = \hat{k} \cdot \overrightarrow{\nabla} \times \left(\frac{\overrightarrow{\tau}_w}{\rho f} \right) . \tag{4.59}$$

The monthly average value and sign of the wind stress curl, $\overrightarrow{\nabla} \times \overrightarrow{\tau}_w$, for the general BATS region was taken from Scatterometer Climatology of Ocean Winds (SCOW) database available at cioss.coas.oregonstate.edu/scow. The monthly value calculated for W from this equation is then assumed to be the maximum, occurring at the base of the Ekman layer, for that particular month. Given the sign of the wind stress curl for the BATS region, a negative W was calculated, indicating general downwelling processes in this region. Seasonal profiles of W are shown in Fig. 4.3(e).

Due to the prevalence of mesoscale eddies within this region [183], which can provide episodic upwelling of nutrients to the upper water column, we include an additional positive upwelling vertical velocity (W_E) which has a timescale of 15 days. The general profile of W_E remains the same as W, where it is zero at the surface and maximum at depth, however, there is no linear interpolation between each 15 day period and the maximum magnitude of W_E is randomized between 0 and 0.1 m/d. Fig. 4.3(f) shows the maximum magnitude of W_E for each 15 day period.

4.4.4 Boundary and Initial Conditions

Although the BATS region measures many biological variables, initial conditions for only 5 of the 17 species within BFM17 could be extracted from the data. Similarly to the temperature and salinity, the initial chlorophyll, particulate organic carbon, oxygen, nitrate, and phosphate were interpolated to a 1m vertical grid spacing, averaged over the initial month, and smoothed vertically in space to give the initial profiles seen in Fig. 4.5(b). The remaining 12 species initial conditions were determined either through the use of the Redfield ratio (106:16:1) or an assumed reasonable initial value. Since the one-dimensional simulations are run to steady state over 10 years, memory of these initial states are assumed to be lost and therefore have little effect on the results.

The oxygen, nitrate, phosphate, and ammonium species use observed BATS data for

Figure 4.5: Sargasso Sea Boundary and Initial Conditions: (a) Monthly bottom boundary conditions for nitrate, phosphate, ammonium, and oxygen. Each quantity is normalized by their mean annual value shown in parentheses. (b) Initial profiles of nitrate, phosphate, particulate organic carbon, chlorophyll, and oxygen. Each profile is normalized by their mean depth values shown in parentheses. Units: nitrate (mmol N/m^3), phosphate (mmol P/m^3), ammonium (mmol N/m^3), oxygen (mmol O/m^3), particulate organic carbon (mg C/m^3), and chlorophyll (mg Chl/m^3).

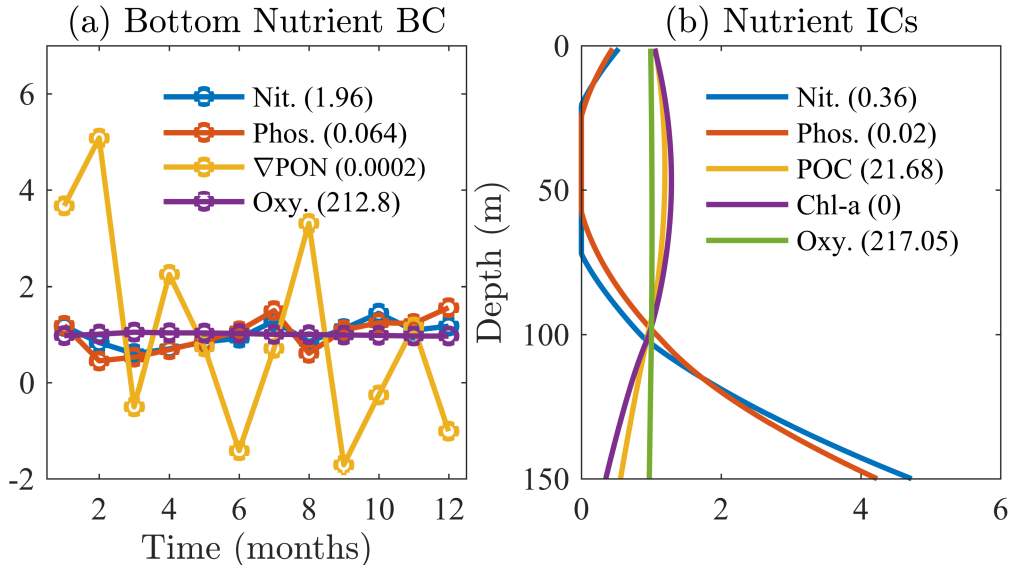

their bottom boundary conditions. For oxygen, nitrate, and phosphate, values are taken at the next closest data point below the bottom boundary (at 150m) and then averaged over the month. For ammonium, we average over all data points between 125-150m and 150-175m across each month for the particulate organic nitrogen, compute the gradient, and then assume the ammonium exhibits a similar gradient. Figure 4.5(a) shows the monthly average bottom boundary conditions for each of the four species.

4.5 Parameter Reduction by Sensitivity Experiments

Within BFM17, there are 56 parameters (see Tables 4.4-4.6), some of which cannot be reliably prescribed from literature. Prescribing values to biological parameters has always been a problematic task, partially due to the lack of experimental and field data for a wide range of biological species. However, more of the difficulty lies within the fact that we are limited in representing a vast and extremely diverse ecosystem, filled with thousands of different plankton species, with models that contain at most three to four different autotrophic and heterotrophic groups (and this is only within the most complex BGC models) [156]. In this study, the method we have chosen to improve calibration of the model is that of parameter optimization. However, before we employ this method, it is helpful to gain some knowledge regarding the sensitivity of the model to each of the parameters in order to reduce the number over which we need to optimize.

A sensitivity study was performed, similar to that in [165], where each parameter was perturbed, both up and down (most cases doubling and halving, respectively), from baseline values used in a base case simulation, which were determined using expert knowledge and literature values, and the model was run out to steady-state. After steady-state is reached, a multi-year monthly-mean normalized sensitivity was calculated for each target BATS field according to

$$S(x) = \left[\frac{\chi(x) - \chi_{BASE}}{\chi_{BASE}}\right] \Big/ \left[\frac{p - p_{BASE}}{p_{BASE}}\right] \tag{4.60}$$

where χ is the mean of any of the 6 target BATS fields, p is the specific parameter being perturbed, and the subscript $BASE$ denotes the base case. Figure 4.6 shows the normalized sensitivity for chlorophyll, oxygen, nitrate, phosphate, particular organic nitrogen (PON), and net primary production for each parameter that was perturbed. A total of 54 parameters were perturbed, the numbers on the vertical axis correspond to the parameters listed in Table 4.4. Any parameter with a value over 1 was categorized as sensitive, those with values above 0.3 categorized as mildly sensitive, and those less than 0.3 categorized as relatively insensitive.

Figure 4.6: Sensitivies of model target fields to each model parameter. Lighter bars with light grey boarders represent the mean sensitivity due to perturbing the parameter upwards (generally by a factor of 2) and darker bars with black boarders are due to perturbing the parameter downwards (generally by a factor of 0.5). Bars are respectively color coated according to whether they are a phytoplankton parameter (red), a zooplankton parameter (blue), or other parameter (green). Vertical dashed lines indicate values greater than 1 (or less than -1), which are categorized a model sensitive parameters.

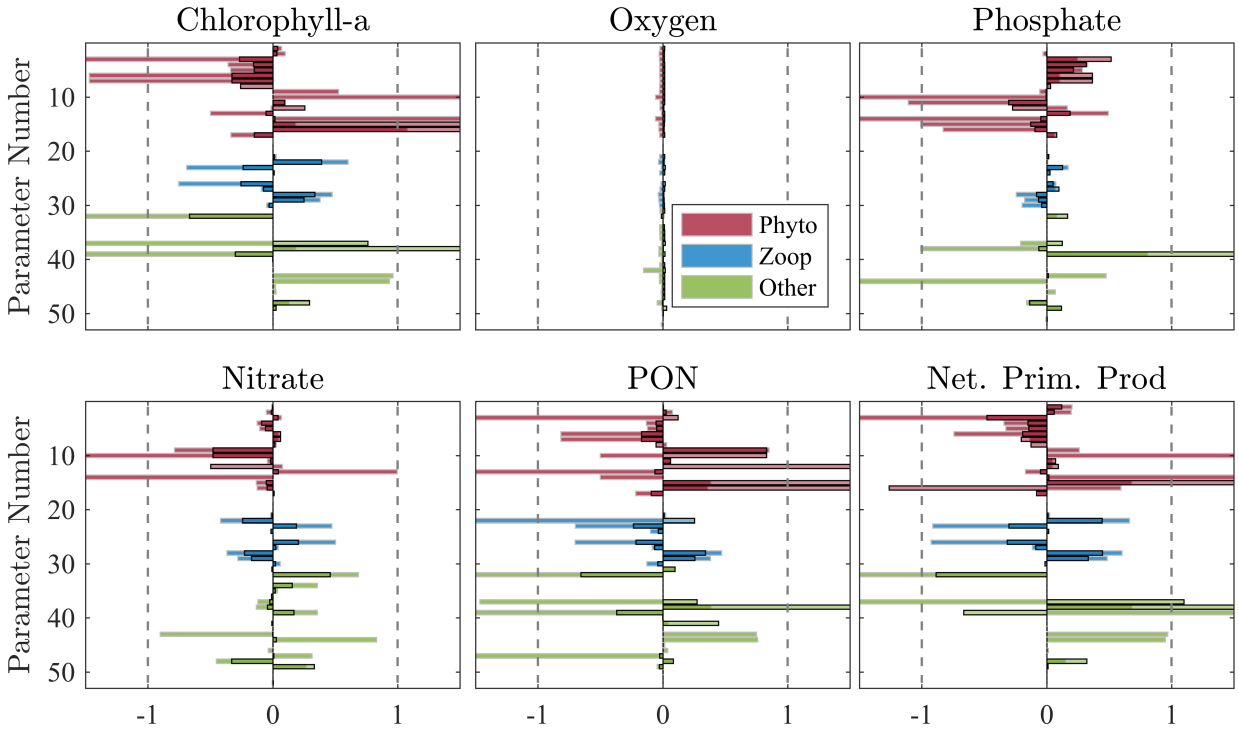

From Figure 4.6, 17 sensitive and mildly sensitive parameters can be identified; 10 phytoplankton parameters, 3 zooplankton parameter, and 4 other parameters. These parameters are denoted by an asterisk in parenthesis in Table 4.4. It should be noted that perturbations to parameters were kept within reasonable bounds, so it is possible, if perturbed well outside of these bounds, many of the relatively insensitive parameter might become sensitive due to non-linear effects. As such, these sensitivities are only valid within the parameter range explored in this study. In order to reduce the number of parameters for optimization, only these 17 parameters were used with the assumption that optimization over parameters that the model is insensitive to is not likely to improve results [159].

4.6 Optimization

As was previously stated, prescribing values to biological parameters can be difficult. As such we have chosen to employ an optimization algorithm to determine the 17 parameters the model was most sensitive to. An open-source optimization package, Dakota from Sandia National Laboratories [184], was used to perform the optimization. Since the initial results obtained with the model were in decent agreement with the BATS field data, it was assumed that the parameters are relatively close to a local minima and therefore local methods could be used instead of global methods, which are much more computationally expensive. A conjugate-gradient method [185] was used. The conjugate gradient method minimizes a given cost function over a space using just the gradient of the function, with no need to compute the Hessian. The optimization was run in parallel with a multi-objective cost function, which was the minimization of the sum of squared residuals

$$f(\mathbf{y}) = \Sigma_{i=1}^{n} \Sigma_{j=1}^{m} \left(\mathbf{y}_{n,m} - \mathbf{y}_{n,m}^{*} \right)^2 \tag{4.61}$$

where $\mathbf{y}$ is a vector of the model learning fields, $\mathbf{y}^*$ is a vector of the target BATS fields, n is the number of months to sum over, and m is the number of vertical levels to sum over. Of the six target BATS fields, only three were used as the optimization learning variables

(chlorophyll, nitrate, and phosphate), while the other three were used as test variables after the model was optimized. Results from the optimization were obtained after 19 objective function evaluations and optimized parameter values are reported in Table 4.4.

4.7 Results

The coupled BFM17-POM1D model was run using the parameter values shown in Table 4.4, which were obtained using both literature values and some expert "tuning", along with the 17 optimized values. The simulation was allowed to run out to steady-state and a multi-year monthly-mean was calculated as a function of depth for (a) chlorophyll, (b) oxygen, (c) nitrate, (d) phosphate, (e) particulate organic nitrogen, and (f) net primary production.

Figure 4.7 qualitatively compares the optimized model results against each of their respective BATS target fields. The model is able to capture the initial spring bloom between January and March brought on by physical entrainment of nutrients, the corresponding peak in net primary production and PON around the same time, and the subsequent subsurface chlorophyll maxima during the summer. While oxygen, nitrate, and phosphate levels are a bit lower than observed values, their overall structures predicted by the model are quite similar to that of the BATS target fields.

To quantitatively evaluate the optimized model, a model skill assessment was performed and is summarized in Figure 4.8 with a Taylor diagram for each target field. A Taylor diagram can be used to assess the extent of misfit between the model and observations by showing the normalized root mean squared (RMS) differences ($\varepsilon_{rms}/\sigma_{obs}$ where ε_{rms} is root mean squared error between the model and the observation fields and σ_{obs} is the standard deviation of the observation field), normalized standard deviation ($\sigma_{mod}/\sigma_{obs}$ where σ_{mod} is the standard deviation of the model field), and correlation coefficient between each of the model output and the BATS target fields. Each of these give an indication of the relative similarities in amplitude, variations in amplitude, and structure of each field compared to

Figure 4.7: Comparison of target BATS fields (top row) to optimized simulation results (bottom row) for (a) chlorophyll (mg Chl-a/m^3), (b) oxygen (mmol O/m^3), (c) nitrate (mmol N/m^3), (d) phosphate (mmol P/m^3), (e) particulate organic nitrogen (PON - mg N/m^3), (f) and net primary production (NPP - mg C/m^3/day).

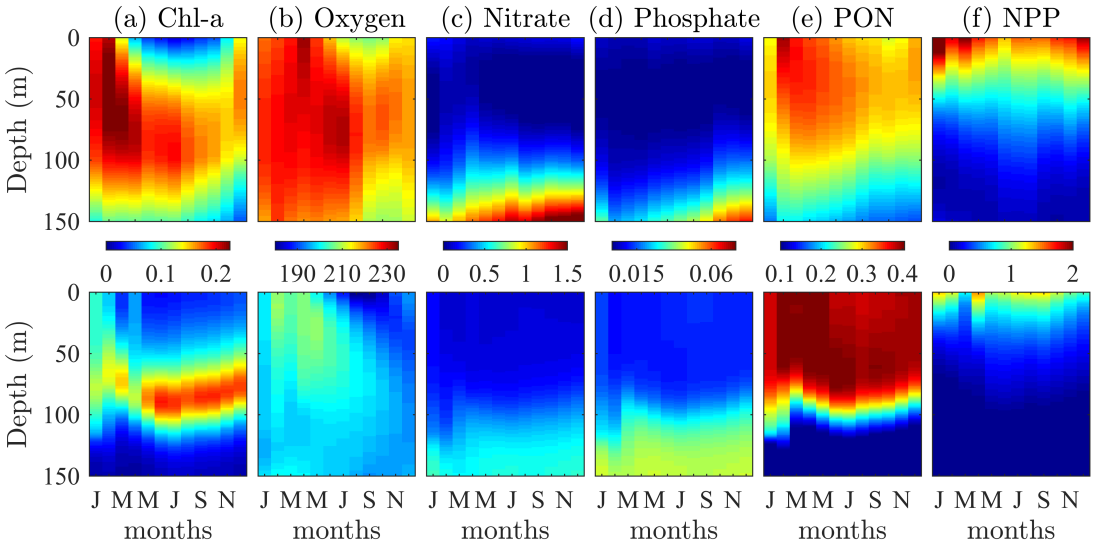

Figure 4.8: Taylor diagram showing the normalized standard deviation, correlation coefficient, and normalized root mean squared differences between the model output and the BATS target fields. Observations lie at (1,0). Radial deviations from observations corresponds to the normalized root mean squared difference, radial deviation from the origin correspond to the normalized standard deviation, and angular deviations from the vertical axis correspond to the correlation coefficient.

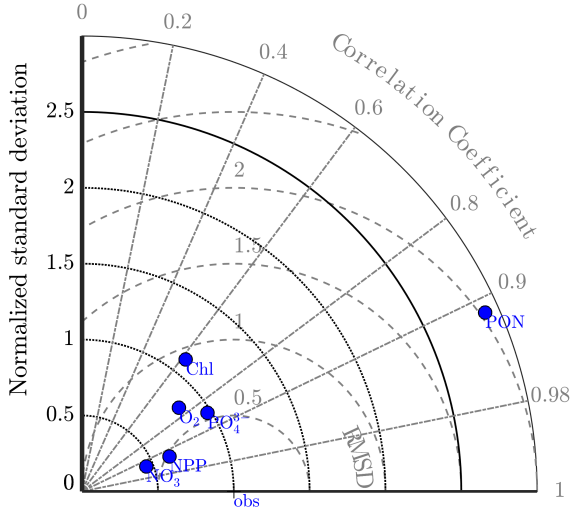

the BATS target fields, respectively. From the Taylor diagram, we can see that for all fields except for PON, errors in the amplitudes are within one standard deviation of the observations. Additionally, the structure of the model fields have high correlations with that of the BATS target fields, ranging from 0.62 for chlorophyll to 0.92 for Nitrate and NPP. The variability in amplitude for chlorophyll, phosphate, and oxygen are all approximately that of the corresponding BATS target fields, while the nitrate and NPP have a lack of variability and PON an excess of variability.

Table 4.1 compares the optimized model results using correlation coefficients and RMS errors to several other reduced-order models. A comparison is only made to those models which were calibrated with the same BATS area data (and employed some kind of parameter estimation technique), forced with a similar one-dimensional physical model, and which reported correlation and RMS errors. Ayata et al. (2013) contained six biological tracers, while both Fasham et al. (1990) and Spitz et al. (2001) contained seven. The Spitz et al. (2001) study, used data assimilation, while the Ayata et al. (2013) and Fasham et al. (1990) studies used only optimization to determine a select set of parameters. On average, the optimized BFM17 does much better than the Ayata et al. (2013) and Fasham et al. (1990) studies when it comes to correlation and RMS error and is on par with the Spitz et al. (2001) study, which used data assimilation and is therefore naturally more likely to perform better. These results show that with a relatively small increase in the number of biological tracers, which allows for phosphate tracking and variable intra- and extra-cellular

Table 4.1: Correlation coefficients (and RMS error in parenthesis) between BATS target fields and several example reduced-order models.

Variable	**BFM17-POM1D**	**Fasham (1990)**	**Ayata (2013)**	**Spitz (2001)**
Chlorophyll	0.62 (0.04)	-0.33 (0.34)	0.60 (0.06)	0.86 (0.04)
Oxygen	0.76 (3.77)	-	-	-
Nitrate	0.92 (0.23)	0.87 (0.28)	0.80 (0.33)	0.98 (0.05)
Phosphate	0.86 (0.007)	-	-	-
PON	0.91 (0.10)	0.48 (0.6)	0.45 (0.08)	0.76 (0.12)
NPP	0.92 (0.24)	-0.47 (0.021)	0.50 (0.14)	0.69 (0.016)

nutrient ratios, BFM17 is able to increase correlation coefficient values and decrease RMS error values for each target field in comparison to similar models.

4.8 Conclusions

In this study, we present a new reduced-order BGC model that is complex enough to accurately capture open-ocean ecosystem dynamics within the Sargasso Sea region, yet reduced enough to integrate within a physical model without substantial additional computational cost. It expands upon more reduced BGC models by incorporating a phosphate equation, as well as the ability to track variable intra- and extra-cellular nutrient ratios. In order to calibrate and test the model, it was coupled to the one-dimensional Princeton Ocean Model and forced using field data from the Bermuda Atlantic test site area. A sensitivity study was performed in order to assess which parameters the model was most sensitive to and were most beneficial to optimize over. Of the 52 parameters within the model, 17 parameters were identified as most sensitive, making them ideal for optimization. An open-source optimization package was used to run a gradient-base parameter optimization on the 17 parameters, where a multi-objective cost function made up of the sum of squared residuals between three (of six) target BATS observation biology fields (chlorophyll, nitrate, and phosphate) and the corresponding model output field. Results using the optimized base parameter values are compared to all six of the BATS target fields (chlorophyll, oxygen, nitrate, phosphate, PON, and NPP) and a model skill assessment was performed, concluding that the optimized BFM17 does well at reproducing observations. In comparison to similar studies with models of slightly less complexity, BFM17-POM1D in is able to perform on par with or better than those studies.

Table 4.2: List of reference state variables for the BFM17 pelagic model. LO = Living Organic, NO = Non-Living Organic, IO = Inorganic.

	Symbol	Code	Type	Units	Description
1	P_c	P2c	LO	mg C m^{-3}	Pico Phytoplankton Carbon
2	P_n	P2n	LO	mmol N m^{-3}	Pico Phytoplankton Nitrogen
3	P_p	P2p	LO	mmol P m^{-3}	Pico Phytoplankton Phosphate
4	P_l	P2l	LO	mg Chl-*a* m^{-3}	Pico Phytoplankton Chlorophyll
5	Z_c	Z4c	LO	mg C m^{-3}	Microzooplankton Carbon
6	Z_n	Z4n	LO	mmol N m^{-3}	Microzooplankton Nitrogen
7	Z_p	Z4p	LO	mmol P m^{-3}	Microzooplankton Phosphate
8	$R_c^{(1)}$	R1c	NO	mg C m^{-3}	Labile Disolved Organic Carbon
9	$R_n^{(1)}$	R1n	NO	mmol N m^{-3}	Labile Disolved Organic Nitrogen
10	$R_p^{(1)}$	R1p	NO	mmol P m^{-3}	Labile Disolved Organic Phosphate
11	$R_c^{(6)}$	R6c	NO	mg C m^{-3}	Particulate Organic Carbon
12	$R_n^{(6)}$	R6n	NO	mmol N m^{-3}	Particulate Organic Nitrogen
13	$R_p^{(6)}$	R6p	NO	mmol P m^{-3}	Particulate Organic Phosphate
14	O	O2o	IO	mg O_2 m^{-3}	Inorganic Dissolved Oxygen
15	$N^{(1)}$	N1p	IO	mmol P m^{-3}	Inorganic Phosphate
16	$N^{(3)}$	N3n	IO	mmol N m^{-3}	Inorganic Nitrate
17	$N^{(4)}$	N4n	IO	mmol N m^{-3}	Inorganic Ammonium

Table 4.3: List of all the abbreviations used to inidicate the physiological and ecological processes in the equations.

Abbreviation	Process
gpp	Gross primary production
rsp	Respiration
prd	Predation
rel	Biological release: egestion, excretion, mortality
exu	Exudation
lys	Lysis
syn	Biochemical synthesis
nit/denit	Nitrification, denitrification

Table 4.4: Phytoplankto parameters within the BFM17 pelagic model.

	Symbol	Code	Base Value	Unit	Description
1	Q_{10_P}	p_q10	2.00	-	Characteristic Q10 coefficient
2	r_{0_P}	p_sum	1.60	d^{-1}	Maximum specific photosynthetic rate
3	$b_P(*)$	p_srs	0.05	d^{-1}	Basal specific respiration rate
4	d_{0_P}	p_sdmo	0.05	d^{-1}	Maximum specific nutrient-stress lysis rate
5	$h_P^{n,p}$	p_thdo	0.10	-	Nutrient stress threshold
6	$\beta_P(*)$	p_pu_ea	0.05	-	Excreted fraction of primary production
7	$\gamma_P(*)$	p_pu_ra	0.05	-	Activity respiration fraction
8	a_4	p_qun	0.025	m^3 (mg C)$^{-1}$ d^{-1}	Specific affinity constant for N
9	h_P^n	p_lN4	1.00	mmol N-NH4 m^{-3}	Half saturation constant for ammonium uptake
10	n_P^{min}	p_qnlc	6.87e-3	mmolN (mg C)$^{-1}$	Minimum nitrogen quota
11	$n_P^{opt}(*)$	p_qnRc	1.26e-2	mmolN (mg C)$^{-1}$	Optimal nitrogen quota
12	$n_P^{max}(*)$	p_xqn*p_qnRc	2.5*n_P^{opt}	mmolN (mg C)$^{-1}$	Maximum nitrogen quota
13	$a_1(*)$	p_qup	2.5e-3	m^3 (mg C)$^{-1}$ d^{-1}	Specific affinity constant for P
14	p_P^{min}	p_qplc	4.29e-4	mmolP (mg C)$^{-1}$	Minimum phosphorus quota
15	$p_P^{opt}(*)$	p_qpRc	7.86e-4	mmolP (mg C)$^{-1}$	Optimal phosphorus quota
16	$p_P^{max}(*)$	p_xqp*p_qpRc	2*p_P^{opt}	mmolP (mg C)$^{-1}$	Maximum phosphorus quota
17	$\alpha_{chl}^0(*)$	p_alpha_chl	1.52e-5	mgC (mg chl)$^{-1}$ (μE)$^{-1}$ m^2	Maximum light utilization coefficient
18	$\theta_{chl}^0(*)$	p_qchlc	0.016	mg chl (mg C)$^{-1}$	Maximum chl:C quotum
19	c_P	p_epsChla	0.03	m^2 (mg chl)$^{-1}$	Chl-specific light absorption coefficient

Table 4.5: Same as Table 4.4, but for zooplankton parameters.

	Symbol	Code	Base Value	Unit	Description
20	Q_{10_Z}	p_q10	2.00	-	Characteristic Q10 coefficient
21	b_Z	p_srs	0.02	d^{-1}	Basal specific respiration rate
22	$r_{0_Z}(*)$	p_sum	2.00	d^{-1}	Potential specific growth rate
23	d_Z^O	p_sdo	0.25	m^3 (mg C)$^{-1}$ d^{-1}	Density-dependent specific mortality rate
24	d_{0_Z}	p_sd	0.00	d^{-1}	Specific mortality rate
25	$\eta_Z(*)$	p_pu	0.50	-	Assimilation efficiency
26	β_Z	p_pu_ea	0.25	-	Fraction of activity excretion
27	ε_Z^c	p_pe_R1c	0.60	-	Partition between dissolved and particulate excretion of C
28	ε_Z^n	p_pe_R1n	0.72	-	Partition between dissolved and particulate excretion of N
29	ε_Z^p	p_pe_R1p	0.832	-	Partition between dissolved and particulate excretion of P
30	h_Z^F	p_chuc	200	mgC m^{-3}	Half-saturation food concentration for Type II
31	μ_Z	p_minfood	50.0	mgC m^{-3}	Half-saturation food concentration for preference factor
32	n_Z^{opt}	p_qncMIZ	1.26e-2	mmolN (mg C)$^{-1}$	Maximum nitrogen quota
33	p_Z^{opt}	p_qpcMIZ	7.86e-4	mmolP (mg C)$^{-1}$	Maximum phosphorous quota
34	$\delta_{Z,P}(*)$	p_paPPY	1.00	-	Availability of phytoplankton P to zooplankton Z
35	$\delta_{Z,Z}$	p_paMIZ	0.00	-	Availability of zooplankton Z to zooplankton Z

Table 4.6: Same as Table 4.4, but for all other parameters.

	Symbol	Code	Base Value	Unit	Description
36	Λ_{N4}^{nit}	p_sN4N3	0.01	d^{-1}	Specific nitrification rate at 10C
37	Q_{10_N}	p_q10N4N3	2.00	-	Q10 factor for nitrification/denitrification reaction
38	h_o	p_clO2o	10.0	$mmolO_2\ m^{-3}$	Half saturation for chemical processes
39	T^*	BASETEMP	15.0	°C	Base temperature for Q10
40	$\varepsilon_{PAR}(*)$	p_PAR	0.40	-	Fraction of Photosynthetically Available Radiation
41	$\lambda_w(*)$	p_eps0	0.0435	m^{-1}	Background attenuation coefficient
42	$c_{R(6)}$	p_epsR6	0.1e-3	$m^2\ (mg\ C)^{-1}$	C-specific attenuation coefficient of particulate detritus
43	$v_{R(6)}^{sed}$	sediR6	1.00	$m\ d^{-1}$	Settling velocity of particulate detritus
44	$\alpha_{R(1))}^{O(3)}$	p_sR1O3	0.05	d^{-1}	Specific remineralization rate of dissolved oxygen
45	$\alpha_{R(1))}^{N(1)}(*)$	p_sR1N1	0.05	d^{-1}	Specific remineralization rate of dissolved nitrogen
46	$\alpha_{R(1))}^{N(4)}(*)$	p_sR1N4	0.05	d^{-1}	Specific remineralization rate of dissolved ammonium
47	$\alpha_{R(6))}^{O(3)}$	p_sR6O3	0.50	d^{-1}	Specific remineralization rate of particulate oxygen
48	$\alpha_{R(6))}^{N(1)}$	p_sR6N1	0.50	d^{-1}	Specific remineralization rate of particulate nitrogen
49	$\alpha_{R(6))}^{N(2)}$	p_sR6N4	0.50	d^{-1}	Specific remineralization rate of particulate ammonium
50	W	WGEN	-0.02 - 0	$m\ s^{-1}$	Imposed general circulation vertical velocity
51	W_E	WEDDY	0 - 0.1	$m\ d^{-1}$	Imposed mesoscale circulation vertical velocity
52	$\lambda_{[O2o]}$	NRT_o2o	1.00	$m\ d^{-1}$	Relaxation constant for oxygen at bottom
53	$\lambda_{[N1p]}$	NRT_n1p	1.00	$m\ d^{-1}$	Relaxation constant for phosphate at bottom
54	$\lambda_{[N3n]}$	NRT_n3n	1.00	$m\ d^{-1}$	Relaxation constant for nitrogen at bottom
55	$\kappa_{[N4n]}$	NRT_n4n	1.00	$m^2\ s^{-1}$	Relaxation constant for ammonium at bottom
56	D_{BFM}	UMOLBFM	1e-4	$m^2\ s^{-1}$	Background diffusion for BFM tracers

Chapter 5

Conclusions and Future Research

5.1 Conclusions

This dissertation explored the effects of upper-ocean turbulence, from kilometer to meter scales, including submesocale and small-scale wind- and wave-driven turbulent processes, on both non-reactive and biogeochemically reactive tracers. While these scales remain subgrid scale in almost all ESMs, and so are often not explicitly represented, the effects of tracer-turbulence coupling can have large effects on the global climate cycle. In particular, couplings at submeoscales and below have the potential to have the greatest impact, as knowledge gained from research on reacting flows in other contexts suggests that the most significant tracer-flow couplings occur when the dominant physical processes have time scales on the order of the tracer reactive time scale. While basin-scale and mesoscale processes are generally much slower than most biological processes, submesoscale and small-scale processes have time scales of the same order as many important biogeochemical reaction processes. It is thus worth while to explore these couplings, from a relatively fundamental approach first in order to gain a better understanding of their effects. The common thread throughout this work is exploring these subgrid scale tracer-turbulence time couplings through the use of high-fidelity large eddy simulations of relatively idealized physical set-ups (i.e. no topography, a flat and regular surface, etc.), but with realistic turbulence and biogeochemical tracer dynamics.

5.1.1 Effects of Submesoscale Turbulence on Ocean Tracers

The second chapter of this dissertation explored the effects of multi-scale turbulence on non-reactive tracers spanning a spacial scale range of 20 km down to 5 m. The simulations included the effects of both wave-driven Langmuir turbulence and submesocale eddies, and explored the evolution and distribution of tracers with different initial and boundary conditions. This study serves to provide a baseline fundamental understanding of multi-scale tracer-turbulence coupling. Two different flow regimes were examined, a Langmuir-only (LO) region, which contained only small-scale, three-dimensional wind- and wave- driven boundary layer turbulence, and a submesocale-eddy (SE) region, which contained the small-scale turbulence of the LO region, but also larger submesoscale processes. Tracer properties were found to be highly dependent on on the relative strengths of restratifcation by submesoscale eddies and vertical mixing by Langmuir turbulence and these dependencies were shown to have an effect on the effective vertical eddy diffusivity, a quantity often used to parameterize small scale tracer transport. Tracer released at different initial depths were shown to be transported differently (both spatially and temporally) based upon the turbulence regime and the depth at which it was released. Tracers with varying rates of air-sea flux showed vertical mixing that was dependent on the ratio of characteristic time scaled associated with the flux rate and the dominant near-surface mixing process. A multi-scale analysis showed that tracer vertical transport was achieved by small-scale processes only in the LO region, while in the SE region, transport is achieved by both small and large-scale processes. Results from this chapter, such as dependencies of tracer transport on the vertical structure of the mixed layer and the physical processes that create that structure, can be used in the development of reduced-order modeling of tracer dynamics and serve as a baseline knowledge for similar studies using reactive tracers.

5.1.2 Effects of Langmuir Turbulence on Upper Ocean Carbonate Chemistry

The third chapter of this dissertation explored the effects of wave-driven Langmuir turbulence on carbonate chemistry by varying strength of Langmuir turbulence and using several different carbonate chemistry models. Langmuir turbulence and carbonate chemistry have time scales of the same order as each other, and thus have potentially strong tracer-flow coupling. This study served to examine these couplings and their importance within the larger global carbon cycle. Physical scenarios were the same for all simulations except for the applied strength of Langmuir turbulence, which was varied from no-Langmuir up to a Langmuir number of 0.2 over four different simulations sets. Three different chemistry models were also used: (*i*) an infinitely slow non-reactive model, (*ii*) a time-dependent model, and (*iii*) a infinitely fast equilibrium model. Results showed that the presence of Langmuir turbulence increased the flux rate of CO_2 from the atmosphere to the ocean by continually flushing out the surface layer of the domain, which results in a greater air-sea gradient in CO_2 and faster flux rates. As the strength of Langmuir turbulence was increased, the increase in flux rate also increased. Results also showed that the choice of carbonate chemistry model had an affect on the flux rate of CO_2, with the infinitely fast equilibrium chemistry increasing the flux rate the most by, again, maintaining a lower concentration of CO_2 at the surface through quickly converting CO_2 into bicarbonate and carbonate, and the infinitely slow non-reactive chemistry increased it by the least. The combination of both Langmuir turbulence and different carbonate chemistry models revealed that the two affects are not simply additive as the presence of Langmuir turbulence and its increase in strength did not have the same affect on each chemistry model. As such, results from this study have implications for the development of reduced-order model, in that not only are both of these processes important to consider for basin-scale air-sea flux rates of CO_2, but that their coupling is non-trivial.

5.1.3 Development and Testing of a Reduced Order Biogeochemical Model

The fourth chapter of this dissertation details the development of a reduced-order biogeochemical model called BFM17. The need for such a model is motivated by the first chapter in this work, primarily the need for a biogeochemical model that is relatively accurate enough to reproduce real upper ocean ecological dynamics, but that can also be integrated within a high-resolution LES, similar to that in the second chapter, at a reasonable computational cost. The development of such a model facilitates a wide range of studies examining the effects of submesoscale and small-scale dynamics on biological processes important to the global climate cycle, such as the draw down of carbon by phytoplankton and the export of carbon from the surface ocean. Within this chapter, the new reduced-order model is introduced, coupled to a one-dimensional physical model in order to perform a parameter sensitivity study, and then calibrated using open-ocean observational data from the BATS field site. Initial results from the model show good agreement with the BATS data in comparison to models of slightly lesser complexity, demonstrating that with a small increase in complexity and the inclusion of several key processes, the ability for BFM17 to capture open-ocean ecological dynamics increases greatly. Details of an ongoing parameter optimization are presented, including the process of choosing the 17 parameters to optimize over and the numerical techniques used to perform the optimization. Results from the optimized BFM17 are expected to exceed that of the unoptimized model and produce even better agreement with the BATS field data.

5.2 Future Work

5.2.1 Developing a Reduced Order Biogeochemical Model

While the BFM17 model has been calibrated and is currently being optimized using the BATS field data, future research could extend BFM17 calibration to include data from other field sites with different dominant ecological dynamics than that of BATS. This inclusion of

additional field data will help to make results from studies using BFM17 more applicable to the global ocean, as well as make BFM17 more applicable to studies in specific biological regions. In order to do so, similar data to that from the BATS site (i.e. climatological temperature, salinity, wind, PAR, and various biological variables) should be collected and prepared in the same fashion. Incorporating the data into the optimization would be fairly straightforward and involve a simple addition of new cost functions to the multi-objective cost function that it already being used. Data sites that are potential candidates for this additional calibration include the Hawaii Ocean Time-Series (HOTS), the North Atlantic Bloom Experiment (NABE), and the Ocean Weather Ship Station India (OWSI) sites.

5.2.2 Langmuir Turbulence and Carbonate Chemsitry

While a clear connection has been drawn between Langmuir turbulence and its ability to enhance the amount of CO_2 brought into the domain, further exploration into an expanded time and parameter space is warranted before such effects can be incorporated into a sub-grid scale model for use in ESMs. The work done within this thesis explored shorter, transient processes, but longer, steady-state results are needed. The development of a reduced-order, yet still time-dependent carbonate chemistry model would help facilitate this research, allowing for longer-time processes to be explored with a reasonable computational cost. Additionally, this extended-time study could explore effects of diurnal cycle heating and cooling, as well as non-constant wind-driven shear and wave-driven Langmuir turbulence.

Aside from the development and use of a reduced-order model for exploring longer times, a series of shorter time studies could be explored. One possibility is exploring the effects of temperature changes within the mixed layer on CO_2 flux and carbonate chemistry reaction rates due to Langmuir turbulence deepening the mixed layer and subsequently entraining cooler water from below, as well as mixing in warmer or cooler waters from above due to radiative heating/cooling and precipitation at the surface. Various degrees of strat-

ification below the mixed layer, initial temperature profiles, and surface heat forcing could be used to explore this. These studies could also incorporate buoyancy driven turbulence and explore how that can combine with Langmuir and shear-driven turbulence. The carbonate chemistry study within this thesis maintained a constant salinity profile throughout the course of the simulations, and while salinity has a lesser affect on the solubility of CO_2 and reaction rates of carbonate chemistry, its affect could still be explored, both isolated from and in combination with temperature affects.

5.2.3 Multi-Scale Turbulence and Biogeochemsitry

Now that a new reduced-order BFM17 model has been developed and calibrated, the possibilities for its use are quite broad. Of particular interest is exploring a similar multi-scale turbulence set-up as the study done in the first chapter of this thesis, but replacing the non-reactive idealized tracers with the 17 relatively realistic biogeochemically reactive tracers within BFM17 in order to explore tracer-turbulence coupling effects between submesoscale processes and biological tracers and what affect small-scale turbulence has on that coupling. A set of three main physical simulations could be performed to produce a well rounded study: (*i*) a lower resolution ($\sim$ 1 km) simulation, where only submesoscale processes are resolved, (*ii*) a higher resolution (¡ $\sim$ 10 m) simulation, where both submesoscale and small-scale processes are resolved, but the small-scale processes are purely due to wind-driven shear turbulence, and (*iii*) the same high resolution simulation, but with both wind-driven shear and wave-driven Langmuir turbulence. Each of the simulations would incorporate BFM17 as the biogeochemical model and be initialized in the same way. Since the multi-scale turbulence simulations can only be run out to maximum of 15-20 days before the submesoscale eddies begin to break down, initialization of the simulations should be done carefully. In order to determine the appropriate initialization of both the physical and the BFM17 tracer set-ups, an initial suite of simulations could be done. Using a courser resolution simulation set-up similar to that of the main simulations, a large set of varying

initial and boundary conditions for both physical and tracer variables could be explored in a relatively cost effective way. As a first step, BFM17 tracer profiles could be initialized in a horizontally uniform way using depth profiles from different months within the BMF17-POM optimization results. This would help determine what initial conditions would lead to events that are relevant to submesoscale processes, such as entrainment of nutrients due to mixed layer deepening, phytoplankton bloom timing, intensity, patchiness, and subduction, and carbon export from the surface ocean. Aside from determining an appropriate set of initial and boundary conditions for the main simulations, these course resolution simulations could be compiled to form an interesting study in itself, which would be able to explore a much larger parameter space than the higher resolution simulations. Results from these simulations could be compared to other similar course resolution submesoscale simulations that used much simpler biological models than BFM17 such as [9, 57, 186]

Bibliography

[1] B. Fox-Kemper, R. Ferrari, and R. W. Hallberg. Parameterizations of mixed layer eddies. part i: Theory and diagnosis. Journal of Physical Oceanography, 38:1145–1165, 2008.

[2] Richard E. Zeebe and Dieter A. Wolf-Gladrow. Co2 in seawater: Equilibrium, kinetics, isotopes. Gulf Professional Publishing, 65, 2001.

[3] A. G. Dickson and C. Goyet, editors. Handbook of Methods for the Analysis of the Various Parameters of the Carbon Dioxide System in Sea Water. DOE, 2 edition, 1994.

[4] P. E. Hamlington, L. P. Van Roekel, B. Fox-Kemper, K. Julien, and G. P. Chini. Langmuir-submesoscale interactions: Descriptive analysis of multiscale frontal spin-down simulations. Journal of Physical Oceanography, 44:2249–2272, 2014.

[5] Geoffrey K. Vallis. Atmospheric and Oceanic Fluid Dyanmics - Fundementals and Large-Scale Circulation. Cambridge University Press., 2006.

[6] A. Mahadevan and D. Archer. Modeling the impact of fronts and mesoscale circulation on the nutrient supply and biogeochemistry modeling the impact of fronts and mesoscale circulation on the nutrient supply and biogeochemistry of the upper ocean. Journal of Geophysical Research, 105:1209–1225, 2000.

[7] D. Bianchi, M. Zavatarelli, N. Pinardi, R. Capozzi, L. Capotondi, C. Corselli, and S. Masina. Simulations of ecosystem response during the spropel s1 deposition event. Paleogeography, Palaeoclimatology, Palaeoecology, 235:265–287, 2005.

[8] Ian S. Robinson. Measuring the Oceans from Space: The principles and methods of satellite oceanography. Springer, 2004.

[9] L. N. Thomas, A. Tandon, and A. Mahadevan. Submesoscale processes and dynamics. Ocean Modeling in an Eddying Regime - AGU Geophysical Monograph Series, 177:17–38, 2008.

[10] B. J. Hoskins and F. P. Bretherton. Atmospheric frontogenesis models: Mathematical formulation and solution. Journal of Atmospheric Science, 29:11–37, 1972.

[11] R. Pollard and L. Regier. Large variations in potential vorticity at small spatial scales in the upper ocean. Nature, 348:227–229, 1990.

[12] D. L. Rudnick. Intensive surveys of the azores front. part ii: Inferring the geostrophic and vertical velocity fields. Journal of Geophysical Research, 101:16,291–16,303, 1996.

[13] R. K. Sherman, J. A. Barth, and P. M. Kosro. Diagnosis of three-dimensional circulation associated with mesoscale motion in the california current. Journal of Physical Oceanography, 29:651–670, 1999.

[14] R. Bleck, R. Onken, and J. Woods. A two-dimensional model of mesoscale frontogenesis in the ocean. Q. J. R. Meteorol. Soc., 114:347–371, 1988.

[15] M. A. Spall. Frontogenisis, subduction, and cross-front exchange at upper ocean fronts. Journal of Geophysical Research, 100:2543–2557, 1995.

[16] A. Mahadevan. The impact of submesoscale physics on primary productivity of plankton. Annual Review of Marine Science, 8:161–186, 2016.

[17] X. Capet, J. C. McWilliams, M. J. Molemaker, and A. F. Shchepetkin. Mesoscale to submesoscale transition in the california current system. part ii: Frontal processes. Journal of Physical Oceanography, 38:44–64, 2007.

[18] G. Boccaletti, R. Ferrari, and B. Fox-Kemper. Mixed layer instabilities and restratification. Journal of Physical Oceanography, 37:2228–2250, 2007.

[19] D. A. Bennetts and B. J. Hoskins. Conditional symmetric instability - a possible explanation for frontal rainbands. Q. J. R. Meteorol. Soc., 105(446):945–962, 1979.

[20] L. N. Thomas and C. M. Lee. Intensification of ocean fronts by down-front winds. Journal of Physical Oceanography, 35:1086–1102, 2005.

[21] J. R. Taylor and R. Ferrari. Buoyancy and wind-driven convection at mixed layer density fronts. Journal of Physical Oceanography, 40:1222–1242, 2010.

[22] L. N. Thomas and J. R. Taylor. Reduction of the usable wind-work on the general circulation by forced symmetric instabilities. Geophysical Research Letters, 37, 2010.

[23] L. N. Thomas, J. R. Taylor, R. Ferrari, and T. M. Joyce. Symmetric instability in the gulf stream. Deep-Sea Research II, 91:96–110, 2013.

[24] P. P. Sullivan and J. C. McWilliams. Dynamics of winds and currents coupled to surface waves. Annual Review of Fluid Mechanics, 42:19–42, 2010.

[25] I. Langmuir. Surface motion of water induced by wind. Science, 97:119–123, 1938.

[26] A. E. Tejada-Martinez, I. Akkerman, and Y. Bazilevs. Large-eddy simulation of shallow water langmuir turbulence using isogeometric analysis and the residual-based variational multiscale method, 2012.

[27] A. D. D. Craik and S. Leibovich. A rational model for langmuir turbulence. Journal of Fluid Mechanics, 73:401–426, 1976.

[28] I. Gjaja and D. D. Holms. elf-consistent hamiltonian dynamics of wave mean-flow interaction for a rotating stratified incompressible fluid. Physica D, 98:343–1887, 1996.

[29] D. D. Holm. The ideal craik-leibovich equations. Physica D, 98:415–441, 1996.

[30] J. C. McWilliams, J. M. Restrepo, and E. Lane. An asymptotic theory for the interaction of waves and currents in coastal waters. Journal of Fluid Mechanics, 511:135–178, 2004.

[31] N. Suzuki and B. Fox-Kemper. Understanding stokes forces in the wave-averaged equations. 2015.

[32] Sabine. The oceanic sink for anthropogenic co2. Science, 305:367–371, 2004.

[33] S. Khatiwala and. Global ocean storage of anthropogenic carbon. Biogeosciences, 10(4):2169–2191, 2013.

[34] S. C. Bates, B. Fox-Kemper, S. R. Jayne, W. G. Large, S. Stevenson, and S. G. Yeager. Mean biases, variability, and trends in air-sea fluxes and sst in the ccsm4. Journal of Climate, 2012.

[35] A. J. Watson and J. C. Orr. Carbon dioxcide fluxes in the global ocean. Springer2003, 2003.

[36] V. Strass. Chlorophyll patchiness caused by mesoscale upwelling at fronts. Oceanographic Research Papers, 39:75–96, 1992.

[37] James A. Yoder, James Aiken, Robert N. Swift, Frank E. Hoge, and Petra M. Stegmann. Spatial variability in near-surface chlorophyll a fluorescence measured by the airbornw oceanographic lidar (aol). Deep-Sea Research II, 40:37–53, 1992.

[38] D. J. McGillicuddy Jr., V. K. Kosnyrev, J. P. Ryan, and J. A. Yoder. Covariation of mesoscale ocean color and sea-surface temperature patterns in the sargasso sea. Deep-Sea Research II, 48:1823–1836, 2001.

[39] J. F. R. Gower, K. L. Denman, and R. J. Holyer. Phytoplankton patchiness indicates teh fluctuation spectraum of mesoscale oceanic structure. Nature, 288:157–159, 1980.

[40] Kenneth L Denman and Mark R. Abbott. Time scales of pattern evolution from cross-spectrum analysis of advanced very high resolution radiometer and coastal zone color scanner imagery. Journal of Geophysical Research, 99(C4):7433–7442, 1994.

[41] P. G. Strutton, N. S. Lovenduski, M. Mongin, and R. Metear. Quantification of southern ocean phytoplankton biomass and primary productiity via satellite observations and biogeochemical models. CCAMLR Science, 19:247–265, 2012.

[42] Sophie Anne Clayton. Physical Influences on Phytoplankton Ecology: Models and Observations. PhD thesis, Massachusetts Institute of Technology, June 2013.

[43] E. R. Abraham. The generation of plankton patchiness by turbulent stirring. Nature, 391:577–580, 1998.

[44] M. A. Bees. Plankton communities and choatic advection in dynamical models of langmuir circulation. Applied Scientific Research, 59:141–158, 1998.

[45] A. Mahadevan and J. W. Campbell. Biogeochemical patchiness at the sea surface. Geophysical Research Letters, 29(19):32–1–32–4, October 2002.

[46] Marina Levy and Patrice Klein. Does the low frequency variability of mesoscale dynamics explain a part of the phytoplankton and zooplankton spectral variability? Proc. R. Soc. Lond., 460:1673–1687, 2015.

[47] Thomas M Powell and Akira Okubo. Turbulence, diffusion and patchiness in the sea. Phil. Trans. R. Soc. Lond., 343:11–18, 1994.

[48] Adrian P. Martin, Kelvin J. Richards, Annalisa Bracco, and Antonello Provenzale. Patchy productivity in the open ocean. Global Biogeochem Cycles, 16(2):1025, 2002.

[49] A. Mahadevan. Speatial heterogeneity and its relation to processes in the upper ocean, pages 165–182. Springer-Verlag, 2005.

[50] A. Tzella and P. H. Haynes. Small-scale spatial structure in plankton distributions. Biogeosciences, 4(2):173–179, 2007.

[51] W. Smyth. Dissipation-range geometry and scalar spectra in sheared stratified turbulence. Journal of Fluid Mechanics, 401:209–242, 1999.

[52] D. M. Lewis. A simple model of plankton population dynamics coupled with a les of the surface mixed layer. Journal of Theoretical Biology, 234:565–591, 2005.

[53] S. Haney, B. Fox-Kemper, and K. Julien. Symmetric and geostrophic instabilities in the wave-forced ocean mixed layer. Journal of Physical Oceanography, page Submitted, 2015.

[54] J. C. McWilliams, J. Gula, M. J. Molemaker, L. Renault, and A. F. Shchepetkin. Filament frontogenesis by boundary layer turbulence. Journal of Physical Oceanography, 45:1988–2005, 2015.

[55] A. Mahadevan and J. W. Campbell. Biogeochemical variability at the sea surface: How it is linked to process response times. In L. Seuront and P. G. Strutton, editors, Handbook of scaling methods in aquatic ecology: Measurments, analysis, simulation, pages 215–227. CRC Press LLC, 2003.

[56] A. Mahadevan, E. D'Asaro, and M. J. Perry. Eddy-driven stratification initiates north atlantic spring phytoplankton blooms. Science, 337:54–58, 2012.

[57] M. Levy, P. Klien, and A. M. Treguier. Impact of sub-mesoscale physics on production and subduction of phytoplankton in an oligotrophic regime. Journal of Marine Research, 59:535–565, 2001.

[58] D. J. McGillicuddy Jr., A. R. Robinson, D. A. Siegel, H. W. Jannascg, R. Johnson, T. D. Dickey, J. McNeil, A. F. Michaels, and A. H. Knap. Influence of mesoscale eddies on new production in the sargasso sea. Nature, (263-266), 394.

[59] M. J. Follows and R. G. Willliams. Physical transport of nutrients and the maintenance of biological production, pages 19–51. Springer, 2003.

[60] M. Omand, M. Perry, E. D'Asaro, C. Lee, N. Briggs, I. Centinic, and A. Mahadevan. Eddy-driven subduction exports particulate organic carbon from the spring bloom. Science, 348(6231):222–225, 2015.

[61] J. A. Smith. Observed growth of langmuir circulation. Journal of Geophysical Research - Oceans, 97:5651–5664, 1992.

[62] A. Tandon and C. Garrett. Mixed layer restratification due to a horizontal density gradient. Journal of Physical Oceanography, 24:1419–1424, 1994.

[63] T. W. N. Haine and J. Marshall. Gravitational, symmetric, and baroclinic instability of the ocean mixed layer. Journal of Physical Oceanography, 28:634–658, 1997.

[64] S. Haney and S. Bachman and. Hurricane wake restratification rates of one-, two- and three-dimensional processes. Journal of Marine Research, 70(6):824–850, 2012.

[65] J. C. McWilliams. A uniformly valid model spanning the regimes of geostrophic and isotropic, stratified turbulence: Balanced turbulence. Journal of Atmospheric Science, 42:1773–1774, 1985.

[66] R. Benzi and D. R. Nelson. Fisher equation with turbulence in one dimension. Physica D: Nonlinear Phenomena, pages 2003–2015, 2009.

[67] S. Pigolotti, R. Benzi, M. H. Jensen, and D. R. Nelson. Population genetics in compressible flows. Physical Review Letters, 108(12):128, 2012.

[68] K. L. Denman. Modelling planktonic ecosystems: parameterizing complexity. Progress in Oceanography, 57:429–452, 2003.

[69] K. M. Smith, P. E. Hamlington, and B. Fox-Kemper. Effects of submesoscale turbulence on ocean tracers. Journal of Geophysical Research: Oceans, 121(1):908–933, 2016.

[70] M. A. Donelan, J. Hamilton, and W. H. Hui. Directional spectra of wind-generated waves. Philosophical Transactions of the Royal Society of London Series A - Mathematical Physical and Engineering Sciences, 315:509–562, 1985.

[71] A. Webb and B. Fox-Kemper. Wave spectral moments and stokes drift estimation. Ocean Modeling, 40:273–288, 2011.

[72] A. Webb and B. Fox-Kemper. Impacts of wave spreading and multidirectional waves on estimating stokes drift. Ocean Modeling, 2015.

[73] J. C. McWilliams, P. P. Sullivan, and C. H. Moeng. Langmuir turbulence in the ocean. Journal of Fluid Mechanics, 334:1–30, March 1997.

[74] L. P. Van Roekel, B. Fox-Kemper, P. P. Sullivan, P. E., and S. R. Haney. The form and orientation of langmuir cells for misaligned winds and waves. Journal of Geophysical Research - Oceans, 117, 2012.

[75] J. C. McWilliams and B. Fox-Kemper. Oceanic wave-balanced surface fronts and filaments. Journal of Fluid Mechanics, 730:464–490, 2013.

[76] C. H. Moeng. A large-eddy-simulation model for the study of planetary boundary-layer turbulence. Journal of Atmospheric Science, 41:2052–2062, 1984.

[77] P. P. SullivanSullivan, J. C. McWilliams, and W. K. Meslville. Surface gravity wave effects in the oceanic boundary layer. Journal of Fluid Mechanics, 593:405–452, 2007.

[78] Peter P. Sullivan, James C. McWilliams, and Chin-Hoh Moeng. A subgrid-scale modeal for large-eddy simulations of planetary boundary-layer flow. Boundary-Layer Meteorology, 71:247–276, 1994.

[79] R. Wanninkhof. Relationship between wind speed and gas exchange over the ocean. Journal of Geophysical Research, 97:7373–7382, 1992.

[80] P. S. Liss and M. T. Johnson, editors. Ocean-Atmosphere Interactions of Gases and Particles. Springer, 2014.

[81] I. Calmet and J. Magnaudet. High-schmidt number mass transfer through turbulent gas-liquid interfaces. International Journal of Heat and Fluir Flow, 19(5):522–532, 1998.

[82] S. Bachman and B. Fox-Kemper. Eddy parameterization challenge suite. i: Eddy spindown. Ocean Modeling, 64:12–28, 2013.

[83] P. Klien and G. Lapeyre. The oceanic vertical pump induced by mesoscale and submesoscale turbulence. Annual Review of Marine Science, 1:351–375, 2009.

[84] T. Radko. Double Diffusive Convection. Cambridge University Press., 2013.

[85] S. Bachman, B. Fox-Kemper, and F. O. Bryan. A tracer-based inversion method for diagnosing eddy-induced diffusivity and advection. Ocean Modeling, 86:1–14, 2013.

[86] B. J. Hoskins. The role of potential vorticity in symmetric stability and instability. Journal of the Royal Meteorological Society, 100(425):480–482, 1974.

[87] Kenneth Ward Church and Patrick Hanks. Word association norms, mutual information, and lexicography. Computational Linguistics, 1(22-29), 16.

[88] Benjamin W. Zeff, Daniel D. Lanterman, Ryan McAllister, Rajarshi Roy, Eric J. Kostelich, and Daniel P. Lathrop. Measuring intense rotation and dissipation in turbulent flows. Nature, 421:146–149, January 2003.

[89] Thomas Boeck, Dmitry Krasnov, and Jorg Schumacher. Statistics of velocity gradients in wall-bounded shear flow turbulence. Physica D, 239(14):1258–1263, 2010.

[90] Peter E. Hamlington, Dmitry Krasnov, Thomas Boeck, and Jorg Schumacher. Statistics of the energy dissipation rate and local enstrophy in turbulent channel flow. Physica D, 241:169–177, 2012.

[91] L. N. Thomas. Destruction of potential vorticity by winds. Journal of Physical Oceanography, 35:2457–2466, 2005.

[92] M. Spall. Baraoclinic jets in confluent flow. Journal of Physical Oceanography, 27:381–402, 1997.

[93] R. Ferrari and D. L. Rudnick. Thermohaline variability in the upper ocean. Journal of Geophysical Research, 105(C7):16857–16883, July 2000.

[94] X. Capet, J. C. McWilliams, M. J. Molemaker, and A. F. Shchepetkin. Mesoscale to submesoscale transition in the california current system. part ii: Frontal processes. Journal of Physical Oceanography, 38:44–64, 2008.

[95] A. Mahadevan and A. Tandon. An analysis of mechanisms for submesoscale vertical motion at ocean fronts. Ocean Modell., 14:241–256, 2006.

[96] H. U. Sverdrup. On conditions for the vernal blooming of phytoplankton. J. Cons. Int. Explor. Mer., 18:287–295, 1953.

[97] Jorge L Sarmiento and Nicolas Gruber. Biogeochemical Dynamics. Princeton Univeristy Press, 2004.

[98] S. F. Barstow. The ecology of langmuir circulation: A review. Marine Environmental Research, 9:211–236, 1982.

[99] T. J. Smayda. Suspension and sinking of phytoplankton in the sea. Oceanogr. Mar. Biol. Ann. Rev., 8:353–414, 1970.

[100] T. M. Powell, P. J. Richerson, T. M. Dillon, B. A. Agee, B. J. Dozier, D. A. Godden, and L. O. Myrup. Spatial scales of current speed and phytoplankton biomass fluctuations in lake tahoe. Science, 189:1088–1090, 1975.

[101] H. Stommel. Trajectories of small bodies sinking slowly through convection cells. Journal of Marine Research, 8:24–29, 1949.

[102] D. M. Lewis. A simple model of plankton population dynamics coupled with a les of the surface mixed layer. Journal of Theoretical Biology, 234:565–591, 2005.

[103] F. Qiao, D. Dai, J. Simpson, and H. Svendsen. Banded structure of drifting macroalgae. Marine Pollution Bulletin, 58:1792–1795, 2009.

[104] S. A. Thorpe. Langmuir circulation and the dispersion of oil spills in shallow seas. Spill Science and Technology Bulletin, 6(3/4):213–223, 2000.

[105] S. A. Thorpe. Spreading of floating particles by langmuir circulation. Marine Pollution Bulletin, 58:1787–1791, 2009.

[106] A. H. Woodcock. Subsurface pelagic sargassum. Journal of Marine Research, 9:77–92, 1950.

[107] A. H. Woodcock. Winds subsurface pelagic sargassum and langmuir circulations. J. Exp. Mar. Biol. Ecol., 170:117–125, 1993.

[108] D. L. Johnson and P. L. Richardson. On the wind-induced sinking of sargassum. J. Exp. Mar. Biol. Ecol., 28:255–267, 1977.

[109] A. Shoener and G. T. Rowe. Pelagic sargassum and its presence among the deep-sea benthos. Deep-Sea Research, 17:923–925, 1970.

[110] S. M. Gallager, C. S. Davis, A. W. Epstein, A. Solow, and R. C. Beardsely. High-resolution observations of plankton spatial distributions correlated with hydrography in the great south channel, georges bank. Deep-Sea Research Part II – Topical Studies in Oceanography, 43(7-8):1627–1663, 1996.

[111] B. Pinelalloul. Spatial heterogeneity as a multiscale characteristic of zooplankton community. Hydrobiologia, 301:17–42, 1995.

[112] A. Solow and J. H. Steele. Scales of plankton patchiness – biomass versus demography. Journal of Plankton Research, 17:1669–1677, 1995.

[113] A. J. Yool. The dynamics of open-ocean plankton ecosystem models. PhD thesis, University of Warwick, 1998.

[114] M. Ledbetter. Langmuir circulations and plankton patchiness. Ecological Modelling, 7:289–310, 1979.

[115] T. Buranathanitt, D. J. Cockrell, and P. H. John. Some effects of langmuir circulation on the quality of water resource systems. Ecological Modelling, 15:49–74, 1982.

[116] J. C. McWilliams and P. P. Sullivan. Vertical mixing by langmuir circulations. Spill Science and Technology Bulletin, 6(3/4):225–237, 2000.

[117] W. H. Sutcliffe Jr., E. R. Baylor, and D. W. Menzel. Sea surface chemistry and langmuir circulation. Deep-Sea Research, 10:233–243, 1963.

[118] P. M. Williams. Sea surface chemistry: Organic carbon and organic nitrogen and phosphorus in surface films and subsurface waters. Deep-Sea Research, 14:791–800, 1967.

[119] T. R. Parsons and M. Takahishi, editors. Biological oceanographic processes. Pergamon, 1973.

[120] S. J. Eisenreich, A. W. Ellerman, and D. E. Armstrong. Enrichment of micronutrients, heavy metals and chlorinated hydrocarbons in wind- generated lake foam. Env. Sci. Tech., 12:413–417, 1978.

[121] H. M. Dierssen, R. C. Zimmerman, and D. J. Burdige. Optics and remote sensing of bahamian carbonate sediment whitings and potential relationship to wind-driven langmuir circulation. Biogeosciences, 6:487–500, 2009.

[122] D. Guo, H. Thee, G. da Silva, J. Chen, W. Fei, S. Kentish, and G. W. Stevens. Borate-catalyzed carbon dioxide hydration via the carbonic anhydrase mechanism. Environmental Science and Technology, 45:4802–4807, 2011.

[123] D. A. Wolf-Gladrow, J. Bijma, and R. E. Zeebe. Model simulation of the carbonate chemistry in the microenvironment of symbiont bearing foraminifera. Marine Chemistry, 64:181–198, 1999.

[124] R. E. Zeebe. Modeling co2 chemistry, d13c, and oxidation of organic carbon and methane in sediment porewater: Implications for paleo-proxies in benthic foraminifera. Geochimica et Cosmochimica Acta, 71:3238–3256, 2007.

[125] K. G. Schulz, U. Riebesell, B. Rost, S. Thoms, and R. E. Zeebe. Determination of the rate constants for the carbon dioxide to bicarbonate inter-conversion in ph-buffered seawater systems. Marine Chemistry, 100:53–65, 2006.

[126] B. Jahne and E. C. Monahan, editors. Third International Symposium on Air-Water Gas Transfer, 1995.

[127] K. S. Johnson. Carbon dioxide hydration and dehydration kinetics in seawater. Limnol. Oceanogr., 27(5):849–855, 1982.

[128] J. A. Quinn and N. C. Otto. Carbon dioxide exchange at the air-sea interface: Flux augmentation by chemical reaction. Journal of Geophysical Research, 76(6):1539–1550, 1971.

[129] K. G. Schulz, J. Barcelos e Ramos, R. E. Zeebe, and U. Riebesell. Co2 perturbation experiments: similarities and differences between dissolved inorganic carbon and total alkalinity manipulations. Biogeosciences, 6:2145–2153, 2009.

[130] J. Uchikawa and R. E. Zeebe. The effect of carbonic anhydrase on the kinetics and equilibrium of the oxygen isotope exchange in the co2–h2o system: Implications for del18o vital effects in biogenic carbonates. Geochimica et Cosmochimica Acta, 95:15–34, 2012.

[131] G. R. Williams. The rate of hydration of carbon dioxide in natural waters. Environmental Biogeochemistry, 35:281–289, 1983.

[132] W. E. Asher and J. F. Pankow. The interaction of mechanically generated turbulence and interfacial films with a liquid phase controlled gaslliquid transport process. Tellus, 38B:305–318, 1986.

[133] W. E. Asher and R. Wanninkhof. Transient tracers and air-sea gas transfer. Journal of Geophysical Research, 103(C8):15939–15958, 1998.

[134] B. Bolin. On the exchange of carbon dioxide between the atmosphere and the sea. Tellus XII, 3:275–281, 1960.

[135] J. Boutin, J. Etcheto, and P. Ciais. Possible consequences of the chemical enhancement effect for air- sea co2 flux estimates. Phys. Chem. Earth (B), 24(5):411–416, 1999.

[136] J. Goldman and M. R. Dennett. Carbon dioxide exchange between air and seawater: No evidence for rate catalysis. Science, 220:199–201, 1982.

[137] T. E. Hoover and D. C. Berkshire. Effects of hydration on carbon dioxide exchange across an air-water interface. Journal of Geophysical Research, 75(2):456–464, 1969.

[138] C. Jacobs, J. F. Kjeld, P. D. Nightingale, R. C. Upstill-Goddard, S. Larson, and W. Oost. Possible errors in co2 air-sea transfer velocity from deliberate tracer releases and eddy covariance measurements due to near-surface concentration gradients. Journal of Geophysical Research, 107(C9):1–26, 2002.

[139] J. Kuss and B. Schneider. Chemical enhancement of the co2 gas exchange at a smooth seawater surface. Marine Chemistry, 91:165–174, 2004.

[140] J. F. Pankow and W. E. Asher. Carbon dioxide transfer at the gas/water interface as a function of system turbulence. Gas Transfer at Water Surfaces, pages 101–111, 1982.

[141] L. P. VanRoekel, B. Fox-Kemper, P. P. Sullivan, P. E. Hamlington, and S. R. Haney. The form and orientation of langmuir cells for misaligned wind and waves. Journal of Geophysical Research, 117:1–22, 2012.

[142] Gilbert Strang. On the construction and comparison of difference schemes. SIAM J. Numer. Anal., 5(3):506–517, September 1968.

[143] B. P. Sommeijer, L. F. Shampine, and J. G. Verwer. Rkc: An explicit solver for parabolic pdes. Journal of Computational Applied Mathmatics, 88:315–326, 1997.

[144] J. G. Verwer, B. P. Sommeijer, and W. Hundsdorfer. Rkc time-stepping for advection-diffusion-reaction problems. Journal of Computational Physics, 201:61–79, 2004.

[145] K. E. Niemeyer and C. J. Sung. Accelerating moderately stiff chemical kinetics in reactive-flow simulations using gpus. Journal of Computational Physics, 256:854–871, 2014.

[146] S. H. Lam and D. A. Goussis. Understanding complex chemical kinetics with computational singular perturbation. In Twenty-Second Symposium (International) on Combustion, The University of Washington, Seattle, Washington, pages 931–941. The Combustion Institute, Pittsburgh, August 14-19 1988.

[147] S. H. Lam. Using csp to understand complex chemical kinetics. Combust. Sci. Tech., 89:375–404, 1993.

[148] S. H. Lam and D. A. Goussis. The csp method for simplifying kinetics. Int. J. Chem. Kin., 26:461–486, 1994.

[149] I. D. Lima, D. B. Olson, and S. C. Doney. Biological response to frontal dynamics and mesoscale variability in oligotrophic environments: Biological production and community structure. Journal of Geophysical Research, 107(C8):3111, 2002.

[150] B. Schneider, L. Bopp, M. Gehlen, J. Segschneider, T. L. Frolicher, F. Joos, P. Cadule, P. Friedlingstein, S. C. Doney, and M. J. Behrenfeld. Spatio-temporal variability of marine primary and export production in three global coupled climate carbon cycle models. Biogeosciences Discussions, European Geosciences Union, 4:1877–1921, 2007.

[151] C. Hauri, N. Gruber, M. Vogt, S. C. Doney, R. A. Feely, Z. Lachkar, A. Leinweber, A. M. P. McDonnell, M. Munnich, and G. K. Plattner. Spatiotemporal variability and long-term trends of ocean acidification in the california current system. Biogeosciences, 10:193–216, 2013.

[152] M. J. Behrenfeld. Climate-mediated dance of the plankton. Nature Climate Change, 4:880–887, 2014.

[153] A. D. Barton, M. S. Lozier, and R. G. Williams. Physical controls of variability in north atlantic phytoplankton communities. Limnology and Oceanography, 60:181–197, 2015.

[154] P. W. Boyd, C. E. Cornwall, A. Davison, S. C. Doney, M. Fourquez, C. L. Hurd, I. D. Lima, and A. McMinn. Biological responses to environmental heterogeneity under future ocean conditions. Global Change Biology, 22:2633–2650, 2016.

[155] S. C¿ Doney. Major challenges confronting marine biogeochemical modeling. Global Biogeochem Cycles, 13(3):705–714, 1999.

[156] T. R. Anderson. Plankton functional type modelling: running before we can walk? Journal of Plankton Research, 27(11):1073–1081, 2005.

[157] J. R. Dearman, A. H. Taylor, and K. Davidson. Influence of autotroph model complexity on simulations of microbial communities in marine mesocosms. Mar. Ecol. Prog., 250:13–28, 2003.

[158] J. C. Blackford, J. I. Allen, and F. J. Gilbert. Ecosystem dynamics at six contrasting sites: A generic modelling study. Journal of Marine Systems, 52:191–215, 2004.

[159] M. A. M. Friedrichs, J. A. Dusenberry, L. A. Anderson, R. A. Armstrong, F. Chai, J. R. Christian, S. C. Doney, J. Dunne, M. Fujii, R. Hood, D. Jr, J. K. Moore, M. Schartau, Y. H. Spitz, and J. D. Wiggert. Assessment of skill and portability in regional marine biogeochemical models: Role of multiple planktonic groups. Journal of Geophysical Research, 112:1–22, 2007.

[160] J. W. Ammerman, R. R. Hood, D. A. Case, and J. B. Cotner. Phosphorus deficiency in the atlantic: An emerging paradigm in oceanography. EOS, 84(18):165–170, 2003.

[161] M. Levy, M. Gavart, L. Memery, G. Caniaux, and A. Paci. A four-dimensional mesoscale map of the springbloom in the northeast atlantic (pommeexperiment): Results of a prognostic model. Journal of Geophysical Research, 110(C07S21), 2005.

[162] S. D. Ayata, M. Levy, O. Aumont, A. Siandra, J. Sainte-Marie, A. Tagliabue, and O. Bernard. Phytoplankton growth formulation in marine ecosystem models: Should we take into account photo-acclimation and variable stoichiometry in oligotrophic areas? Journal of Marine Systems, 125:29–40, 2013.

[163] Y. H. Spitz, J. R. Moisan, and M. R. Abbott. Con"guring an ecosystem model using data from the bermuda atlantic time series (bats). Deep-Sea Research II, 48:1733–1768, 2001.

[164] S. Doney, D. M. Glover, and R. G. Najjar. A new coupled, one-dimensional biological-physical model for the upper ocean: Applications to the jgofs bermuda atlantic time-series study (bats) site. Deep-Sea Research II, 43(2-3):591–624, 1996.

[165] M. J. R. Fasham, H. W. Ducklow, and S. M. McKelie. A nitrogen-based model of plankton dynamics in the oceanic mixed layer. Journal of Marine Research, 48(591-639), 1990.

[166] K. Fennel, M. Losch, J. Schroter, and M. Wenzel. Testing a marine ecosystem model: sensitivity analysis and parameter optimization. Journal of Marine Systems, 28:45–63, 2001.

[167] G. C. Hurtt and R. A. Armstrong. A pelagic ecosystem model calibrated with bats data. Deep-Sea Research II, 43(2-3):653–683, 1996.

[168] G. C. Hurtt and R. A. Armstrong. A pelagic ecosystem model calibrated with bats and owsi data. Deep-Sea Research I, 46:27–61, 1999.

[169] L. M. Lawson, E. E. Hofmann, and Y. H. Spitz. Time series sampling and data assimilation in a simple marine ecosystem model. Deep-Sea Research II, 43(2-3):625–651, 1996.

[170] M. Vichi and N. Pinardi abd S. Masina. An advanced model of pelagic biogeochemistry for the global ocean ecosystem. part i: theory. Journal of Marine Systems Special Issue: Advances in Marine Ecosystem Modelling Research Symposium, 2005.

[171] Alan D. Jassby and Trevor Platt. Mathematical formulation of the relationship between photosynthesis and light for phytoplankton. Limnology and Oceanography, 21(4):540–547, 1976.

[172] J. G. Baretta-Bekker, J. W. Baretta, and W. Ebenhoh. Microbial dynamics in the marine ecosystem model ersem ii with decoupled carbon assimilation and nutrient uptake. Journal of Sea Research, 38(3-4):195–211, 1997.

[173] R. J. Geider, H. L. MacIntyre, and T. M. Kana. A dynamic model of phytoplankton growth and acclimation: responses of the balanced growth rate and chlorophyll a:carbon ratio to light, nutrient limitation and temperature. Mar. Ecol. Prog. Ser., 148:187–200, 1997.

[174] A. F. Blumberg and G. L. Mellor. A description of a three-dimensional coastal ocean circulation model. Three Dimensional Coastal Ocean Models, 1987.

[175] G. L. Mellor and T. Yamada. Development of a turbulence closure model for geophysical fluid problems. Review of Geophysical Space Physics, 20(4):851–875, 1982.

[176] D. K. Steinberg, C. A. Carlson, N. R. Bates, R. J. Johnson, A. F. Michaels, and A. H. Knap. Overview of the us jgofs bermuda atlantic time-series study (bats): a decade-scale look at ocean biology and biogeochemistry. Deep-Sea Research II, 48:1405–1447, 2001.

[177] K. A. Fanning. Nutrient provencies in the sea: Concentration ratios, reaction rate ratios, and ideal covariation. Journal of Geophysical Research, 97(C4):5693–5712, 1992.

[178] A. F. Michaels, A. H. Knap, R. L. Dow, K. Gundersen, R. J. Johnson, J. Sorensen, A. Close, G. A. Knauer, S. E. Lohrenz, V. A. Asper, M. Tuel, and R. Bidigare. Seasonal pattern of ocean biogeochemistry at the u. s. jgofs bermuda atlantic time-series study site. Deep-Sea Research I, 41(7):1013–1038, 1993.

[179] K. K. Cavender-Bares, D. M. Karl, and S. W. Chisholm. Nutrient gradients in the western north atlantic ocean: Relationship to microbial community structure and comparison to patterns in the pacific ocean. Deep-Sea Research I, 48:2373–2395, 2001.

[180] A. C. Martiny, C. T. A. Pham, F. W. Primeau, J. A. Vrugt, J. K. Moore, S. A. Levin, and M. W. Lomas. Strong latitudinal patterns in the elemental ratios of marine plankton and organic matter. Nature Geoscience, 2013.

[181] A. Singh, S. E. Baer, U. Riebesell, A. C. Martiny, and M. W. Lomas. C:n:p stoichiometry at the bermuda atlantic time-series study station in the north atlantic ocean. Biogeosciences, 12:6389–6403, 2015.

[182] P. D. Killworth. Time interpolation of forcing fields in ocean models. Journal of Physical Oceanography, 26:136–143, 1995.

[183] B. L. Hua, J. C. McWilliams, and W. B. Owens. An objective analysis of the polymode local dynamics experiment. part ii: Streamfunction and potential vorticity fields during the intensive period. Journal of Physical Oceanography, 16:506–522, 1985.

[184] B. M. Adams, L. E. Bauman anad W. J. Bohnhoff, K. R. Dalbey, M. S. Ebeida, J. P. Eddy, M. S. Eldred, P. D. Hough, K. T. Hu, J. D. Jakeman, J. A. Stephens, L. P. Swiler, D. M. Vigil, and T. M. Wildey. Dakota, a multilevel parallel object-oriented framework for design optimization, parameter estimation, uncertainty quantification, and sensitivity analysis: Version 6.0 user's manual. Technical report, Sandia Technical Report SAND2014-4633, 2015.

[185] G. N. Vanderplaats. Conmin – a fortran program for constrained function minimization. Technical report, Technical Report TM X-62282, NASA, 1973.

[186] G. Badin, A. Tandon, and A. Mahadevan. Lateral mixing in the pycnocline by baroclinic mixed layer eddies. Journal of Physical Oceanography, 41:2080–2100, 2011.

[187] J. R. Taylor. Turbulent mixing, restratification, and phytoplankton growth at a submesoscale eddy. Geophysical Research Letters, 43:5784–5792, 2016.

[188] G. A. Gray and T. G. Kolda. Algorithm 856: Appspack 4.0: Asynchronous parallel pattern search for derivative-free optimization. ACM Transactions on Mathematical Software, 32(3):485–507, 2006.

[189] S. Alvain, C. Moulin, Y. Dandonneau, and F. M. Breon. Remote sensing of phytoplankton groups in case 1 waters from global seawifs imagery. Deep-Sea Research I, 52:1989–2004, 2005.

[190] D. Archer. Upper ocean physics as relevant to ecosystem dynamics: a tutorial. Ecological Applications, 5:724–739, 1995.

[191] John P. Crimaldi, Jillian R. Hartford, and Jeffrey B. Weiss. Reaction enhancement of point sources due to vortex stirring. Physical Review E, 74(016307), 2006.

[192] B. Fox-Kemper, R. Ferrari, and R. Hallberg. Parameterization of mixed layer eddies. part i: Theory and diagnosis. Journal of Physical Oceanography, 38(6):1145–1165, 2008.

[193] P. R. Gent and J. C. McWilliams. Isopycnal mixing in ocean circulation models. Journal of Physical Oceanography, 20:150–155, 1990.

[194] B. Jahne, G. Heinz, and W. Dietrich. Measurements of the diffusion coefficients of sparingly soluble gases in water with a modified barrer method. Journal of Geophysical Research, 91:10,767–10,776, 1987.

[195] W. G. Large, J. C. McWilliams, and S. C. Doney. Oceanic vertical mixing: a review and a model with nonlocal boundary layer parameterization. Review of Geophysics, 32:363–403, 1994.

[196] Wentian Li. Mutual information functions versus correlation functions. Journal of Statistical Physics, 60(5-6):823–837, 1990.

[197] Qing Li, Adrean Webb, Baylor Fox-Kemper, Anthony Craig, Gokhan Danabasoglu, William G. Larger, and Mariana Vertenstein. Langmuir mixing effects on global climate: Wavewatch iii in cesm. Ocean Modelling, 103:145–160, 2016.

[198] P. S. Liss and L. Merlivat. Air-sea gas exchange rates: Introduction and synthesis. In P. Buat-Menard, editor, The Role of Air-Sea Gas Exchange in Geochmical Cycling, pages 113–127. NATO ASI Series, 1986.

[199] G. Lohmann and J. Schneider. Dynamics and predictability of stommel's box model. a phase-space perspective with implications for decadal climate variability. Tellus, 51A:326–336, 1999.

[200] J. Marshall. On the parameterization of geostrophic eddies in the ocean. Journal of Physical Oceanography, 11:257–271, 1981.

[201] A. P. Martin. Phytoplankton patchiness: the role of lateral stiring and mixing. Progress in Oceanography, 57(2):125–174, May 2003.

[202] P. D. Nightingale, G. Malin, C. S. Law, A. J. Watson, P. S. Liss, M. I. Liddicoat, J. Boutin, and R. C. Upstill-Goddard. In situ evaluation of air-sea gas exchange parameterizations using novel conservative and volatile traces. Global Biogeochem, Cycles, 14:373–387, 2000.

[203] Kenneth R. Pratt, James D. Meiss, and John P. Crimaldi. Reaction enhancement of initially distant scalars by lagrangian coherent structures. Physics of Fluids, 27(035106), 2015.

[204] H. Stommel. Thermohaline convection with two stable regimes of flow. Tellus, 13:224–230, 1961.

[205] Peter P. Sullivan, James C. McWilliams, and Chin-Hoh Moeng. A subgrid-scale modeal for large-eddy simulations of planetary boundary-layer flow. Boundary-Layer Meteorology, 71:247–276, 1994.

[206] S. A. Thorpe. Langmuir circulation. Annual Review of Fluid Mechanics, 36:55–79, 2004.

[207] M. Vichi, P. Oddo, M. Zavatarelli, A. Coluccelli, G. Coppini, M. Celio, S. Fonda Umani, and N. Pinardi. Calibration and validation of a one-dimensional complex marine biogeochemical flux model in different areas of the northern adriatic shelf. Annales Geophysicae, European Geosciences Union (EDU), 21(1):413–436, 2003.

[208] R. Wanninkhof and E. McGills. A cubic relationship between air-sea co2 exchange and wind speed. Geophysical Research Letters, 26:1889–1892, 1999.

[209] R. F. Weiss. The solubility of nitrogen, oxygen and argon in water and seawater. Deep-Sea Research, 17:721–735, 1970.

[210] P. Welander. A simple heat-salt oscillator. Dynamics of Atmospheres and Oceans, 6:233–242, 1982.

[211] G. Boccaletti, R. Ferrari, and B. Fox-Kemper. Mixed layer instabilities and restratification. Journal of Physical Oceanography, 37:2228–2250, 2007.

[212] B. Fox-Kemper, R. Ferrari, and R. W. Hallberg. Parameterizations of mixed layer eddies. part i: Theory and diagnosis. Journal of Physical Oceanography, 38:1145–1165, 2008.

[213] N. Gruber, M. Gloor, S. M. Mikaloff Fletcher, S. C. Doney, S. Dutkiewicz, M. J. Follows, M. Gerber, A. R. Jacobson, F. Joos, K. Lindsey, D. Menemenlis, A. Mouchet, S. A. Muller, J. L. Sarmiento, and T. Takahashi. Oceanic sources, sinks, and transport of atmospheric co2. Global Biogeochem Cycles, 23:1–21, 2009.

[214] T. W. N. Haine and J. Marshall. Gravitational, symmetric, and baroclinic instability of the ocean mixed layer. Journal of Physical Oceanography, 28:634–658, 1997.

[215] S. Haney, B. Fox-Kemper, and K. Julien. Symmetric and geostrophic instabilities in the wave-forced ocean mixed layer. Journal of Physical Oceanography, page Submitted, 2015.

[216] A. Mahadevan, E. D'Asaro, and M. J. Perry. Eddy-driven stratification initiates north atlantic spring phytoplankton blooms. Science, 337:54–58, 2012.

[217] R. C. Miller. The sea. Nelson.

[218] C. N. Murray and J. P. Riley. The solubility o gases in distilled water and seawater - iv. carbon dioxide. Deep-Sea Research, 18:588–541, 1971.

[219] J. L. Sarmiento. Ocean Biogeochemical Dynamics. Princeton Univeristy Press, 2013.

[220] Richard E. Zeebe, D. A. Wolf-Gladrow, and H. Jensen. On the time required to establish chemical and isotopic equilibrium in the carbon dioxide system in seawater. Marine Chemistry, 65:135–153, 1999.